1974

Experimental studies of muonium production and the muonium-antimuonium transition in free space

Cheng-shong Hsieh

College of William & Mary - Arts & Sciences

INFORMATION TO USERS

This material was produced from a microfilm copy of the original document. While the most advanced technological means to photograph and reproduce this document have been used, the quality is heavily dependent upon the quality of the original submitted.

The following explanation of techniques is provided to help you understand markings or patterns which may appear on this reproduction.

1. The sign or "target" for pages apparently lacking from the document photographed is "Missing Page(s)". If it was possible to obtain the missing page(s) or section, they are spliced into the film along with adjacent pages. This may have necessitated cutting thru an image and duplicating adjacent pages to insure you complete continuity.

2. When an image on the film is obliterated with a large round black mark, it is an indication that the photographer suspected that the copy may have moved during exposure and thus cause a blurred image. You will find a good image of the page in the adjacent frame.

3. When a map, drawing or chart, etc., was part of the material being photographed the photographer followed a definite method in "sectioning" the material. It is customary to begin photoing at the upper left hand corner of a large sheet and to continue photoing from left to right in equal sections with a small overlap. If necessary, sectioning is continued again — beginning below the first row and continuing on until complete.

4. The majority of users indicate that the textual content is of greatest value, however, a somewhat higher quality reproduction could be made from "photographs" if essential to the understanding of the dissertation. Silver prints of "photographs" may be ordered at additional charge by writing the Order Department, giving the catalog number, title, author and specific pages you wish reproduced.

5. PLEASE NOTE: Some pages may have indistinct print. Filmed as received.

EXPERIMENTAL STUDIES OF MUONIUM PRODUCTION AND THE

MUONIUM-ANTIMUONIUM TRANSITION IN FREE SPACE

———————

A Thesis

Presented to

The Faculty of the Department of Physics

The College of William and Mary in Virginia

———————

In Partial Fulfillment

Of the Requirements of the Degree of

Doctor of Philosophy

———————

by

Cheng-shong Hsieh

May 1974
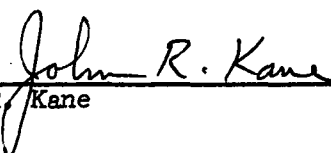
APPROVAL SHEET

This dissertation is submitted in partial fulfillment of

the requirements of the degree of

Doctor of Philosophy

Cheng-Chong Hsieh
Author
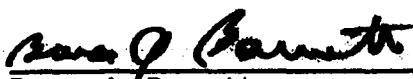
Approved, May 1974

John R. Kane
John R. Kane

Carl E. Carlson
Carl E. Carlson

Morton Eckhause
Morton Eckhause

W. J. Kossler
William J. Kossler

Bruce A. Barnett
Bruce A. Barnett
Department of Physics and Astronomy
University of Maryland

EXPERIMENTAL STUDIES OF MUONIUM PRODUCTION AND THE

MUONIUM-ANTIMUONIUM TRANSITION IN FREE SPACE

TABLE OF CONTENTS

ABSTRACT

Experimental studies of muonium production and a search for the muonium ($\mu^+ e^-$) to antimuonium ($\mu^- e^+$) transition in a vacuum space are reported.

The emission of muonium from the surface of thin gold foils has been studied by a spin precession technique using the low momentum muon beam from the SREL synchrocyclotron. The data analysis of the decay asymmetry of the muons, which stopped in the gold foils, yields a lower limit for the rate of muonium formation of 0.35 ± 0.06.

A search for the $(\mu^+ e^-) \to (\mu^- e^+)$ process in a vacuum has been carried out using $(\mu^+ e^-)$ atoms formed in a thin gold foil. Observation of the possible $(\mu^+ e^-) \to (\mu^- e^+)$ transition in free space is important as a test of lepton number conservation laws and as a search for a heretofore undetected weak process. The experimental technique involved the detection of a high energy e^- from μ^- decay which occurred within a 4 μsec gate opened by the stopped μ^+ signal. The observed transition rate was consistent with zero, and the results set an upper limit on the coupling constant ratio $C_{M\bar{M}}/C_V \lesssim 100$, assuming the M-$\bar{M}$ process is a 4-fermion weak interaction of the universal V-A form.

v

I. INTRODUCTION

At present, the lepton classification scheme consists of four different particles: e^-, μ^-, ν_e, ν_μ and their antiparticles e^+, μ^+, $\bar{\nu}_e$, $\bar{\nu}_\mu$. The behavior of these particles has been studied extensively, both in experiment and theory, over the last 15 years. Nevertheless, the reason for the difference between the muon and the electron is still not understood. The existing evidence seems to indicate that both the muon and the electron participate only in the electromagnetic and weak interactions, both having the same interaction properties[1] except for the difference in mass ($m_\mu = 207\ m_e$) and the fact that they are associated with different neutrinos[2].

The distinctions between electron neutrinos (ν_e) and muon neutrinos (ν_μ) and the apparent absence of muon-electron transitions without neutrinos, such as

Reactions	Upper limit of branching ratio[3,4]	
$\mu \rightarrow e\gamma$	2.2×10^{-8}	(1)
$\mu \rightarrow 3e$	6×10^{-9}	(2)
$\mu \rightarrow e\gamma\gamma$	1.6×10^{-5}	(3)
$\mu + Z \rightarrow Z + e$	1.6×10^{-8}	(4)

lead one to speculate that there is an intrinsic quantum number which results from the differences between muons and electrons, and their neutrinos, and is conserved in all interactions.[5,6] The assignment of these so called leptonic numbers is not unique. Several potentially valid schemes have been

suggested.[5,7] (see Appendix A.) All of them are consistent with the observed weak processes and also with the absence of those processes which have been shown experimentally to be inhibited.

No matter how one assigns the lepton quantum number, the nature of the conservation law is an open question. Usually, two possibilities for the conservation of lepton number in the weak interaction are considered.[6,8] The more usual one is an additive law. If we choose $L_e = +1$ for e^- and ν_e, and $L_e = -1$ for their antiparticles, $L_\mu = +1$ for μ^- and ν_μ, and $L_\mu = -1$ for their antiparticles as in Table 1 (a),this additive form states that the algebraic sum of L_e and of L_μ are separately conserved in all interactions.

The other possible conservation law is a parity-like multiplicative conservation law, in which only the sum $\Sigma(L_e + L_\mu)$ and the sign $(-1)^{\Sigma L_\mu}$ are conserved in all interactions. The sign $(-1)^{\Sigma L_e}$ must consequently also be conserved. This law has been proposed because of the fact that all the "missing interactions" involve an odd number of muon-like and electron-like particles.

Of the two laws, the additive one is the more restrictive. In particular, it forbids the following four-lepton interactions allowed by the multiplicative law:[8]

$$M(\mu^+ e^-) \rightarrow \overline{M}(\mu^- e^+) \qquad (Muonium \rightarrow Antimuonium), \quad (5)$$

and

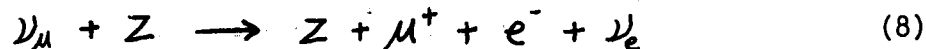$$\mu^+ \rightarrow e^+ + \overline{\nu}_e + \nu_\mu \qquad (Exotic\ Muon\ Decay). \quad (6)$$

There are certain theoretical arguments in favor of a multiplicative law

for muons and electrons, since it may be derived from reflection or per-
mutation symmetry principles in which e and μ are regarded as a combin-
ation of two more primitive leptons.[8,9]

Several experiments have been carried out in search of the
reactions that would determine which form of the lepton conservation
law prevails. The present results are insufficient to rule out the
possibility of a multiplicative conservation law for the muon number,
and only provide upper limits for the associated weak interaction coupl-
ing constant C_M that are much larger than the universal vector-coupling
constant of beta decay C_V. Amato[10] et al. have looked for muonium-
antimuonium conversion in a high pressure argon gas target and were able
to set an upper limit of only $C_M \leqslant 5800\ C_V$. A group at Stanford[11] has
searched for the equivalent reaction

$$e^- + e^- \longrightarrow \mu^- + \mu^-$$ (7)

using colliding beams. They were able to set an upper limit of $C_M \leqslant 610$
C_V. Another test has been made by Chang.[12] He has examined a CERN high
energy neutrino experiment[13] for evidence of "inverse exotic muon decay",

$$\nu_\mu + Z \longrightarrow Z + \mu^+ + e^- + \nu_e$$ (8)

where ν_μ are produced from the decay of π^+ or K^+. He estimated the upper
limit of the coupling constant for the exotic muon decay given by reaction
(6) to be $C_M \leqslant 4.1\ C_V$.

Another indirect search for exotic muon decay has been made in a
high energy $\nu_e(\bar{\nu}_e)$ - nucleon scattering experiment at CERN by the Gargamelle
group.[14] The presence of $\bar{\nu}_e$ (possibly due in part to exotic μ decays) is
detected in the ν beam, in the energy range from 1 GeV to 6 GeV by distinguish-
ing between the inverse beta decay reactions

$$\bar{\nu}_e + N \rightarrow e^+ + \text{hadrons} , \tag{9}$$

and

$$\nu_e + N \rightarrow e^- + \text{hadrons} . \tag{10}$$

The experimental result obtained was expressed in terms of the branching ratio

$$r = \frac{(\mu^+ \rightarrow e^+ + \bar{\nu}_e + \nu_\mu)}{\text{all } \mu^+ \text{ decay modes}}$$

where the μ^+ decay modes are (1) normal decay mode $\mu^+ \rightarrow e^+ + \nu_e + \bar{\nu}_\mu$ and (2) exotic decay mode $\mu^+ \rightarrow e^+ + \bar{\nu}_e + \nu_\mu$. The group found the branching ratio r to be $\leqslant 0.25$. The value r = 0.5 is predicted by the multiplicative law. The result, however, is insufficient to invalidate conclusively the multiplicative scheme of lepton number conservation. If we assume the same strength for exotic muon decay and normal muon decay, the upper limit of coupling constant C_M would turn out to be equal to 0.6 C_V according to this value of the branching ratio.

A more direct search for the reaction (6) has been proposed[15] at LAMPF using the inverse beta decay process

$$\bar{\nu}_e + P \rightarrow N + e^+ \tag{11}$$

on free protons in water to detect the electron-antineutrino $\bar{\nu}_e$ from the exotic decay. The neutrinos originating in the LAMPF beam stop have a typical energy of 40 MeV. This energy is below the threshold for producing muons and pions from muon-neutrinos. Electron-neutrino interactions can therefore be studied without interference from the muon-neutrino processes which dominate neutrino events at higher energies. It is hoped that this experiment will be sensitive enough to detect any events, or to set an upper limit of interaction which restricts C_M to the level ~ 0.25 C_V.

There is, therefore, no present experimental evidence which would allow us to distinguish unambiguously between the two lepton number conservation laws for weak interactions. An additional consideration is that reactions (5) and (6) represent two different currents. A negative result in the exotic muon decay experiment does not necessarily imply the non-existence of a muonium-antimuonium transition process, because (5) requires the presence of a weak neutral current component. This would be a neutral current which couples muonic leptons to electronic leptons, which is distinct from the L_μ and L_e conserving neutral current which is the object of much recent activity. Actually, reactions (5) and (6) are complementary to each other since in the M-$\bar{\text{M}}$ transition process all lepton participants are charged, thus allowing us to make a comparison between the behavior of charged leptons versus those of neutral leptons. However, our present empirical knowledge about reactions of this kind is still far removed from yielding a conclusive result.

It has been pointed out by Feinberg and Weinberg[8,16] that a strong environmental quenching seriously affects the M-$\bar{\text{M}}$ transition rate. This is due to the presence of static external electromagnetic fields which will break the original energy degeneracy between the states of M and $\bar{\text{M}}$. In addition, an inelastic collision in which a μ^- (a constituent of $\bar{\text{M}}$) is captured by an environmental medium introduces another mode of breakup of the M-$\bar{\text{M}}$ system. A simple V-A four-fermion weak interaction calculation at Fermi coupling strength (β-decay coupling constant) predicts an overall probability for $\bar{\text{M}}$ disappearance in vacuum P($\bar{\text{M}}$) which is only 2.5×10^{-5} (in the absence of external fields). In a gaseous

medium (such as argon) the rate would be reduced to $P(\bar{M}) = 2.5 \times 10^{-5}(1/N)$, where N is the average number of collisions suffered by the M-$\bar{M}$ system over the course of a muon lifetime. Thus for STP conditions we are faced with a suppression factor of $\sim 10^{6}$. In a solid, such as quartz or ice, the situation is even less promising. The probability $P(\bar{M})$ would be reduced to a value between 10^{-14} and 10^{-20} depending on the material. Therefore, in order to maintain an experimentally accessible conversion probability, it is best to perform the experiment in a vacuum free space. A great deal of our effort has gone into attempts to search for a suitable material as a free muonium production target and to avoid these environmental influences in the M-$\bar{M}$ transition rate.

Section II of this paper contains a description of the theories which bear upon the question of free muonium formation in thin gold foils. It also contains the calculation of the $\bar{M}$ disappearance rate in vacuum, and how the external electromagnetic fields affects this rate.

Section III contains a description of the experimental setup for the production of muonium and the detailed data analysis of the same.

Section IV includes a description of the experimental search for the muonium-antimuonium transition, as well as the corresponding data reduction.

In section V the experimental results are reported. Possible improvements in this experiment for the future are considered with regard to the availability of a higher intensity muon beam at LAMPF.

II. THEORY

A. Muonium Formation

When a positive muon beam is slowed down to sufficiently low
energy in matter there develops an energetically favorable condition[17]
in which, through charge-exchange, a μ^+ captures an electron from an
atom of the medium to form a ground state muonium atom (μ^+e^-). This
atom may be ionized and form again many times as the system loses energy.
In a small group of materials, the majority of μ^+ particles reach thermal
velocity in the muonium state. By selecting highly polarized μ^+, the
muonium state can be studied by the precession technique. A thermal
muonium atom which chemically resembles a low mass hydrogen atom can
interact with nearby matter through collisions or chemical reactions.
Thus, although polarized muonium may initially form, a process of spin
relaxation can quickly result whenever (1) chemically active or para-
magnetic impurities are present, (2) covalent bonding of the muonium
(μ^+e^-) atom to adjacent sites occurs, or (3) electron traps are present
in the lattice.

Several workers have investigated muonium formation and sub-
sequent depolarization inside solid materials[18-21]. These solids
include quartz, ice, germanium, and silicon. Successful attempts have
also beem made to observe muonium in argon gas.[22] For the purposes of
an M-$\bar{\text{M}}$ conversion experiment, a gas or solid environment presents a

substantial disadvantage as pointed out by Feinberg and Weinberg[16] (see section IIB). The above materials, some of which are highly efficient in forming muonium, are inappropriate as media in which to pursue the M-$\bar{\text{M}}$ transition because of strong environmental quenching. It is necessary that the muonium formed in a medium be quickly transferred to a vacuum free space, in which the M-$\bar{\text{M}}$ system can develop free of external influence. We initially selected as our target an array of thin gold foils spaced at regular intervals in a vacuum chamber.

We have reported the first observation of free muonium formation in thin gold foils and subsequent delivery of the muonium atoms to the intervening vacuum space.[23,24] Thin gold foils were chosen as target mainly because gold is known to be chemically inactive and the foils were thin enough to permit the muonium atom to diffuse out in a very short time.

The nature of the physical mechanism which would account for this muonium production is not clear to us at this time. A variety of related processes suggest that noble high Z materials may be appropriate candidates for the formation of the muonium atom

(1) A high percentage of the atomic charge-capture reaction of protons in gold to form neutral hydrogen atoms has been shown in the work of J. A. Phillips[25,26]. Figure 1 shows experimental data on the equilibrium fractions of the proton beam passing through a gold target in the charge states H^+, H^o, and H^- (F_{+1}, F_0, and F_{-1}, respectively) as a function of beam kinetic energy. The ratio, F_{+1}/F_0, of the fraction of the beam in the charge state +1 to that in state 0 is approximately equal at a given

energy to the ratio of cross sections, σ_{01}/σ_{10}, for ionization and charge capture. It is seen that at a kinetic energy of 4 keV a fraction of the beam greater than 0.85 is in the neutral state H^0. We have per- formed a separate experiment[27] by using the Space Radiation Effects Laboratory (SREL) Cockroft-Walton accelerator to produce protons. This allowed us to extend the lower bound of energy to 650 eV. Our results show that the fraction of H^0 production is still greater than 0.9 down to this energy, with no sign of decreasing. The fact that this charge-capture cross section σ_{10} for protons in gold at low energies remains high is in contrast to the case of the charge-capture reaction of pro- tons in argon gas. Unlike the case of gold, the charge-capture cross section of protons in argon starts to fall off rapidly at 2 keV proton energy[17]. Therefore, if we use a μ^+ beam instead of protons passing through a gold target, the free muon and muonium fractions, from our theoretical understanding, will be about the same as the H^+ and H^0 fractions at the same velocities, e.g., the cross sections for a 650 eV proton will correspond to a 70 eV μ^+.

(2) It has been shown that large charge-exchange cross sections on the order of 10^{-16} cm^2 are not restricted to the keV energy range in which the ion velocity approximates that of outer atomic electrons.[28,29] For example, in the case of He^+ interacting at energies below 20 eV with Xe atoms there is evidence that charge-exchange proceeds quite favorably via $He^+ + Xe \rightarrow He + Xe^{+*}$ due to a near degeneracy between the initial state (He^+Xe) and the excited states of ($HeXe^{+*}$). There is a sharp peak in the cross section at 10 eV energy that is almost an order of magnitude

larger than that expected in the so-called adiabatic transition. For a multi-electron system such as gold, we also anticipate similar resonance interactions.

(3) Studies of neutralization of slow incident ions on metal surfaces have shown that both resonance and Auger neutralization occur with high probability for adions at high-Z metal surfaces.[30] The mechanism is one of metal electron tunneling through the potential barrier between the surface and the adion to fill an excited state of the incident ion. The ion is then neutralized and the excited atom may be de-excited. The energy is balanced with the simultaneous release from the metal surface of an Auger electron. If a μ^+ beam is incident on a metal surface with sufficient energy, one can speculate that ground state muonium will be formed through the de-excitation of neutralized muonium in the metal surface with the simultaneous emission of an Auger electron.

(4) It has been reported, both in experimental[31] and theoretical[32,33] work, that positrons have a negative work function in gold. Following the calculation of Hodges and Stott[33], we can separate the positron work function ϕ_p, by analogy with the electron case, into three terms:

$$\phi_p = -D - E_0 - E_{corr}. \tag{12}$$

In this expression, D is the potential barrier against electron escape due to the surface-dipole layer, which acts to expel the positron because of its opposite charge. The terms E_0 and E_{corr} together are the positron chemical potential in the interior of the metal. E_0 is called zero point energy which arises from the positron-ion interaction; E_{corr} is the

positron-electron correlation energy which tends to bind the positron to the metal, whereas the positron-ion interaction and the surface-dipole layer both tend to squeeze the positron out of the metal. D and E_0 are normally positive, while E_{corr} is negative. In gold, the sum of D(4.49 eV) and E_0(4.62 eV) is larger than E_{corr}(-7.48 eV). The positron work function ϕ_p for gold is then equal to -1.63 eV.

It has also been shown by Hodges and Stott[33] that the positronium work function ϕ_{ps} can be written as

$$\phi_{ps} = \phi_p + \phi_e - E_B \qquad (13)$$

where ϕ_e = 5.17 eV is the electron work function in gold and E_B is the positronium binding energy (6.8 eV). The positronium work function appears also to be negative in gold (-3.2 eV), and it requires less work to remove positronium from gold than removing just the positron alone.

An independent positronium lifetime experiment[34], in which positrons were stopped in a metal oxide powder, has provided evidence that the free orthopositronium can energetically diffuse out of the powder. This may constitute evidence to support the possibility of a negative work-function for positronium. If a μ^+ replaced an e^+ in these calculations, the major changes in the calculation of the work function would be to reduce the zero point energy E_0 of the lowest Bloch state by a factor $(\frac{m_\mu}{m_e})^{\frac{1}{2}}$, i.e. $\sqrt{207}$, and to slightly increase E_{corr}. This would make the μ^+ workfunction in gold positive.[35] The muonium (μ^+e^-) workfunction in gold, however, would possibly remain at a negative value because the muonium binding energy is 13.5 eV. This implies that it is easier for muonium to diffuse out of a gold surface than for the μ^+ itself.

(5) From the point of view of solubility, it is known that hydrogen is not soluble in gold to any measurable extent.[36] Solubility as used here is defined to mean the capability of the metal to dissolve hydrogen to form hydrides. The solubility of hydrogen in silver is quite low. The value obtained[37] at 800 Torr hydrogen pressure and 400 °C is (5.5×10^{-6}) H per Ag. The solubility of hydrogen in gold would be lower than this value. Since muonium is a hydrogen-like atom, its solubility in gold must likewise be low. This low solubility implies that once muonium is formed in gold it will not stay within the gold, but instead would diffuse to the surface.

B. Muonium-Antimuonium Transition

The muonium $M(\mu^+ e^-)$ can be regarded as a light isotope of hydrogen from the viewpoints of atomic interaction and chemical reaction. It is the simplest system involving the only known charged leptons, the muon and the electron. Hence its study can yield precise information about the interaction of the muon and the electron.[17] From the electromagnetic point of view, the interation of the muon and the electron can be studied through measurements of the energy levels of muonium, which have been carried out by several workers.[38,39] From the weak interaction point of view, the subject matter of this paper, the coupling of muonium M to antimuonium $\bar{M}(\mu^- e^+)$ can be studied through observations of the decay of the negative muon from antimuonium, or through the observation of the characteristic x-rays emitted by the

negative muon when atomically captured in a collision of $\bar{M}$ with a neighboring atom.

The total Hamiltonian for the muonium-antimuonium system in the ground state is

$$H = H_{em} + H_W ,$$

(14)

The term H_{em} is an electromagnetic interaction which predicts the hyperfine structure (hfs) level splitting and the Zeeman interactions of muonium (antimuonium). H_W is the weak interaction perturbation term which couples M and $\bar{M}$ states and is responsible for the $M \rightarrow \bar{M}$ transition process. The explicit form of H_W can be written in the current-current interaction[5,16] as

$$H_W = \frac{C_{M\bar{M}}}{\sqrt{2}} L_\lambda L^\lambda + h.c. ,$$

(15)

where

$$L_\lambda = \bar{\Psi}_\mu \gamma_\lambda (1 + \gamma_5) \Psi_e .$$

(16)

L_λ is a neutral leptonic 4-current, since it involves lepton field operators that leave the total charge unchanged when acting on an occupation number wave function. $C_{M\bar{M}}$ is the muonium-antimuonium coupling constant. $C_{M\bar{M}}$ would be approximately equal to the usual β-decay coupling constant C_v,[16] if one extends the universal Fermi interaction concept to the M-$\bar{M}$ process. This value is about 1.4×10^{-49} erg-cm^3. The field operators

and γ-matrices have their usual meaning. The Hamiltonian H_w is therefore a four-fermion weak interaction of the universal V-A form.

The complete eigenstates and energy levels of the coupled M-$\bar{\text{M}}$ system in an external magnetic field is derived in detail in Appendix B. Because only the charge-conjugation-invariant part of H_w can contribute to the matrix element of the mixed state,[40] the weak interaction Hamiltonian H_w yields a matrix element for conversion of M$\to\bar{\text{M}}$ equal to

$$\langle \bar{M_i} | H_w | M_i \rangle = \begin{cases} \dfrac{\delta}{2} & i = 1, 3 \\[3mm] \dfrac{\delta}{2} (1 + \chi^2)^{-\frac{1}{2}} & i = 2, 4 \end{cases}$$

(17)

where

$$\delta = \frac{C_{M\bar{M}}}{\sqrt{2}} \left(\frac{16}{\pi a_o^3} \right) = 2.1 \times 10^{-12} \left(\frac{C_{M\bar{M}}}{C_V} \right) eV,$$

(18)

$$\chi = \frac{|\vec{H}|}{1585 \, G}$$

(19)

and i=1,2,3, and 4 represent the hfs state with (F,m_F)=(1,+1), (1,0), (1,-1), and (0,0), respectively. F is the total angular momentum quantum number and m_F is the associated magnetic quantum number for the M-$\bar{\text{M}}$ system. The value of δ is $143(\dfrac{C_V}{C_{M\bar{M}}})$ times smaller than

$\lambda = 3 \times 10^{-10}$ eV, the muon decay width. In the low magnetic field region, where x is small, $\langle \bar{M}_i | H_w | M_i \rangle = \frac{\delta}{2}$ is applicable for both the F=1 and F=0 hfs states.

The actual energy levels for the M-$\bar{M}$ coupled 1S system are

$$E_{1\pm} = \frac{A}{4} \pm \frac{1}{2} \left(\Delta^2 + \delta^2 \right)^{1/2}$$

$$E_{2\pm} = \frac{A}{4} \left[-1 + 2 \left(1 + \chi^2 \right)^{+1/2} \right] \pm \frac{\delta}{2} \left(1 + \chi^2 \right)^{-1/2}$$

$$E_{3\pm} = \frac{A}{4} \pm \frac{1}{2} \left(\Delta^2 + \delta^2 \right)^{1/2}$$

$$E_{4\pm} = \frac{A}{4} \left[-1 - 2 \left(1 + \chi^2 \right)^{+1/2} \right] \pm \frac{\delta}{2} \left(1 + \chi^2 \right)^{-1/2}$$

(20)

where + and - notation refers to states of symmetric and antisymmetric combinations of M and $\bar{M}$, Δ is the energy splitting of the M-$\bar{M}$ system due to the presence of an external electromagnetic field, and A is the zero-field hfs splitting. For the above, $\Delta \tilde{=} 2\mu_B^e |\vec{H}|$ for the states with F=1, $m_F = \pm 1$ (μ_B^e is electron Bohr magneton). The corresponding new energy eigenstates are

$$| M_{1+} \rangle = \left[2W(W-\Delta) \right]^{-1/2} \left(\delta | M_1 \rangle + (W-\Delta) | \bar{M}_1 \rangle \right)$$

$$| M_{1-} \rangle = \left[2W(W+\Delta) \right]^{-1/2} \left(-\delta | M_1 \rangle + (W+\Delta) | \bar{M}_1 \rangle \right)$$

$$| M_{2\pm} \rangle = \frac{1}{\sqrt{2}} \left(| M_2 \rangle \pm | \bar{M}_2 \rangle \right)$$

$$| M_{3+} \rangle = \left[2W(W-\Delta) \right]^{-1/2} \left(\delta | M_3 \rangle + (W-\Delta) | \bar{M}_3 \rangle \right)$$

$$| M_{3-} \rangle = \left[2W(W+\Delta) \right]^{-1/2} \left(-\delta | M_3 \rangle + (W+\Delta) | \bar{M}_3 \rangle \right)$$

$$| M_{4\pm} \rangle = \frac{1}{\sqrt{2}} \left(| M_4 \rangle \pm | \bar{M}_4 \rangle \right),$$

$$(21)$$

where $W = (\Delta^2 + \delta^2)^{1/2}$. We note that if $\Delta = 0$, i.e., in the absence of an external magnetic field, the four states with $m_F = \pm 1$ simply reduce to the expected symmetric and antisymmetric combination of M and $\bar{M}$. Further, when $\Delta = 0$, we have the conditions:

$$E_{i+} - E_{i-} = \delta \qquad\qquad i = 1, 2, 3, 4$$

$$(22)$$

Figure 2 shows the energy level splitting vs. the magnetic field, where, for the purpose of illustration, the effect of δ has been greatly exaggerated. Dashed lines represent unperturbed muonium (or antimuonium) hfs energy levels. Solid lines are the energy levels of the M-$\bar{M}$ coupled system. We see that both of the levels, F=1 and F=0, that are present at zero-field when H_W is absent are each split into a pair of levels by the action of H_W. The separation of energy levels for each pair is equal to δ. For all values of magnetic field, the presence of H_W similarly splits each of the two unperturbed levels $E_2 = \bar{E}_2$ (F=1, $m_F = 0$) and $E_4 = \bar{E}_4$ (F=0, $m_F = 0$)

into a pair of levels, respectively (E_{2+}, E_{2-}) and (E_{4+}, E_{4-}). For the states labeled 2 and 4, the energy separation within each pair is greatest at $|\vec{H}|=0$, where it is equal to δ, and decreases slowly with increasing $|\vec{H}|$. At a field value of 70 G the energy separation has decreased to about $\delta/2$. The effect of H_w on the levels $E_1 = \bar{E}_3$ $(m_F = +1, m_F = -1)$ and $E_3 = \bar{E}_1$ $(m_F = -1, m_F = +1)$ does not produce a splitting in each of these levels, but simply shifts them to $E_{1+} = E_{3+}$ and $E_{1-} = E_{3-}$, respectively. Each of these shifts is equal to $\delta/2$ making the energy separation between the pairs equal to δ at zero field. The energy shift $\delta/2$ at $|\vec{H}|=0$ decreased to $\delta/4$ at a field value of about 1.35×10^{-4} G. The energy shift decrease to $\delta/20$ at a field value of about 9×10^{-4} G $\approx$ mG.

The energy eigenstates for the M-$\bar{\text{M}}$ coupled system are linear combination of $|M_i\rangle$ and $|\bar{M}_i\rangle$, not $|M_i\rangle$ or $|\bar{M}_i\rangle$ itself. Thus, if the system is initially in the pure muonium state ψ_i $(t=0)=|M_i\rangle$, then at time t it will have developed an antimuonium component equal to

$$\langle \bar{M}_i | \psi_i(t) \rangle = \langle \bar{M}_i | M_{i+} \rangle \langle M_{i+} | M_i \rangle \, e^{-iE_{i+}t}$$
$$+ \langle \bar{M}_i | M_{i-} \rangle \langle M_{i-} | M_i \rangle \, e^{-iE_{i-}t}$$
$$= \begin{cases} i \dfrac{\delta}{W} \sin\left(\tfrac{1}{2}Wt\right) e^{-\frac{i}{2}(E_{i+} + E_{i-})t} & i = 1,3 \\[2mm] i \sin\left(\tfrac{1}{2}Vt\right) e^{-\frac{i}{2}(E_{i+} + E_{i-})t} & i = 2,4 \end{cases}$$

$$(23)$$

where $V = \delta(1 + x^2)^{-\frac{1}{2}}$ is the energy separation of $m_F=0$ states. The probability that the muon decays as a μ^- rather than a μ^+ in an electromagnetic environment by time t is [16]

$$P(\overline{M}_i, t) = \int_0^t dt' \, \lambda \, e^{-\lambda t'} |\langle \overline{M}_i | \Psi_i(t')\rangle|^2$$

$$= \begin{cases} \dfrac{\delta^2}{2(\lambda^2+W^2)}\left\{ e^{-\lambda t}\left[-\dfrac{\lambda^2}{W^2}(1-\cos Wt) - \dfrac{\lambda}{W}\sin Wt\right] + (1-e^{-\lambda t})\right\} & \\ & \text{for } i=1,3 \\ \dfrac{V^2}{2(\lambda^2+W^2)}\left\{ e^{-\lambda t}\left[-\dfrac{\lambda^2}{V^2}(1-\cos Vt) - \dfrac{\lambda}{V}\sin Vt\right] + (1-e^{-\lambda t})\right\} & \\ & \text{for } i=2,4 \end{cases}$$

(24)

wher $\lambda = 3 \times 10^{-10}$ eV (= 0.455×10^6 sec^{-1}), is the muon decay width. For $t \to \infty$, this becomes

$$P(\overline{M}_i, \infty) = \begin{cases} \dfrac{\delta^2}{2(\delta^2+\Delta^2+\lambda^2)} & i=1,3 \\[4mm] \dfrac{\delta^2}{2[(1+x^2)\lambda^2+\delta^2]} & i=2,4 \end{cases}$$

(25)

In the absence of external fields ($\Delta=0$) we obtain

$$P(\overline{M}_i, \infty) \approx \frac{\delta^2}{2\lambda^2} = 2.5 \times 10^{-5} \left(\frac{C_{M\overline{M}}}{C_V}\right)^2 \quad i=1,2,3,4$$

(26)

since $\delta \ll \lambda$. From this expression it clearly follows that external electromagnetic fields will quench the M-$\bar{\text{M}}$ conversion unless

$$\Delta \ll \lambda \tag{27}$$

As long as $\Delta \ll \lambda$, the conversion process will be unaffected; the reason is that as Δ increases beyond δ, $|M_{i+}>$ approaches $|M_i>$ and $|M_{i-}>$ approaches $|\bar{\text{M}}_i>$ for $i = 1$ and 3, but also the interference "beat" between $|M_{i+}>$ and $|M_{i-}>$ speeds up. Figure 3 given the development in time of both $|<\bar{\text{M}}_i| \psi_i(t)>|^2 e^{-\lambda t}$ and $P(\bar{\text{M}}_i, t)$ for the $\Delta = 0$ condition.

A constant electric field does not contribute to Δ, as has been shown in the work of Feinberg and Weinberg.[16] This is true because the only scalars that the energy may depend upon in a state with angular momentum $\vec{F}$ are $|\vec{E}|^2$ and $(\vec{E} \cdot \vec{F})^2$ (since $\vec{E} \cdot \vec{F}$ is pseudoscalar); both scalars are even in $\vec{E}$ so that they are the same for M and $\bar{\text{M}}$. In an inhomogeneous electric field, Δ will contain only odd powers of $\vec{E}$, and since M and $\bar{\text{M}}$ are neutral the lowest term will be of order $|\vec{E}|^3$. A calculation of Feinberg and Weinberg[16] to lowest order in gradient shows that for fields varying in distances of order 1 mm this term gives $\Delta < \lambda$ for $\frac{dE}{dx} < 10^8$ v/cm. We may therefore safely ignore contributions to Δ from any reasonable external electric field. From eq. (25), we see that for small x^2, the transition rate will remain equal to the vacuum rate $2.5 \times 10^{-5} \left(\frac{C_{M\bar{M}}}{C_F}\right)^2$, for the $m_F=0$ states. The 1S M and $\bar{\text{M}}$ states with F=1, $m_F=\pm 1$ are split by a constant magnetic field by an amount $|\Delta| \approx 2\mu_B^e |\vec{H}|$; thus, in order to avoid quenching in these states we have to limit the magnetic field according to equation (27)

$$2\mu_B^e |\vec{H}| \ll \lambda = 3 \times 10^{-10} \text{ eV}, \tag{28}$$

which sets a condition that

$$|\vec{H}| \ll 0.03 \, G.$$

A possible signature of an M$\to\bar{\text{M}}$ transition is the emission of a fast decay e^- with an slow e^+, _i.e._,

$$\bar{M}(\mu^- e^+) \to \text{fast } e^- + \text{slow } e^+ + 2 \text{ neutrinos.} \tag{29}$$

Ordinary muonium decay, by contrast, is

$$M(\mu^+ e^-) \to \text{fast } e^+ + \text{slow } e^- + 2 \text{ neutrinos.} \tag{30}$$

The probability that the e^+ emitted when the μ^+ decays in ordinary muonium ($\mu^+ e^-$) should give up $\geqslant$ 10 MeV of its energy to the bound e^- has been estimated by Feinberg and Weinberg[16], who give a value $\simeq 10^{-10}$; hence a fast e^- is a sure sign that $\bar{\text{M}}$ was formed.

Another signature of M-$\bar{\text{M}}$ conversion (used by Amato et al.[10]) would be to detect the characteristic x-rays following the atomic capture of the negative muon of the $\bar{\text{M}}$ atom in a target placed downstream of the muonium production region. For example, the atomic capture of μ^- in gold would produce 2 MeV (3d $\to$ 2p) and 5 MeV (2p $\to$ 1s) x-rays.

The choice between these two signatures depends in large part upon the overall detection efficiency for events allowed by the experimental setup and the background problems related to the different techniques.

III. THE PRODUCTION OF MUONIUM

A. Introduction

Well known consequences of parity nonconservation[41] in the π-μ-e decay chain are (1) the longitudinal spin polarization of muons in meson beams emerging from synchrocyclotrons and (2) the asymmetric angular distribution of muon decay electrons.[42,43] The decay of a positive pion at rest $(\pi^+ \rightarrow \mu^+ + \nu_\mu)$ produces a positive muon with its spin in the direction opposite to its linear momentum, the μ^+ carrying a helicity of -1. Further, the decay of a positive muon $(\mu^+ \rightarrow e^+ + \nu_e + \bar{\nu}_\mu)$ occurs with an angular asymmetry favoring positron emission in the direction of the muon spin, the e^+ possessing a helicity of +1.

Once polarized muon slows down in matter polarized muonium will be formed upon capture of an atomic electron from an atom of the medium. The polarization of the muons is not changed in the slowing down process, because principally the Coulomb interaction is involved and magnetic forces are small. When muonium is formed, the magnetic interaction between the muon spin and the electron spin can alter the muon spin direction and thus lead to a partial depolarization of the muon.

The distribution of muonium atoms in the four hfs magnetic substates depends on the initial polarization P_0 of the muon beam and on the external magnetic field $\vec{H}$. If P_0 = +1 and $\vec{H}$ is in the longi-

21

tudinal direction (parallel to the muon spin), then the population
probabilities P_i of forming the hfs substates are given by [44]

$$P_1 = \frac{1}{2} \quad ; \quad P_2 = \frac{1}{2} s^2 \quad ; \quad P_3 = 0 \quad ; \quad P_4 = \frac{1}{2} c^2 \; , \tag{31}$$

in which the state designations i are those given in Figure 2 and the
quantities s and c are given in eq. (B-8). The resulting polorization
P of the muons forming muonium is given by

$$P = \frac{1}{2} + \frac{1}{2} \frac{x^2}{(1+x^2)} \; , \tag{32}$$

in which x is defined by eq. (B-6), and is negligible in this experi-
ment.

Unambiguous evidence of muonium production has been sought
with the spin-precession technique.[42] In this process both the effec-
tive asymmetry parameter of the decay positron angular distribution
and the characteristic muonium Larmor precession frequency in a uniform
external magnetic field were obtained in a measurement of the decay
positron time distribution. For a given system with magnetic moment
$\vec{\mu}$ and total spin angular momentum $\vec{F}$ the motion of the spin in a uniform
external magnetic field $\vec{H}$ is given by

$$\frac{d\vec{F}}{dt} = \vec{\mu} \times \vec{H} = \vec{\omega} \times \vec{F} \tag{33}$$

where $\vec{\omega}$ is the Larmor frequency.

The magnetic moment of a free μ^+ is μ_B^μ and its Larmor precession frequency in a transverse magnetic field H (G unit) is

$$|\omega_\mu| = \frac{\mu_B^\mu H}{F} = 2\mu_B^\mu H = \frac{e}{m_\mu}H = 0.085H \ \text{rad.}/\mu\text{sec} \tag{34}$$

since $F = \frac{1}{2}$.

The magnetic moment of muonium depends on the hfs magnetic substate and on H. Under the transverse weak-field condition which we used in this experiment, the small horizontal field components $(x \ll 1)$, together with the value for the ratio of magnetic moments

$$\frac{\mu_B^e}{\mu_B^\mu} = \frac{m_\mu}{m_e} = 207 \ , \tag{35}$$

mean that the magnetic moment of muonium for each polarized hfs substate is dominated by the electron magnetic moment μ_B^e. Therefore, the Larmor precession frequency for muonium in the states 1 and 3 is approximately

$$|\omega_M| \simeq \frac{\mu_B^e H}{F} = \mu_B^e H = \frac{e}{2m_e}H = 8.8H \ \text{rad.}/\mu\text{sec} \ , \tag{36}$$

since the triple state has $F = 1$ (H in G unit). With a muon initially polarized along the beam direction the only muonium Larmor precession which contributes to the decay positron time spectrum is the hfs state 1 $(F = 1, m_F = +1)$, since the probability of forming state 3 is zero.

If muons effectively remain free in the gold targets used,
then the precession of the muon at the free-muon frequency ω_μ^+ should
be observed in this experiment. On the other hand, if the muons dif-
fuse to the gold surface and enter the surrounding vacuum as muonium
in a time short compared to the precession period, then the character-
istic muonium precession frequency ω_M, which is 103 times greater than
ω_μ^+, should be observed.

It is interesting to note that the "beat frequency", which
arises from the transitions between muonium hfs levels in a magnetic
field,[45] does not affect this experiment. The decay positron distrib-
ution function of muonium precession would be modified by the beat
frequency Ω to the form

$$N(t) \propto (1 + a \cos \omega_M t \cos \Omega t)$$

(37)

in which a is the experimental coefficient of the μ-e decay asymmetry,
ω_M is muonium Larmor precession frequency, and beat frequency Ω is
given by

$$\Omega \approx \frac{\omega_M^2}{\omega_0} = \omega_M \frac{H}{2H_0}$$

(38)

In this expression, ω_0 is the frequency of the ground state hfs of the
muonium atom at zero magnetic field, namely, $\omega_0/2\pi = 4463$ MHz and
$H_0 = \frac{\omega_0}{2\mu_B^e} = 1585$ G is the magnetic field at the location of the electron
due to the magnetic moment of μ^+. H is a precession field which is less

than 21 G for this experiment; hence, $\omega_M \gg \Omega$. It is necessary to record a very large number of Larmor precession periods in order to observe a single beat period. Therefore, it is negligible in our experiment, for which only a relatively small number of few cycles have been detected.

The experimental method consisted of measuring the time distribution of decay positrons with respect to parent muons and then in analyzing the data for the characteristic precession frequency ω_M of muonium. For materials where we anticipate only partial formation of muonium the time distribution of the decay positrons, as observed with a fixed counter telescope, should be given by the expression

$$N(t) = N_0 e^{-t/\tau}\left[1 + a_\mu \cos(\omega_\mu t + \phi) + \tfrac{1}{2}a_c R e^{-t/T}\cos(\omega_M t + \phi)\right] + B$$

(39)

where $N_0 = N_\mu + N_M$ is the sum of both free μ^+ and muonium events, at the initial time; τ is the muon mean lifetime; a_μ is the observed free muon asymmetry in the target material; $R = N_M/N_0$ is the fraction of μ^+ stops which form muonium; $\tfrac{1}{2}$ is the probability that the muonium will form in the polarized state $(F, m_F) = (1, +1)$; T is the muonium relaxation time, ϕ is the observed phase angle, and B is the accidental background. In terms of this function a least-squares fit of the data can be made to obtain the unknown parameters. The following section will describe this procedure in further details and give the results of analysis.

B. <u>Experimental Procedure</u>

   1. <u>Beam Characteristics and Experimental Arrangement</u>

        The experiment was performed in three cyclotron runs from September, 1970 through November, 1972 at N.A.S.A. Space Radiation Effects Laboratory (SREL) in Newport News, Virginia. We required a polarized positive muon beam of high purity and low momentum. We chose the "backward-produced" positive muon beam from the muon channel.[46] (The "backward" beam consists of those μ^+ which decay in the backward direction as measured in the pion rest frame.) The beam was almost entirely free of pions and had a muon purity of approximately 95%. The remaining 5% were electrons.

        Figure 4 shows a layout of the muon beam area at SREL. The pions were produced in the 600 MeV synchrocyclotron when orbiting protons were incident on a stationary thin filament carbon "harp" target. The beam was "stretched" such that it had a duty factor of 20%. The pions and the resulting decay muons then traveled through the fringe field of the cyclotron, entering a pair of 12" aperture matching quadrupole magnets which served as a focussing lens for the muon channel beam. The main channel is composed of twenty-four quadrupole magnets. A beam momentum of 90 MeV/c ± 10% corresponding to backward muons was selected with a 18" x 18" dipole bending magnet. The pions, forward positive muons, and negative part-

icles were deflected into the magnetic yoke, while the backward

positive muons went through two additional focussing quadrupole

magnets into the muon cave.

A typical experimental set up is shown in Figure 5.

Although some counters were changed for different targets (as

described in section III B. 5), the general features were the

same for all targets. A 6" thick lead brick wall, with a

8" x 8" opening, served as a first collimator, and was built

against the downstream side of the last quadrupole magnet.

The second lead collimator (2" thick) with a 4" x 4" opening

followed the energy degrader, and was located on the upstream

side of counter 3. All counters from 1 to 10, except 5 and 6,

were made of Pilot B plastic scintillant.[47] They were optical-

ly coupled to Amperex 56 AVP photomultiplier tubes by means of

adiabatic Lucite light pipes. All light pipes were made long

enough to locate the phototubes far from the region of the

precession field. Mu-metal and soft iron cylinders shielded

the phototubes from the effects of the fringing field of the

cyclotron and of the Helmholtz coils. The active areas of

the scintillation counters were:

counter 1 and 2   - 8" x 8" x ¼"

counter 3   - 8" x 8" x 3/8" with 4½" diameter

                hole at the center.

counter 4   - 4½" diameter x ¼" thick disk.

counters 7-10   - 10" x 10" x ¼"

Counters 5 and 6 were especially designed to be sensitive to muons stopping in small mass targets. Both were made of Pilot M plastic scintillant, and were located inside the vacuum chamber. Counter 5 was a 0.001" thick, $4\frac{1}{2}$" diameter sheet of scintillant which was attached to the downstream side of an 1/8" thick, $4\frac{1}{2}$" diameter Lucite light pipe. It was viewed from outside of the vacuum chamber by a 5" diameter RCA C70133B photomultiplier tube with a high gain cathode and gallium-phosphide first dynode. The efficiency of counter 5 was found to be about 50% for stopping μ^+ particles. Counter 6 was a five-sided scintillator cup (3/8" wall thickness) which inscribed a volume of 6" x 6" x 6". This cup was attached to a $8\frac{1}{2}$" long conical Lucite light pipe. It was viewed by a 5" diameter RCA 4522 photomultiplier tube (bialkali photocathode). Both photomultiplier tubes of counters 5 and 6 were protected by Co-Netic magnetic shields[48] from the effects of external magnetic fields. The target vacuum chamber was a 0.032" thick stainless steel cylinder of 10" diameter and 12" length. The center portion of the upstream aluminum end plate was reduced to 1/8" thickness for the purpose of beam transmission. The downstream end plate contained a 5" diameter hole to allow passage of the counter 6 light pipe. The chamber was fit with Nupro valves and a $\frac{1}{2}$" diameter valve for gas handling and evacuation. A vacuum of 10^{-5} Torr was attained with an oil diffusion pumping system.

Coincidences between counters 1 and 2 (12) served as a monitor of the number of particles in the beam. Counter 3, operated in the anticoincidence mode, was followed by counter 4, which was placed against the upstream side of the vacuum chamber. (see Figure 5). Both 3 and 4 together served to control the entrance angle of the beam into the target. A coincidence signal 1 2 $\bar{3}$ 4 5 $\bar{6}$ indicated that a particle had stopped in the target chamber. Counter 5 was made thin so as to reduce the number of false signals (i.e. stops in the counter itself) to a minimum.

The number of muon stops in the target chamber was maximized by studying the variation in stops per monitor count as a function of polyethylene degrader thickness. A typical range curve is shown in Figure 6.

The decay-positron detectors were divided into two symmetric pair. These counter telescopes were located on either side of the vacuum chamber. Counters 7 and 8 were on the left-hand side as one looks downstream and counters 9 and 10 were on the right-hand side. The fractional solid angle subtended by each positron telescope from the center of the target was approximately 8%.

For some muonium runs a 10" x 10" x ¼" aluminum plate was positioned between counters 7 and 8, and between counters 9 and 10, to eliminate the low energy portion of the positron spectrum. The overall asymmetry amplitude in μ^+ decay is

energy-dependent, increasing with increasing energy cutoff.[18,44]
This low-energy cutoff set the positron energy detection
threshold at about 6 MeV. This cutoff thereby increased
the observed absolute asymmetry amplitude by about 0.5%.

A decay positron was indicated by the coincidence
signal $(\bar{2})$ $(\bar{3})$ $(\bar{4})$ 7 8 or $(\bar{2})$ $(\bar{3})$ $(\bar{4})$ 9 10, where $(\bar{2})$, $(\bar{3})$
and $(\bar{4})$ overlapped in an "or" anticoincidence mode. For
the 200 gold-foil target, which had a thickness of 45.5
mg/cm^2 and a total mass of 3.3 g, the μ^+ stop rate was
80/sec (for 65 x 10^3/sec 12's). This corresponds to a
normalized muon stop rate of 24/g-sec. Both decay positron
telescopes recorded events at a rate of 6/sec.

2. Targets

The main target used in this experiment was thin
gold leaf. However, in order to measure beam polarization
and to test our experimental sensitivity to muonium we also
used graphite, fused quartz, and argon gas as targets. For
the solid targets the chamber was evacuated to 10^{-5} Torr.
For the gas target runs the chamber was preevacuated to a
pressure of 10^{-5} Torr before introducing the argon gas. A
brief description of each target follows.

a. Graphite

It is well known that positive muons remain highly
polarized in graphite.[49] Therefore, a graphite measurement
of the asymmetry coefficient provides a calibration of the

product of the quantities: beam polarization, finite decay
counter geometry, and positron energy cut-off correction.
The graphite target used was a thin sheet of dimensions
6" x 4"x1/8" and density 1.41 g/cm^3. This target was
positioned inside the cup-shaped counter 6, and oriented
at 45 degrees to the beam.

    b. Quartz

        Fused quartz, a well known muonium producing
material,[18] was used to test the system for an unambiguous
muonium signal. Two sheets were used, one extremely thin
(dimensions: 6" x 5½" x 1/32"; mass: 38g.), the other
four times as thick as the first. Each was positioned
inside counter 6, angled 45 degrees to the beam.

    c. Argon Gas

        Argon gas is also known to be a muonium-forming
material, although well-defined signals had not been
observed prior to these measurements. Because the argon
mass could be made comparable to the mass of our gold foils
we chose it to test the sensitivity of the system for a
small mass target. The argon gas was rated ultrahigh purity,
i.e., fewer than 20 ppm of contamination.[50] It was main-
tained under a continuous flow condition within the target
chamber at either a pressure of 2280 Torr or 1290 Torr.
The argon mass within the 6" x 6" x 6" target region was
41mg/cm^2 at a pressure of 1290 Torr. We attempted at one

point to purify the argon gas by recirculating the gas through
a heated titanium-zirconium purifier, but the muonium signal
decreased as a consequence.

d. Gold Foils

We used two different target arrangements for the
gold foils in this experiment. The first gold foil target
consisted of an array of 200 commercial gold leaf,[51] and were
each separately suspended by a thin thread from a frame of 1/8"
dia and 0.004" wall stainless steel tubing. The frame, includ-
ing the thread, had a total mass of about 4 g, and for the most
part was located outside of the beam area. Each foil was 8.5
cm x 8.5 cm x 10^{-5} cm, so that the total weight of 200 foils
was 3.3 g. The foils were separated from one another by ~0.08
cm on the average, thus filling the 6" length of the active
target region. For μ^+ particles stopping in these gold foils it
was anticipated that a certain number, upon diffusing to the
surface, would enter the vacuum region in the form of polar-
ized muonium. The interval between foils was such that ther-
mal muonium atoms in the vacuum space could be expected to
undergo two to three uninterrupted cycles of muonium preces-
sion on the average if the precession field was ~10 G. In
addition, a calculation of μ^+ diffusion time at room temper-
ature shows that the μ^+ ion is capable of traversing a half-
foil thickness in $t = \frac{x^2}{2D}$ ~40 nsec, a time short compared to
the expected muonium precession period, where x = half-foil

thickness and D is the μ^+ diffusion coefficient in gold at 25°C.

The second gold foil target consisted of 800 gold leaf confined to the same volume defined by the 200 foil target. These foils were simply bunched randomly in order to rduce significantly the vacuum space available for uninterrupted muonium precession.

e. Empty Target

Empty target runs were made in which a duplicate frame, minus gold foils, was positioned in the counter 6 cup. This permitted us to determine to what extent μ^+ stops in the frame, in counter 5, or in the deadlayer of counter 6 contributed to the muonium signal.

f. Gold Foils in Argon

The 200 gold-foil target was introduced into the argon gas either at a pressure of 2280 Torr or 1290 Torr to study how this compound target would affect the muonium signature. The number of muons stopped inside any fraction of a compound target is proportional to the number of grams of that fraction of target. If the muons which stopped in the gold foil does not form muonium, the fraction of muonium formation rate should be reduced by a considerable amount.

3. Magnetic Field

A uniform precession field was provided along the vertical direction by a pair of 23" diameter Helmholtz coils separated by 11.5". We defined "+" for field pointing up and "-" for field pointing down. The coil current was supplied by a Sorenson Nobatron DCR 300-8A power supply and monitored by a digital voltmeter (DVM) which was located in the counting area. The DVM reading showed that the current remained highly stable over the course of each experimental run. We found that the cyclotron fringe-field contributed a 3 G vertical field as well as a non-zero horizontal field at the target position. It was necessary for us to use two pairs of bucking coils to eliminate the horizontal components to less than 100 mG. For the argon gas runs we used the cyclotron fringe field alone to precess the muonium spin.

The field in the target region was carefully mapped with the aid of a Hall probe[52] whenever targets were interchanged. It showed that the variation of magnetic field intensity was less than ± 50 mG through out the target region. The magnetic field was also calibrated in four special runs. Among these were one graphite, one 800-gold foil, and two quartz runs. We fit the data of the graphite and gold target to the free muon precession function. By using a least-squares method to obtain the precession frequency, we then calculated the corresponding magnetic field.

The results were all consistent with the magnetic field measured by the Hall probe technique. Figure 7 shows a plot of the magnetic fields used in each run versus the observed frequencies.

4. Electronic Logic

A typical block diagram of the logic circuitry used in the precession experiments is shown in Figure 8. Although there are two cyclotron runs in which we used only one decay telescope and a 100 MHz digital timer instead of the time to amplitude converter (TAC), the general features were the same for most experimental runs. All the units shown in Figure 8 were modular in form and were manufactured commercially. Blocks labeled D are standard discriminators (Chronetics model 154 or E. G. & G. model T105/N) and those labeled C are coincidence units (E. G. & G. model C203/N or Chronetics model 152). The main purpose of this circuitry was to define a stopping muon and to determine in time interval between each positron event relative to the μ^+ stop signal.

The fast outputs from the beam telescope counters 1-6 were fed through delay boxes to discriminators D1-D6. The shape outputs of discriminators formed the necessary inputs to the coincidence units as shown in Figure 8. The output of each relevant coincidence unit was scaled. A 12 coincidence served as the beam monitor; $1\ 2\ \bar{3}\ 4\ 5 \equiv I$ specified the arrival of a beam particle in the target region; $1\ 2\ \bar{3}\ 4\ 5\ \bar{6} \equiv I\bar{6}$ indicated the particle had stopped in the target. Given the poor pulse height and time jitter

response of the 1 mil counter 5, we chose to make counter 4 the time-determining counter in the stopping signature. For this reason the D4 output (4_r) was narrowed to 5 nsec (FWHM). The true stopped muon was then indicated by $\overline{16}4_r$.

As a precaution, we checked for "second" and "previous" muons; i.e., we ascertained that expept for 2% of the cases, the muon associated with the observed decay positron was neither preceded nor followed by another stopped muon within the observation time of 4 μsec. The 2% effect is negligible and we therefore removed this "protective" circuitry from the logic sequence for the sake of simplicity.

The fast outputs from the positron telescope counters 7-10 were also fed through delay boxes to discriminators, which fed coincidence units in turn. The fast coincidence 7 8 and 9 10 were vetoed by a prompt pulse from either 2, 3, or 4 to eliminate direct spray from the beam. Thus the decay positron signal was either an $e_L \equiv (\overline{2})\ (\overline{3})\ (\overline{4})\ 7\ 8$ or an $e_R \equiv (\overline{2})\ (\overline{3})\ (\overline{4})\ 9\ 10$. A delay of 0.4 μsec was placed in the positron circuits. Discriminators D13 and D14 were used to reshape the logic signal following the delay, and their outputs represented the decay positron signals which should be analyzed.

The time interval between a true stopped muon $\overline{16}4_r$ and the subsequent decay positron, either e_L or e_R, was determined by separate TAC[53] units (or a 100 MHz digital timer[54]). The TAC outputs were finally sorted by a dual ADC pulse height analyzer

(PHA)[55]. The muon stop signals were used as a "START" pulse to the

TACs which were set for a range of 4 μsec. The decay positron sig-

nal was used as a "STOP" pulses to the TAC and was delayed a fixed

0.4 μsec relative to the muon. This permitted a study of "negative

time" events, i.e., random background. Thus, good decay-positron

events e_L or e_R were defines as those which occurred within 3.6

μsec after the time of arrival of a positive muon.

The time resolution was slightly different for the

left and right systems, due to the fact that different TAC units

were used. The calibration for the left system was 1.87 μsec per

channel; for the right system it was 1.80 μsec per channel.

5. Data Collection

During the graphite, quartz and most of the gold foil

in vacuum runs a Nuclear Data 4096 channel PHA[55] and magnetic tape

recording system were used for data acquisition. The PHA operated

in a dual mode, with the first 2048 channels devoted to the decay

positron events e_L and the remaining 2048 channels used for the

decay positron events e_R.

For the various argon gas runs and the particular

gold foil run at a magnetic field of H = -7 G taken September 1970,

we set up only the left positron telescope. In addition, a 100 MHz

digitron replaced the TAC as a timing device to measure the time

interval between the occurrence of the muon stop and the subsequent

decay signal. The signals were fed through the SREL IBM 2972/7

interface to an IBM 360/44 computer. All data taken by this method were put onto magnetic tape and cards.

For the graphite target, data were taken at the magnetic field of + 31 G. Before making a search for muonium production in the gold foils, data were collected from the quartz targets at field of + 10 G, - 4 G, and - 10 G. Typical timing spectra for e^+ events in graphite (H = + 31 G) and quartz (H = - 4 G) are shown in Figure 9 and Figure 10, respectively. These spectra are less than 4 μsec in extent and are characterized by a 2.2 μsec exponential modulated by pronounced sinusoidal precession signals. The characteristically higher frequency of muonium versus the free muon is readily apparent here.

Searches for muonium production in small mass targets were taken in the following sequence: low pressure argon (2280 Torr and 1290 Torr), low pressure argon with 200 gold foils introduced, 200 gold foils in vacuum, and 800 gold foils in vacuum. The cyclotron fringe field (H = -3 G) was used to precess muonium when argon runs were involved. The magnetic fields used for the 200 gold-foil runs were sequentially -7, -9.3, +8.4, -5 and -10.5 G. The magnetic fields used for the 800 gold foil runs were -5 and + 21 G. Typical sets of PHA data for the argon (2280 Torr) and gold foil (H = + 8.4 G) run are shown in Figure 11 and Figure 12, respectively.

Target empty runs consisting of the bare frame were taken at magnetic field of -3 and -9 G. The ratio of the μ^+ stop

rate $\bar{I}64_r$ to the incident beam intensity I was found to be 1.1%
for the frame only, whereas the same ratio for the 200 gold foils
in vacuum runs was 1.7%.

6. Calibration

The method employed to calibrate the TAC-ADC system
was that suggested by E. G. & G., Inc.[56] A block diagram of this
is shown in Figure 13. A 10 kHz signal, derived from "TRIGGER OUT"
of a time mark generator,[57] served as the start pulse to the TAC.
A fixed frequency signal, 10 MHz, from the "MARKER OUT" of the
time mark generator, which was randomly gated by a pulse from a
radioactive source(Ru^{106}) through a coincidence unit, was used as
stop pulses for the TAC. A spectrum evenly spaced peaks of equal
amplitude was then obtained, with a spacing of 100 nsec. The aver-
age width between two peak was (53.5 ± 0.3) channels and (55.5 ±
0.1) channels for left and right system, respectively. The calcul-
ated channel width for the left system was 1.87 nsec per channel
and was 1.80 nsec per channel for the right system.

In order to determine the spectrum time t = 0 cor-
rectly we performed a special run with $\bar{6}$ removed from the logic
circuitry. The coincidence signal 1 2 $\bar{3}$ 4 5 became a start pulse
and the corresponding decay or scattered signal ($\bar{2}$) ($\bar{3}$) ($\bar{4}$) 7 8
or ($\bar{2}$) ($\bar{3}$) ($\bar{4}$) 9 10 was the stop pulse as before. This resulted
in a sharp timing spike corresponding to beam scattered events
and hence determined the positions of t = 0.

C. Data Analysis

1. General Technique

Decay positron time distributions were fit by a non-linear least-squares method[58] (see Appendix C for detail) to the generalized function:

$$N_k(t) = N_0^k e^{-t/\tau} \left[1 + a_\mu \cos(b\omega_M t + \phi_k) \right.$$
$$\left. + \frac{1}{2} a_c R e^{-t/\tau} \cos(\omega_M t + \phi_k) \right] + B_k \qquad (40)$$

The function $N_k(t)$ was associated with the number of decay positron events detected either in the left positron telescope ($k \to \ell$) or in the right positron telescope ($k \to r$). The first oscillating term in this expression accounts for the slowly varying free muon precession which is characterized by the free μ^+ precession frequency ω_μ. The second oscillating term accounts for the rapid variation of muonium precession at the characteristic frequency ω_M. The parameters are defined as follows (with the k label suppressed):

N_0 is the initial amplitude at time t = 0 and is the sum of both free μ^+ and muonium events, namely $N_0 = N_M + N_\mu$, where N_M is the number of stopped muons forming muonium in any (F, m_F) substate and N_μ includes all stopped muons which maintain the character of free μ^+ particles,

τ is the μ^+ mean lifetime of 2.2 µsec,

a_μ is the empirical free muon asymmetry,

a_c is the calibration signal measured for μ^+ stopping in

graphite. It is related to the theoretical value of 1/3 by the expression $a_c = 1/3 \ P_0 \ f_\Omega \ f_E \ (1 - D)$, where P_0 is the initial polarization of μ^+ in the incident beam, D is the depolarization factor by which the initial muon polarization is reduced as the particle is brought to rest, f_Ω is a correction factor associated with the finite positron detector geometry, and f_E is an energy cutoff correction factor arising from the condition that only positrons above a low energy threshold were able to trigger the decay telescope,

R   is the fraction of stopping μ^+ which form muonium, <u>i.e.</u>, $R = N_M/(N_M + N_\mu)$, both polarized and unpolarized,

½   is the probability that muonium will form in the polarized state $(F, m_F) = (1, 1)$,

T   is the muonium relaxation time, characteristic of the medium,

ω_M is the muonium Larmor precession frequency,

b   is a scaling factor which is equal to the ratio of the free muon Larmor frequency to that of muonium, namely $b = \omega_\mu/\omega_M = - 1/103$,

ϕ_k represents the average phase angle for each positron detector. For the left telescope the angle ϕ_ℓ was measured from the initial beam polarization axis to the center of the left telescope. The angle ϕ_r was related to ϕ_ℓ by defining $\phi_r = \phi_\ell + \phi_0$ where ϕ_0 is the

opening angle between two telescopes, and

B   is a measure of the accidental background.

The variable parameters a_μ, R, ω_M, and T were common to both systems while N_0^k, ϕ_k, and B_k were sensitive to the small differences between the left and right telescopes. The fitting was performed with left and right data simultaneously using an iterative process in order to determine unique values for common parameters. The convergence limit for parameters was set at 1%. Because the common parameters were adjusted to fit both left and right data simultaneously, a single value of the χ^2 characterized the fit to both telescope spectra.

Since the intensity of the muonium signal varied greatly from target to target, it was not possible to fit all free parameters simultaneously in most data sets. We applied the fitting procedure to data in the following sequence: graphite, quartz, argon and finally the gold foil data. From the graphite data we determined the parameter a_c, which included the beam polarization, a detector geometry correction, and positron energy cutoff correction. Where the muonium signal in quartz and argon was large, we were able to fit simultaneously all five parameters, with a_μ set equal to zero. In the gold and frame only data the number of fitting parameters was reduced with the aid of the information from the graphite, quartz and argon parameter analysis.

2. Graphite

The asymmetry coefficient a_c was obtained in a control experiment performed with a graphite target. It is well known that a positive muon does not depolarize in graphite, and that graphite data is only characterized by the slow precession signature of the free muon (refer to Figure 9). The analysis of the data to obtain the asymmetry parameter was therefore based on eq. (40) with parameter R set equal to zero. A fit was performed to the free parameters N_0^k, a_μ, ω_μ, and ϕ_k, where $a_\mu = a_c$, $\omega_\mu = - b\omega_M$. Here, as elsewhere in our work, the background B_K was selected as the average value accumulated in the "negative" time channels. $\phi_o = 3.86$ radians was the constant phase difference between left and right positron telescopes.

A thin sheet of graphite was used as a beam calibration target because its small stopping power (0.5 g/cm^2) provided a negligible energy correction to the (μ - e) asymmetry. About 1.2×10^6 events were taken during this graphite run in a magnetic field of H = +31 G. The value of parameters obtained from the data analysis were as follows:

$$a_c = 0.176 \pm 0.002; \qquad \phi_\ell = 1.44 \pm 0.02 \text{ radians}$$

$$\omega_\mu = 0.43 \pm 0.02 \text{ MHz/sec}; \quad B_\ell = 33$$

$$\chi^2/\nu = 2.0 \text{ where } \nu \text{ are the total number of degrees of}$$

freedom.

In this expression $a_c = 1/3 \, P_0 \, f_\Omega \, f_E (1-D)$. If we assume $D = 0$ for graphite and calculate $f_\Omega = 0.95$ and $f_E = 1.006$ for this target, we find that the beam polarization $P_0 = 62\%$.

Because the target region was defined by counters 5 and 6, the correction for the positron telescope angular acceptance f_Ω should be the same for all targets used in this experiment, i.e., $f_\Omega^C = f_\Omega^{quartz} = f_\Omega^{Ar} = f_\Omega^{Au}$. In addition, the contribution to the positron energy cutoff correction to the $(\mu - e)$ asymmetry is negligible for this thin sheet of graphite, as well as for the small mass targets which are described in the following subsection, i.e., $f_E^C \simeq f_E^{quartz} \simeq f_E^{Ar} \simeq f_E^{Au}$. Therefore, the experimental value of the parameter a_c which was obtained in this graphite run is a good calibration for the following runs in small mass targets.

3. Quartz

The function $N(t)$ of eq. (40) with parameter $a_\mu \simeq 0$ was expected to represent the quartz target data (refer to Figure 10). Fits were therefore made to the parameters N_0^k, R, T, ω_M and ϕ_k simultaneously, subject to the choice $a_\mu \equiv 0$. Here, as elsewhere in our search for muonium, the empirical parameter a_c was that obtained from the graphite target analysis. Figure 14 shows typical left-right muonium signals in quartz with H = -4 G in the reduced form $(N_k(t) - B_k)/e^{-t/\tau}$. The solid curve represents the best fit to the muonium part of eq. (40). The results of three separate runs are shown in Table 2. The excellent χ^2 values support the decision to ignore the possible presence of a free muon

signal. The fraction of positive muons that form muonium in the thicker quartz sample was 0.66 ± 0.04. This value is lower than values reported by others.[18] We feel this discrepancy was due to purity differences in the various fused quartz samples since our considerably thinner argon target provided a larger signal than that of quartz. The results for T and ϕ_ℓ for two 1/8" quartz runs at different fields are not in agreement. The reasons are not known at present.

In eq. (40), we should expect a high correlation between the parameters T and R. In order to avoid false fits due to such a correlation, we have calculated χ^2 distributions as a function of various (R,T) combinations, all other parameters held fixed at their nominal values. Figure 15(a) shows the mapping of χ^2 contours for the case of 1/8" quartz with H = -4 G. The minimum χ^2 point, i.e., χ^2_{min} represents the best fit values of R and T. The one, two, and three standard deviation curves, corresponding to χ^2 changing to χ^2_{min} + 1, χ^2_{min} + 4, and χ^2_{min} + 9, respectively, are a measure of the parameter correlation. The results are consistent with the results given in Table 2 for which the more general five parameter fit was made.

A value of 0.45 ± 0.06 was obtained for R for the 1/32" thick quartz sheet, decidedly smaller than that for the 1/8" thick target. Again this result was felt to be possibly linked to questions of sample impurities, or possibly related to a modification in the counting logic, in which for the 1/32" run we demanded a

6 7 8 coincidence for an e^+ signature instead of simply 7 8. It was originally thought that a study of muonium signal-to-noise versus target thickness could be made with quartz. Our results with argon gas proved to serve this purpose better, so that the main role played by the quartz data was one of calibrating the muonium frequency versus Helmholtz current.

4. Argon and Gold Foils in Argon

Further tests of the sensitivity of the system were made by searching for muonium signals in argon gas at low pressures of 1290 Torr and 2280 Torr, both with and without the 200 gold foil target. All gas data were fit by eq. (40) with $a_\mu = 0$, as for the quartz analysis. (refer to Figure 11) In addition, a separate Fourier frequency analysis was made for the gas data. Five parameter fits were made for N_ℓ, R, T, ω_M and ϕ_ℓ. Since $\phi_\ell = 1.37 \pm 0.12$ radians was obtained in these fits (consistent with the graphite results) we repeated the fitting procedure, while fixing $\phi_\ell = 1.37$ radians. Figure 16 shows a best fit (solid curve) to the observed muonium signal in the case of 2280 Torr argon with H = -3.0 G in the reduced form $(N(t) - B)/e^{-t/\tau}$. This clearly indicates that an excellent muonium signal-to-noise can be achieved in a small mass target arrangement. In fact, this represents the first unambiguous precession signal obtained in argon or any other gas. Values of the adjusted parameters and χ^2/ν, where ν is the number of degrees of freedom in the fit are summarized in Table 2

for cases of (a) argon gas at 2280 Torr pressure, (b) 200 gold
foil in 2280 Torr argon gas, (c) argon gas at 1290 Torr pressure,
and (b) 200 gold foil in 1290 Torr argon gas. Figure 15(b) shows
the results of a study of the correlation between the parameters
R and T for argon gas at 2280 Torr.

The method of frequency analysis is known to be very
sensitive to the situation in which a signal is comparable in
intensity to the background. Each point in the frequency analysis
represented the best-fit value of parameter R for a particular
choice of ω_M (all other parameters fixed at nominal values). The
value of ω_M was then incremented and the process repeated many
times. Figure 17 shows the results of this analysis as a plot of
best-fit R as a function of $\omega_M/2\pi H$. The points indicated positions
for which the analysis was made; the error bar shown is a typical
one standard deviation. Each solid curve is a theoretical line
shape computed from the time distribution function of eq. (40)
reducted to the form $\delta N(t) = N(t) - N_\ell e^{-t/\tau} - B$ [refer to section
III C.5 eq. (41)]. Essentially these curves are the Fourier trans-
form of $\delta N(t)$. The central maxima of the resonances were calculated
using the muonium precession frequency ω_M predicted from eq. (36)
for the measured value of H. The values of T were predetermined
from the earlier best fit analysis to four parameters. The peak
amplitudes of the calculated line shapes were normalized to the
peak value of R obtained in the Fourier analysis.

The fraction R of muonium formation was found to be 0.85 ± 0.09 for 2280 Torr argon, and 0.64 ± 0.16 for 1290 Torr argon. These results confirm the predictions of almost total formation of muonium in argon gas.[21] In particular, since the thickness of the 2280 Torr target (73 mg/cm^2) was similar to that of 200 gold foil target (46 mg/cm^2) we demonstrated that the target chamber construction was suitable for revealing muonium evidence in small mass targets.

Introducing the gold foils into the Ar gas did not cause a reduction in R. The results were R = 0.98 ± 0.12 for 2280 Torr argon plus 200 gold foils and R = 0.85 ± 0.15 for 1290 Torr argon plus 200 gold foils. A comparision of the Ar results with those of Ar plus 200 Au foils show that the introduction of the foils in no way degraded the muonium signal. In fact the tendency was to increase the signal. This observation is rather difficult to interpret unless we introduce a mechanism whereby the thin foils themselves participate in the formation of muonium, since it is well known that (i) a positive muon stopped in thick metal targets precesses as a free muon, and (ii) the number of muons stopped inside any constituent of a compound target is proportional to the thickness (g/cm^2) of that constituent of the target. One interpretation consistent with what we have observed would be that some of the positive muons which stopped in the thin gold foils managed to escape the thin foils as muonium in a time short compared to one cycle of muonium precession. These results encouraged us to look for muonium formation separately in the foils. The analysis of data taken for gold foils in a vacuum

environment will be treated next.

5. Gold Foils

In analyzing the gold foils in vacuum data we found that allowing for both a free muon signal and a muonium signal in a given run produced a better fit in terms of a lower χ^2 value. As before we assumed that the functional form of eq. (40) best represented the observed spectra. The analysis procedure involved the following steps: first the data points taken over the full 4 μsec interval were fit to the time distribution function $N_k(t)$ of eq. (40) in which the parameter R was set equal to zero and the phases ϕ_K were fixed at values determined in the graphite and quartz runs. This fit determined to a rather good approximation the parameters N_0^k, a_μ, and ω_μ. Figure 18 shows a typical set of data in the modified form $\delta N_k(t) = [N_k(t) - B_k - N_0^k\, a_\mu e^{-t/\tau}\cos(b\omega_M + \phi_k)]/e^{-t/\tau}$ $= N_0^k [1 + \tfrac{1}{2} a_c\, R\, e^{-t/T} \cos(\omega_M t + \phi_k)]$, in which each data point has been corrected via subtraction for the free muon precession and the background, finally the decay exponential was removed. The remaining $\delta N_k(t)$ should be due principally to the rapidly oscillating muonium term of equation (40).

As a second step we sought to determine the relaxation parameter T by performing a χ^2 mapping versus the two adjustable parameters R and T. This procedure was applied earlier to the quartz and argon data. The analysis was limited to data intervals corresponding to the first two muonium cycles. A closed contour

curve corresponding to one standard deviation was achieved for
which the H = -7 G data gave R $= \left(0.39 \begin{smallmatrix} + & 0.43 \\ - & 0.19 \end{smallmatrix} \right)$ and T = $\left(200 \begin{smallmatrix} + & 200 \\ - & 100 \end{smallmatrix} \right)$
nsec. Relaxation times in this range are consistent with the
proposed mechanism wherein thermal muonium precesses as it travels
between the successive foils.

Selecting the best-fit values for N_0^k, a_μ, ω_μ, and T from
steps (1) and (2) we executed a frequency resonance search for a
muonium signal. As described in section III C. 4 this was a least-
squares fit to parameter R for a given selection of ω_M, all other
parameters held constant. These fit were repeated many times, each
time incrementing the value of ω_M. From this analysis the best-fit
values of R were plotted against the associated values of $\omega_M/2\pi H$ to
reveal possible evidence of a resonance in the R signal. Again data
intervals limited to the first two muonium precession cycles were
chosen. Figure 19 shows the results of the data analysis for the
cases in which polarized muons were stopped in the 200 gold foil
target with (a) H = +8.4 G,(b) H = -10.5 G, (c) H = -9.3 G, (d)
H = -7.0 G, and (e) H = -5.0 G. The plotted points are obtained
from the data analysis; the error bar represents one standard
deviation error. Each solid curve is a theoretical calculation
of the Fourier transform of the oscillating distribution function

$$\Delta N(t) = C_0 e^{-t/\gamma} e^{-t/\tau} \cos(\omega_M t + \phi_K)$$

(41)

in which C_0 is a normalization constant. Its central maximum was chosen at the muonium precession frequency ω_M corresponding to the measured field H as predicted from eq. (36). The curves were computed with the values of T and ϕ_k determined from previous best fits to the data. The theoretical curve was essentially normalized so that the peak value of the curve equals the peak value of the data analysis. The full-width at half maximum resulting from the χ^2 analysis correlated well with the muonium relaxation time T.

Peaks are clearly observed at the anticipated muonium frequency in four cases, but not for the one case of H = -5 G. The amplitudes of the four resonances are 2.5, 2.5, 3.5, and 3.5 standard deviations above zero. Table 3 provides the detailed results of this analysis. The amplitudes of the resonances vary between 24% and 45%, but overlap within an error of one standard deviation. The null result at H = -5 G could possibly be due to a condition of too low a precession field. If the muonium atoms traverse the foil interval of 0.8 mm at thermal velocity (6 x 10^5 cm/sec), only one precession cycle could occur at the muonium frequency corresponding to 5 G. This might be too severe a condition to permit detection. This type of speculation can also be applied to the runs of 800 gold foils where no signal was observed. Figure 20 shows the results of analysis obtained for positive muons stopped in the target of 800 gold foils ($\frac{1}{4}$ the spacing of 200 foils) with H = -5 and +21 G. The null results here rule out the possibility that the signal for R in the 200

foil runs was due to muonium atoms attached or adsorbed to the foil surface.

Agreement between the experimental values of the resonant frequencies and the predicted values is within 3% in all cases. We note that the predicted value of $\omega_M/2\pi H = 1.4$. We obtained an average weighted amplitude[59] for the resonance singal R equal to $(35 \pm 6)\%$.

6. <u>Frame Only</u>

The analysis procedure for positive muons stopped in the target consisting of an empty frame was the same as that just described for the gold foils plus frame in vacuum. Figure 21 shows the results of frequency analysis for data taken at magnetic fields of $H = -3$ G and -9 G. No muonium resonance peak resulted from the analyses. This result was anticipated since plastic scintillator is known not to form muonium,[60] and muons stopped in the steel frame would remain free. The fitting results for the empty target data also appear in Table 3.

IV. MUONIUM-ANTIMUONIUM TRANSITION IN FREE SPACE

A. Introduction

If the lepton number conservation law, as described in Section I., is multiplicative in form, then the $M \rightarrow \bar{M}$ conversion is possible. The eigenstate of the total Hamiltonian including H_w is a mixture of muonium and the antimuonium states. If a system starts as muonium, an antimuonium component should begin to develop with time. The growth of the antimuonium component is strongly retarded by the fact that 1) conversion time is approximately 142 $(C_V/C_{M\bar{M}})$ times longer than the muonium lifetime of 2.2 µsec; and 2) any strong environmental quenching might break the degeneracy between the M and $\bar{M}$ system thereby inhibiting the conversion rate even further. These effects have been detailed by Feinberg and Weinberg[8,16] and described in Section II.B. Therefore, we chose to bypass the environmental problem altogether by seeking $M \rightarrow \bar{M}$ evidence with M atoms which would be produced at the surface of gold foils and released to a vacuum drift space.

The $M \rightarrow \bar{M}$ coupled system might break up in either the muonium or antimuonium state. If break up comes from the muonium state component it takes place exclusively by the μ^+ decay process

$$(\mu^+ e^-) \rightarrow \text{fast } e^+ + \text{slow } e^- + \bar{\nu} + \nu$$

with a lifetime of 2.2 µsec. If the break up takes place from the

$\bar{M}$ state component, it may be from μ^- decay

$$(\mu^-e^+) \to \text{fast } e^- + \text{slow } e^+ + \nu + \bar{\nu}$$
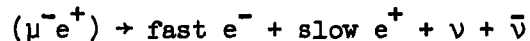
or by μ^- nuclear absorption following an inelastic collision with an
atom in the drift space.

Electrons arising from the decay of negative muons exhibit
the well known shape of the Michel spectrum with a maximum energy of
53 MeV and an average energy of 37 MeV. There are several advantages
in using these electrons as a signature of conversion to $\bar{M}$ compared
to seeking μ^- characteristic x-rays following an $\bar{M}$ inelastic collision.
First, the high energy electrons afford a prominent feature to distin-
guish individual real events from background events. Second, the pro-
bability that one will observe the μ^- decay of the $\bar{M}$ component up to
time t compares favorably to the probability that the M-$\bar{M}$ system will
disappear through an $\bar{M}$ inelastic collision at time t. Finally, the
detection techniques for high energy electrons are relatively straight
forward, and reasonable detection efficiencies can easily be achieved
with large spark chambers. In dealing with high energy electrons or
positrons one must worry about severe degradation of the particle
energy spectrum through the bremsstrahlung process or even the
bremsstrahlung process followed by pair production. This was a serious
factor in the analysis that follows since 0.3 radiation lengths of iron
were positioned between the target region and the spark chamber to
eliminate electromagnetic quenching of the M-$\bar{M}$ conversion.

B. <u>Experimental Procedure</u>

1. <u>Beam and Experimental Set Up</u>

The conversion experiment was performed in the same beam described for the muonium production studies in Section III. B. 1. The experimental arrangement is shown schematically in Figure 22. A 2" thick lead collimator with a 4" x 4" aperture followed by the polyethylene (CH_2) moderator was positioned against the upstream side of the vacuum chamber.

Seven scintillation counters were used in the experiment. Counters 1, 2, 3 and 4 served to define the muon stops. Counters 5, 6, and 7 were the elements of the decay electron telescope. Counters 1 and 2 again formed the beam monitor. Both 3 and 4 were located inside the vacuum chamber. The last defining counter 3 was a 1/32" thick, 4½" diameter sheet of scintillant, which was essentially directly coupled to the photocathode of the 5" dia-meter RCA C70133B phototube. In this arrangement the phototube was inside the vacuum chamber, facing the target region down-stream. Counter 4 was exactly the same as counter 6 in the muon-ium production experiment (see Section III. B. 1). The muonium producing target consisted of two layers of 1000 Å gold foil and was positioned on the downstream side of scintillator 3. It covered the entire downstream surface of counter 3, and also per-formed the function of isolating the light collection between

counters 3 and 4. The total target mass was effectively that of the gold foil and counter 3. The mass of the gold foil was 0.5 mg/cm^2; that of counter 3 was 78 mg/cm^2. The mass ratio of gold foil to total target was 0.6%. The conversion region for M-$\bar{M}$ was encircled by counter 3 and the five-sided counter 4. The vacuum chamber was lengthened to 25" so as to accommodate the counter 3 phototube. The pressure within the chamber was maintained at $<10^{-5}$ Torr. The chamber itself was located within three layers of concentric cylindrical magnetic shielding which shall be described in detail in Section IV. B. 4.

The first gap of the spark chamber spectrometer (see Section IV. B. 2 and IV. B. 3) was located 30" away from the center of the conversion region and in a direction perpendicular to the beam. The entire spectrometer system including the camera was housed in a dark room constructed of black vinyl.

The decay-electron telescope involved either counters 4, 5, 6 or 4, 5, 7. The areas of these counters were: counters 5 - 8" x 7" x 1/8", counter 6 - 24" x 7" x ¼", and counter 7 - 14" x 6" x ¼". The active plastics of 5, 6, and 7 were positioned in the gap of the analyzing C-magnet. Long Lucite lightguides carried scintillation light to phototubes (Amperex 56AVP) located in the weak fringe field. The photomultiplier tubes were shielded by mu-metal and soft iron cylinders from the effects of the magnetic field. Counter 5 was located just before the first gap of the spark chamber, and subtended an average fractional solid angle at the drift region

of about 3.5×10^{-3}. Counter 6 was located along one side of the chamber, and counter 7 followed the last gap of the chamber.

The number of stopped muons were defined by the coincidence 1 2 3 $\bar{4}$ and the decay-electrons by the coincidence $\bar{1}$ 4 5 (6 or 7). Typical rates were: 1 2 = 75 x 10^3 sec^{-1}, 1 2 3 $\bar{4}$ = 200 sec^{-1}, and $\bar{1}$ 4 5 (6 or 7) = 3 min^{-1}.

2. Spark Chamber

The optical spark chamber was located inside a wide gap C-type magnet which operated at a 1.5 kG central magnetic field. It was viewed steroscopically through a large cylindrical lens by a 35 mm camera. This camera was triggered by electron telescope events which followed μ^+ stop pulses within 4 μsec. Figure 23 illustrates details of this chamber which in many ways was a duplicate of the Langley Research Center chamber.[61]

The chamber consisted of 50 gaps, each 0.5" wide. Gaps were formed by alternately sandwiching fifty-one 0.001" thick aluminum plates between 0.5" thick Lucite frames. Both ends of the chamber were protected by a 0.125" thick Lucite plate. Alternate plates were at high potential with the end plates maintained at system ground. Gas inlet and outlet tubing were attached to one side of each frame.

The active area of each gap was a rectangle of 8" width and 5 3/4" height. The overall external dimensions of the chamber were 9" width x 6 3/4" height x 25" length. The frames were

fabricated to the specifications of optical flatness and finish.

The thickness of the aluminum plates was selected to be 0.001" so as to minimize electron interactions and energy loss in at the plates themselves. The gap thickness of 0.5" permitted the chamber to sustain at least six or more multiple tracks with better than 90% efficiency at a firing rate of 5.5 times per second. This specification is extremely sensitive to gas purity, and to the length and geometry of the electrical lines from the high voltage pulsing subsystem to the chamber. The gas fill was a Penning mixture consisting of 90% neon and 10% helium supplied to the spark chamber in a continuous flow condition. The rate of gas flow and excess pressure were pre-determined by several testing runs. It was made rapid enough to prevent build-up of outgassing contaminants and high enough in pressure to prevent backstreaming of air. Spark chamber gas integrity was checked with a Model 21-100 Gas Leak Detector.[62]

The high- voltage pulsing sub-system was manufactured by Science Accessories Corporation.[61] It consisted of (1) one Model 022 spark gap driver amplifier with five trigger outputs; (2) five Model 013 spark gaps; (3) one clearing field power supply 0-3 kV; (4) one high voltage power supply 0-22 kV; (5) one fanout unit incorporating the five Model 013 spark gaps and suitable circuitry (see Figure 24) for distributing high voltage and fields to the gaps.

The Model 022 accepted a trigger signal from the scintillation counters and delivered in parallel five high voltage pulses

to the fanout units, which trigger the five 013 spark gaps. Each of the spark gaps distributes high voltage to ten chamber gaps. The fanout unit delivers high voltage to the chamber plates directly to minimize rise time losses and maximize efficiency. A low voltage clearing field of 40 volts was applied across each gap.

Seven neon light fiducial marks were mounted on the spark chamber at different locations. They were connected in parallel to the high voltage trigger system and could be fired concurrently with the spark. These fixed fiducial marks were used to identify the proper location of the particle tract.

3. Magnetic Spectrometer

The magnetic spectrometer used in this experiment was a wide gap C-type magnet.[63] It had a pole tip with a dimension of 27" length x 11½" width. The separation between the pole tips was 15". It was large enough to house the spark chamber, the fanout unit, the lens, and the mirror. The field was carefully mapped with a Hall probe and digital voltmeter under experimental conditions. For each run the field polarity was set for the appropriately charged (i.e., e^- or e^+) particles which were being observed.

4. Magnetic Shielding of Conversion Space

The magnetic field in the M-M̄ conversion region was ≈ 10 G due to the fringing fields from both the C-magnet and the cyclotron. A field of this magnitude would severely suppress any

M-M̄ conversion for F = 1 state of muonium. We achieved a shielding factor of ~ 10^3 using the arrangement shown in Figure 22. The shielding consisted of three concentric Moly-Permalloy cylinders borrowed from the Chicago-UCSD group,[64] and a large 2" thick wall of iron positioned between the C-magnet and the conversion region to provide isolation. To permit the passage of decay electrons to the spark chamber, a 20" diameter hole was cut in the wall.

Further elimination of stray fields was needed along the muon beam axis. This was provided by a pair of low current correction coils mounted inside the smallest diameter cylinder. Current was adjusted to minimize the average probe reading of a 1 mG sensitive magnetometer (Hewlett Packard Model 4288E). Field mapping indicated that the residual field did not exceed 5 mG in the transverse direction and 10 mG in the longitudinal direction over the entire conversion region. The effect of this shielding upon the M-M̄ process will be described in Section IV. C.

5. Electronic Logic and Spark Chamber Optics

Figure 25 is a schematic block diagram of the electronic circuitry used in the M-M̄ conversion experiment. The relative timing of the various logic pulses is also shown in an upper insert of this figure. The main function of this circuitry was to generate a trigger pulse which would activate the spark chamber and the camera, following the identification of a muon decay electron by the spark chamber counters.

A stopping μ^+ which satisfied the fast coincidence 1 2 3 $\bar{4}$ promptly opened a 4 μsec gate. Within this time gate we looked for an electron event defined by the coincidence $\bar{1}$ 4 5 (6 or 7). Low to high momentum decay electrons were detected by counter 6. The highest momentum e^- and decay e^+ were detected by counter 7. Typical counting rates relative to the 1 2 3 $\bar{4}$ rate were as follows: ungate e^- events $\bar{1}$ 4 5 (6 or 7) = 2%; gated e^- events $\bar{1}$ 4 5 (6 or 7) = 0.025%.

The event pulses were fanned out into four branch pulses. One served as trigger pulse to the high voltage pulsing system of the spark chamber to initiate the firing of a track. The other three were fed through gate generators to control the camera trigger, the BCD light control, and the Nixie light control. The BCD lights and Nixie lights gave information about the film strip and run numbers, respectively, for later identification.

In addition to recording the track of the e^- optically, the time interval between the stopped μ^+ pulse 1 2 3 $\bar{4}$ and subsequent decay electron event $\bar{1}$ 4 5 (6 or 7) was determined by a 4 μsec range TAC and displayed in a Kicksort pulse height analyzer. If, as anticipated, most e^- events originate via electromagnetic interaction from the ordinary $\mu^+ \rightarrow e^+ + 2\nu$ decay process, then this time spectrum should exhibit the characteristic 2.2 μsec exponential shape.

The photographic system consisted of a large cylindrical lens, two mirrors and a single 35 mm camera. The cylindrical lens

was made of optical Lucite, with one flat surface 25.6" long x 14" high, and an opposite cylindrical surface with a radius of curvature of 40". The top view mirror was a front surface-coated high quality flat sheet of glass, 25" long x 8" wide. It was positioned on the top of the spark chamber where it was angled at 45° to the top surface of the chamber to provide a top view of particle tracks. Another smaller mirror was positioned in such a way as to incorporate in the frame the images of BCD and Nixie lights.

Both side view (y,z) and top view (x,y) images of charged particle tracks and fiducial points were recorded on each frame, together with a listing of frame and run numbers.

6. Data Collection

Only 24 hours of running time could be devoted to the M-$\overline{\text{M}}$ part of the experiment due to difficulties in achieving the necessary vacuum of 10^{-5} Torr in the target chamber. During this time two experiments were carried out: I) a study in which μ^+ were stopped in the target and e^- spark chamber tracks were looked for (μ^+ to e^- events run), and II) a study in which μ^+ were stopped and ordinary decay e^+ tracks were looked for (μ^+ to e^+ events run). The switch from I) to II) was accomplished simply by reversing the polarity of the spectrometer magnet. Run II served to calibrate the system. In II, about 1400 frames were taken of which 250 were observed to be $\mu^+ \to e^+$ events. We demanded that an acceptable track be longer than six gaps in order to determine its momentum.

The μ^+ stop rate was 135 sec^{-1}; the e^+ trigger rate was 28 min^{-1}. The yield of e^+ trigger per μ^+ stop, 0.34%, was consistent with the solid angle prediction.

In Run I, the search for M-$\bar{\text{M}}$, we accumulated approximately 4000 frames of which 1300 represent $\mu^+ \rightarrow e^-$ events. On the average the e^- trigger rate was 3 min^{-1}. This trigger rate seems too high compared with the probability of M-$\bar{\text{M}}$ conversion. However, as already noted, only 0.6% corresponds to μ^+ stops in the gold, which mean only 1 μ^+ per second of real stops. Most of the triggers must originate from the decay of muons which stopped in counter 3.

Because the total mass of shielding iron and other material in the path of decay positrons amounted to about 1/3 of a radiation length of iron (4.4 g/cm^2), this material caused the production of both low and high energy e^-'s through the sequence of bremsstrahlung, pair production and/or shower effects as follows:

$$\mu^+ \rightarrow e^+ + \nu + \bar{\nu}$$
$$\hookrightarrow e^+ + \gamma$$
$$\hookrightarrow e^+ + e^- . \tag{42}$$
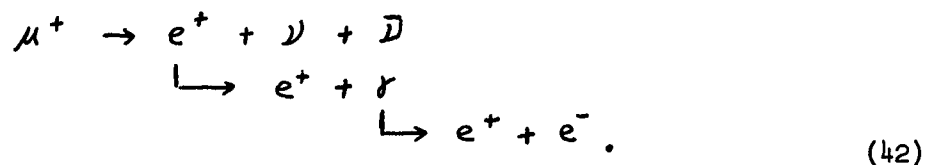
This bremsstrahlung-pair process should modify any e^- or e^+ spectrum associated with the decay process. If not present, one should obtain only the structure of Michel spectrum alone.

Muon decay time spectra were concurrently accumulated in the memory of a PHA along with the film data throughout the run.

The e⁻ events in the PHA should fit a time distribution of the form
[see equ. (23)]

$$N(t) = A e^{-t/\tau} (1 + bt^2) + B,$$

<div align="right">(43)</div>

where the first term is due to ordinary μ^+ decay, the second term
is due to the M-$\bar{\text{M}}$ conversion, and B is random background. Such a
time structure would indicate that conversion took plce.

The e⁺ event data of PHA should fit the ordinary μ^+ decay
time distribution of the form

$$N(t) = A e^{-t/\tau} + B.$$

<div align="right">(44)</div>

C. Data Reduction

1. Scanning

Film was scanned at the University of Maryland, Department
of Physics and Astronomy, using overhead projector scanning tables.
Scanning criteria were simple: 1) rejection of all tracks lacking
the necessary curvature toward counter 6, and 2) rejection of all
tracks involving fewer than six fired gaps. In general event
ambiguity was low. Figure 26 shows two typical e⁻ event frames
taken from the spark chamber system. Because the trigger is sensi-
tive to the particle charge, only a few frames reveal events of the
wrong curvature. Approximately 50% of the frames in the $\mu^+ \to e^-$

run met criteria I and II. The same held for of the $\mu^+ \rightarrow e^+$ calibration run.

2. <u>Measurement</u>

Measurements of track coordinates were made by two different methods. The first involved a template which was used to measure the polar coordinates r, θ of a track relative to fiducials marks. The second method[65] involved use of a Mangispago biradial image plane digitizer mounted on an overhead projector scanning table and linked to a PDP-8 computer. The spatial reconstruction and computer fitting results for the data from both measuring processes were quite consistent with each other.

Further elements in this system were a teletype for scanner-computer communication; a Digi-Data 1420 incremental magnetic tape recorder for data output and program storage; an online clock for program timing; and the Mangispago interface.

The tracks were measured in two stereo views. View 1 is a direct image of the y,z plane, and view 2 is a mirror image of the x,y plane, permitting each track to be reconstructed in three-dimensional space and its momentum and spatial angles to be determined. The track measurements were made relative to three fiducial marks in each view. A total of six points were measured along each view of a track in the polar coordinates r and θ. Among the six points we included the two end points of the track. If it was apparent that the particle was scattered in the spark chamber, the

track was measured up to the point where the scattering took place. If two tracks were present in the same frame each was recorded as a separate event.

3. Reconstruction

Almost without exception events were sharp and unambiguous. This made the computation simple and much easier. A computer program was used to construct histograms of the events. The first computation determined the geometrical and spatial reconstruction of the spark chamber tracks. The information input to this program from the measuring machine consisted of identification information for the event, three fiducial measurements for each view of the track and six track coordinate measurements for each view of the event. Applying rotation and translation processes we reconstructed the tracks in terms of the spark chamber coordinates x, y, z and then transformed to real coordinates by an adjustment for the magnification factor.

The next step consisted of fitting a curve to these space points by using a normal least-squares fitting procedure to determine the energy and the sign of the particle charge. This method is similar to the standard fitting technique for bubble chamber data. The real track of the event in the spark chamber is a helix. The projection of a helix onto the (x,y) plane is a circle. We first fit the circle $(x-\alpha)^2 + (y-\beta)^2 = \rho^2$ to the (x,y) coordinates of the spacial points by minimizing the function

$$F^2(\alpha, \beta, \rho^2) = \sum_{i=1}^{n} (d_i^2 - \rho^2)^2$$

<div align="right">(45)</div>

where $d_i = (x_i - \alpha)^2 + (y_i - \beta)^2$ and n is the total number of points which are measured in the track. Accordingly, the radius of curvature of the event was calculated. The corresponding error can be calculated from the equation

$$\frac{\langle \Delta \rho^2 \rangle}{\rho^2} = \frac{\sigma_d^2}{\rho^2} \left[\frac{1}{n} + \frac{\alpha^2 \Sigma y_i^2 + \beta^2 \Sigma x_i^2 - 2\alpha\beta \Sigma x_i y_i}{|\Gamma|} \right]$$

<div align="right">(46)</div>

where $|\Gamma| = \Sigma x_i^2 \, \Sigma y_i^2 - (\Sigma x_i y_i)^2$, and σ is the rms error on the coordinates. For the typical case of radius $\rho = 36.6$ cm, the error was $\frac{\Delta \rho}{\rho} = 0.02$. If computation gave $\frac{\Delta \rho}{\rho} > 0.2$ the event was rejected. The azimuthal angle ϕ, i.e., the angle which the tangent to the projection of the tracks in the (x,y) plane makes with the x-axis at the point (x,y) on the track, is given by

$$\phi = \tan^{-1} \frac{x-\alpha}{y-\beta}$$

<div align="right">(47)</div>

To find the orientation of each track, we make a linear fit to the z and θ coordinates of the spacial points. In this way the dip angle λ was obtained.

We can calculate the momentum of the track with the best-fit value of β and λ from the equation

$$\frac{1}{P_{(MeV/c)}} = \frac{\cos \lambda}{0.3 \; B_0 \, (kG) \, \rho \, (cm)}$$

(48)

The corrections for variations in the magnetic field and energy loss of the particle were taken into account in the fitted curve.

4. Selection of Events

To find the most probable interpretation of the entire event, an extrapolation of the fitted track was made for each event. All events were extrapolated back to the M-M̄ conversion region. An event was considered to be valid if it originated from within the target region. Otherwise, the event was rejected. Approximately, 25% of the measured events were excluded by this requirement. The final resultant energy spectra of valid events are recorded as histograms. Figure 27 shows the histogram of the $(\mu^+) \rightarrow (e^-)$ events. The histogram of $(\mu^+) \rightarrow (e^+)$ events is shown in Figure 28.

5. Monte Carlo Calculation

Because of the bremsstrahlung-pair production process as mentioned in Section IV. B. 6, any e^- spectrum associated with the M-M̄ process would be modified. Similarly, the production of both low and high e^+'s would distort the expected Michel spectrum of e^+'s in the "$\mu^+ \rightarrow e^+$ events" run. However, the electromagnetic inter-

action of e^+ with metal can be calculated precisely.

The Monte Carlo method was applied to the process of μ^+ decay and to that of bremsstrahlung-pair production. The initial e^+ was assumed to originate from the decay of μ^+ in the target chamber. Its energy was chosen by a random number programs RANDS and weighted by the Michel spectrum.[6]

The e^+ or γ and all degraded radiation were followed through successive layers of iron. Total material in the path of the decay positrons was divided into three intervals, each 0.1 radiation length. At each interval, the bremsstrahlung or pair production was determined by a random number technique. The efficiency of bremsstrahlung was calculated from the equation[66]

$$\epsilon_B(E) \simeq K(E)\,t$$

(49)

where t is the thickness of material in radiation lengths. K(E) is the radiation probability correction factor.

The efficiency of the pair production process was calculated from the equation[67]

$$\epsilon_p(E) = 1 - e^{-\mu(E)t}$$

(50)

where t is the thickness of material in radiation lengths and $\mu(E)$ is the total probability for pair production per radiation length.

The energy distribution of photons from bremsstrahlung or of electrons from pair production was calculated according to ref. (67), in which the correction for the screening effect of the outer electrons has been included. The electron energy loss due to collisions with matter has also been taken into account. However, the energy loss of a photon or that due to subsequent pair-annihilation was neglected.

The normalized resultant energy spectrum obtained from a 200,000 event Monte Carlo calculation is shown as hatched areas in Figure 27 and 28. As can be seen, the observed e^- or e^+ spectra can be accounted for quite readialy by the μ^+ electromagnetic process.

6. Life-Time Spectra

The time spectrum of the "$\mu^+ \to e^-$ event" run included a total of 3800 events. It was difficult to perform a least-squares fit to all parameters in eq. (43) simultaneously. Data analysis showed that it could only be fit to the pure μ^+ decay spectrum with parameter b = 0. The μ^+ mean lifetime obtained was 2.0 ± 0.2 μsec with χ^2 = 0.9 per degree of freedom. This result confirms that most of the events probably originated from μ^+ decay and subsequent electromagnetic interaction.

The data analysis of the "$\mu^+ \to e^+$ event" run yielded a muon lifetime of 2.2 μsec with χ^2 of 1.8 per degree of freedom. The χ^2 is relatively poor, but qualitatively its confirmed an ordinary μ^+ decay spectrum.

D. <u>Calculation of Upper Limit on $C_{M\bar{M}}/C_V$</u>

The results of the Monte Carlo calculation for the e^- spectrum is consistent with zero events due to M-$\bar{M}$. To set up an upper limit on the ratio $C_{M\bar{M}}/C_V$ of the coupling constant, we must choose an upper limit to the possible number of detected high energy e^- events from $\bar{M}$ decay.

The empirical formula we used in setting an upper limit on the M-$\bar{M}$ coupling constant was

$$N_{\bar{M}} = N_{\mu^+} \cdot f_M \cdot P(\bar{M}, t) \cdot \frac{d\Omega}{4\pi} \cdot \varepsilon$$

(51)

where $N_{\bar{M}}$ is the number of e^- events which are obtained from the $M \rightarrow \bar{M}$ conversion; N_{μ^+} is the number of μ^+ stops defined by 1 2 3 $\bar{4}$;

$$f_M = \frac{g/cm^2 \ of \ Au}{(g/cm^2 \ of \ Au + Counter \ 3)} \cdot \times R \ (Au)$$

(52)

is the fraction of μ^+ stops in gold resulting in slow muonium formation in vacuum, $P(\bar{M}, t)$ is the probability that a mixed M-$\bar{M}$ system will decay as a μ^- within the time interval t (Figure 3), $\frac{d\Omega}{4\pi}$ is the solid angle subtended by the spark chamber system, and ε is the spark chamber efficiency.

From the following data:

$N_{\mu^+} = 27 \times 10^6$ in the 24 hours of experimental running time

$f_M = (6 \times 10^{-3})(0.35)$

$P(\bar{M}, 4 \ \mu sec) = 8 \times 10^{-6} \ (C_{M\bar{M}}/C_V)^2$ with $t = 4 \ \mu sec$

(the width of the gate)

$$\frac{d\Omega}{4\pi} = 0.0035$$

$$\varepsilon = 1$$

if we then assume that one e^- event is due to $M \to \bar{M}$ conversion, we obtain:

$$1 = (27 \times 10^{-6}) \ (6 \times 10^{-3}) \ (0.35) \ (0.0035) \ (1) \ (8 \times 10^{-6}) \ (c_{M\bar{M}}/c_V)^2$$

This leads to

$$\frac{C_{M\bar{M}}}{C_V} \leq 25 \tag{53}$$

On the other hand, if we conservatively set an upper limit on the possible number of detected high energy e^- events by attributing all the e^- events with energy $E_{e^-} \geqslant 30$ MeV to $M\text{-}\bar{M}$ conversion, then

$$N_{\bar{M}} = 16$$

and

$$\frac{C_{M\bar{M}}}{C_V} \leq 100 \tag{54}$$

V. CONCLUSION

The observed value for the fraction of polarized muons stopping in the thin gold foils that form muonium in all possible states was 0.35 ± 0.06. This is a lower limit for muonium production in free space. An interpretation consistent with the observation would be that the muonium formed in the gold foils and diffused out into the intervening free space, with a subsequent relaxation time of ~ 200 nsec. This experiment provides the first direct information about muonium behavior in a vacuum environment. The observed conversion of M to $\bar{M}$ was consistent with zero. If one assumes that the conversion process is a four-fermion weak interaction of the universal V-A forms, the results of this experiment set an upper limit to the possible magnitude of the M-$\bar{M}$ coupling constant $C_{M\bar{M}}$ in terms of the vector coupling constant C_V of β-decay. This limit is $C_{M\bar{M}} \leq 100 \, C_V$, or $\sim 2 \times 10^{-47}$ erg-cm^3.

The search for muonium-antimuonium conversion was made for only one day at standard synchrocyclotron fluxes. It was possible to lower the upper limit on the coupling constant ratio $C_{M\bar{M}}/C_V$ from approximately 5800 to 100. It is still impossible to make a definitive statement about the nature of the leptonic number conservation law or the assumed universality of the weak interaction strength. This would require that we reduce the upper limit on the magnitude of $C_{M\bar{M}}$ to that of C_V, assuming no conversion were detected.

73

The principal limitation encountered in this M-$\bar{\text{M}}$ experiment included: (1) low muon stopping rates and the related problem of stops in "dead" layer, (2) short running period, (3) electron background caused by the electromagnetic interaction with the material of magnetic shielding, (4) small solid angle of acceptance in the spectrometer system. These problems are not difficult to overcome, particularly in view of the future availability of muon beams of higher intensity at Nevis and LAMPF.

At LAMPF, the backward μ^+ beam should provide an intensity 0.4×10^6 μ^+/sec into a 20 cm^2 spot size. If we use twenty gold foils instead of two foils, each separated at 1.5 cm intervals along the 42 MeV/c μ^+ beam, the μ^+ stopping rate in the foils will be $\sim 10^4$ μ^+/sec. This represents an improvement of $\sim 10^5$ over the conditions in this experiment.

The background events caused by the e^+ electromagnetic interaction can be eliminated by removing the magnetic shielding and all unnecessary material in the path of the electrons traveling from target region to the spectrometer. The lack of a zero $|\vec{H}|$ environment will result in a M-$\bar{\text{M}}$ conversion consideration of only $F = 0$ muonium. This would reduce the number of M states which can be considered for conversion by a factor of 4. The solid angle of acceptance of a wire chamber and spectrometer can be significantly increased by using a large H-magnet. For a spectrometer defining only 1% solid angle at the target and for a running time of 400 hrs we can anticipate ~ 400 $(C_{M\bar{M}}/C_V)^2$ events originating from the M-$\bar{\text{M}}$ conversion, assuming it exists at conventional weak interaction strength.

The total improvement would correspond to a sensitivity increase in the detection of the M-$\bar{\text{M}}$ type process of $\sim 10^8$ over this experiment. It could reduce the upper limit on the coupling constant $C_{M\bar{M}}$ to a range lower than C_V and it should then be possible to test quantitatively the forbiddeness of the process.

VI. LIST OF TABLES

Table 1a

Particle	L_e	L_μ
e^- (e^+)	+1 (-1)	0
ν_e $(\bar{\nu}_e)$	+1 (-1)	0
μ^- (μ^+)	0	+1 (-1)
ν_μ $(\bar{\nu}_\mu)$	0	+1 (-1)
all others	0	0

Additive law: ΣL_e, ΣL_μ separately conserved.

Multiplicative law: $\Sigma(L_e + L_\mu)$, $(-1)^{\Sigma L_\mu}$,

$(-1)^{\Sigma L_e}$ conserved.

Table 1b

Particle	Lepton Number L	Muon Parity P_μ
e^- (e^+)	+1 (-1)	+1 (+1)
ν_e $(\bar{\nu}_e)$	+1 (-1)	+1 (+1)
μ^- (μ^+)	+1 (-1)	-1 (-1)
ν_μ $(\bar{\nu}_\mu)$	+1 (-1)	-1 (-1)
all others	0	+1

Multiplicative law: $\Sigma L, \Pi P_\mu$ conserved.

Table 1c

Particle	Lepton Number L	Helicity
e^- (e^+)	+1 (-1)	
ν_e ($\bar{\nu}_e$)	+1 (-1)	-1 (+1)
μ^- (μ^+)	-1 (+1)	
ν_μ ($\bar{\nu}_\mu$)	-1 (+1)	-1 (+1)
all others	0	

Additive law: ΣL conserved.

Table 1d

Particle	Lepton Number L
e^- (e^+)	+1 (-1)
ν_e ($\bar{\nu}_e$)	+1 (-1)
μ^- (μ^+)	+2 (-2)
ν_μ ($\bar{\nu}_\mu$)	+2 (-2)
all others	0

Additive law: ΣL conserved.

TABLE 2

Run No.	Target	Pressure (Torr)	H (G)	Total Events (x10³)	N_0	R	T (μsec)	f (MHz/sec)	ϕ_ℓ	B (per bin)	χ^2/ν
1	1/8" Quartz	10^{-5}	− 4.0	1044	5242[a] ±8	0.66 ±0.04	2.9 ±0.5	5.49 ±0.02	1.82 ±0.07	360[a]	1.17
2	1/8" Quartz	10^{-5}	− 9.3	536	1446[b] ±3	0.65 ±0.04	1.4 ±0.3	12.99 ±0.02	2.47 ±0.10	80[b]	0.97
3	1/32" Quartz	10^{-5}	+10.0	1265	1953[c] ±7	0.45 ±0.06	2.9	−14.13	1.82[e]	127[c]	0.91
4	Argon	2280	− 3.0	154	844[d] ±2	0.85 ±0.09	2.8 ±0.8	4.19 ±0.02	1.22 ±0.12	32[d]	1.05
5	Argon	1290	− 3.0	154	789[d] ±3	0.64 ±0.16	0.7 ±0.3	4.12 ±0.07	1.36 ±0.15	57[d]	1.18
6	Argon + 200 Au foil	2280	− 3.0	155	822[d] ±2	0.98 ±0.12	1.2 ±0.3	4.15 ±0.03	1.39 ±0.18	45[d]	1.04
7	Argon + 200 Au foil	1290	− 3.0	159	837[d] ±3	0.85 ±0.15	0.3 ±0.1	4.31 ±0.11	1.50 ±0.13	49[d]	1.05

a. 10 channels per bin
b. 5 channels per bin
c. 3 channels per bin
d. 1 channel per bin
e. ϕ_ℓ fixed as given in run 1.

TABLE 3

Run No.	Target	H (G)	Total Events (x10³)	R	a_μ	B (per bin)	χ^2/ν
A	200 Au foils	+8.4	1760	0.24 ± 0.09[c]	0.117 ± 0.006	162[a]	2.01
B	200 Au foils	-10.5	715	0.32 ± 0.15	0.119 ± 0.006	50[a]	1.98
C	200 Au foils	-9.3	790	0.45 ± 0.10	0.117 ± 0.005	75[a]	0.83
D	200 Au foils	-7.0	288	0.41 ± 0.12	-	150[b]	1.01
E	200 Au foils	-5.0	1639	-0.06 ± 0.10	0.113 ± 0.008	151[a]	2.03
F	800 Au foils	-5.0	2351	-0.01 ± 0.06	0.133 ± 0.006	198[a]	1.86
G	800 Au foils	+21.0	1083	-0.04 ± 0.13	0.145 ± 0.003	76[a]	1.98
H	Frame only	-3.0	250	0.07 ± 0.12	-	114[b]	0.96
I	Frame only	-9.0	952	0.10 ± 0.12	0.114 ± 0.007	95[b]	1.63

a. 2 channels per bin.   b. 1 channel per bin.

c. Weighted average $R_{200\ Au} = 0.35 \pm 0.06$.

VII. APPENDICES

A. Different Schemes for the Lepton Number Assignment

1. Conventional Scheme:

Two different leptonic charges are assumed to exist, one for the muon and one for the electron. The scheme follows the two-component neutrino theory. We have two distinct neutrinos ν_e and ν_μ. To every particle whether lepton or nonlepton, we assign two numbers L_e and L_μ as shown in Table 1(a).

There are two ways in which to state the conservation law of leptons according to this scheme. One of them, the more restrictive of the two, is an additive law which states that in all reactions the algebraic sum of L_e and L_μ are separately conserved.

The second possibility, basically less restrictive, is a multiplicative law which states that only the sum $\Sigma(L_e + L_\mu)$ and the sign $(-1)^{\Sigma L_\mu}$ [Consequently, also the sign $(-1)^{\Sigma L_e}$] are conserved in all reactions.

2. Muon-parity Scheme:

This scheme was first introduced by Feinberg and Weinberg[8,16] in 1961. A permutation symmetry principle in weak interactions leads directly to a parity-like muonic conservation law. In this scheme there is only one additive leptonic number and one multi-

plicative "muon-parity" to be assigned to the particles as
given in Table 1(b).

In this scheme, multiplicative in nature, we are involved
with the "normal" conservation of lepton number L, that is the
algebraic sum of lepton number L should be conserved in all
interactions. In addition, we require the muon parity of a
system of particles, which is the product of the values for
the individual particles, to be universally conserved; i.e.,

$$\prod_i P(i) = constant.$$

This scheme is equivalent to the second possibility of
the conventional scheme.

3. Konopinski and Mahmoud Scheme:

This scheme was proposed earlier by Konopinski and
Mahmoud[68] in 1953 and is also consistent with present experi-
mental evidence. Only one additive leptonic number is
assigned to leptons. No additional muon number is required.
We select e^-, ν_e, μ^+, $\bar{\nu}_\mu$ as particles and assign a lepton
number L = +1 while e^+, $\bar{\nu}_e$, μ^-, ν_μ are taken to be anti-
particles for which L = -1 (see Table 1(c)). The signs of
the μ^- and e^- quantum numbers are opposite. The electron
neutrino ν_e and muon antineutrino $\bar{\nu}_\mu$ are considered to be
negative (left-handed) and positive (right-handed) helicity
particles, respectively. We have, therefore, two distinct
neutrinos in one four-component neutrino theory.

The conservation law shall be only additive in this scheme; namely, the algebraic sum ΣL must be universally conserved in all interactions. The helicity assignment will prohibit the same reactions prohibited by the muon number in the conventional scheme.

4. Double number Scheme[7,69]

There exists one additive lepton number, but with different magnitudes for the electron-like and muon-like particles. The lepton number assignment is shown in Table 1(d).

The conservation of lepton number requires that the algebraic sum of L must be conserved in all reactions. This version is indistinguishable from the additive law in scheme 1 if there are only two leptons.

Within the framework of the above four different schemes there is no experimental evidence presently available which would permit us to decide which one is generally favored in weak interactions. The additive law is pleasing because of its similarity to baryon and charge conservation. Furthermore it does not tamper with weak interaction universality. From a theoretical point of view, the multiplicative law is somewhat more attractive because it is associated with a world of exactly two lepton families, muons and electrons. A multiplicative (parity-like) world would allow us to understand better why the muon exists and why it seems to be the only heavy electron.[8]

B. Energy Eigenstates and Energy Levels for the M-$\bar{\text{M}}$ Coupled System.

The Hamiltonian for the ground state of the M-$\bar{\text{M}}$ system in an external magnetic field is

$$H = H_{em} + H_W$$

(B-1)

where H_w is the weak interaction which couples muonium and anti-muonium states and is responsible for the conversion process M→$\bar{\text{M}}$, H_{em} is the unperturbed Hamiltonian which includes the spin-spin interaction and Zeeman terms. The detailed form is

$$H_{em} = A\, \vec{S}_\mu \cdot \vec{S}_e + g_e\, \mu_B^e\, \vec{S}_e \cdot \vec{H} + g_\mu\, \mu_B^\mu\, \vec{S}_\mu \cdot \vec{H} \; ,$$

(B-2)

in which A is the zero-field hyperfine energy splitting and has a value[38] of 1.84×10^{-5} eV (4.463×10^3 MHz); $\vec{S}_\mu$ and $\vec{S}_e$ are the muon and electron spin operators, respectively; g_e is the electron gyromagnetic ratio in muonium (antimuonium), $g_{e-} = -g_e + \simeq 2$; g_μ is the muon gyromagnetic ratio in muonium (antimuonium), $g_\mu^+ = -g_{\mu-} \simeq -2$; $\vec{H}$ is the static, external magnetic field; μ_B^e and μ_B^μ are Bohr magnetons for electron and muon (considered positive numbers),

$$\mu_B^e = \frac{|e|}{2 m_e} \; , \quad \text{and} \quad \mu_B^\mu = \frac{|e|}{2 m_\mu} \quad (\hbar = c = 1) \; .$$

(B-3)

The unperturbed eigenfunctions and energies are obtained by solving the Schrodinger equation

$$H_{em}\, \Psi_o = E_o\, \Psi_o$$

(B-4)

This equation splits into two equations, one for muonium and one for antimuonium. The solutions for the hyperfine state energy levels of muonium and antimuonium based on this equation are given by the well-known Breit-Rabi formula.[17]

$$E_{F=\frac{1}{2}\pm\frac{1}{2}, m_F} = -\frac{A}{4} + \mu_B^\mu g_\mu H m_F \pm \frac{A}{2}(1 + 2m_F x + x^2)^{\frac{1}{2}},$$

(B-5)

in which F is the total angular momentum quantum number, m_F is the associated magnetic quantum number. The quantity x is:

$$X \equiv \frac{(\mu_B^e g_e - \mu_B^\mu g_\mu)|\vec{H}|}{A} \simeq \frac{|\vec{H}|}{1585\,G}.$$

(B-6)

The normalized spin eigenfunctions denoted by $|M_i\rangle$ for muonium and $|\bar{M}_i\rangle$ for antimuonium are

$$|M_1\rangle = \alpha_{e^-}\alpha_{\mu^+} \qquad ; \qquad |\bar{M}_1\rangle = \alpha_{e^+}\alpha_{\mu^-}$$

$$|M_2\rangle = C\alpha_{e^-}\beta_{\mu^+} + S\beta_{e^-}\alpha_{\mu^+} \quad ; \quad |\bar{M}_2\rangle = S\alpha_{e^+}\beta_{\mu^-} + C\beta_{e^+}\alpha_{\mu^-}$$

$$|M_3\rangle = \beta_{e^-}\beta_{\mu^+} \qquad ; \qquad |\bar{M}_3\rangle = \beta_{e^+}\beta_{\mu^-}$$

$$|M_4\rangle = -S\alpha_{e^-}\beta_{\mu^+} + C\beta_{e^-}\alpha_{\mu^+} \quad ; \quad |\bar{M}_4\rangle = -C\alpha_{e^+}\beta_{\mu^-} + S\beta_{e^+}\alpha_{\mu^-}$$

(B-7)

in which the hyperfine structure (hfs) states $(F, m_F) = (1,+1)$, $(1,0)$, $(1,-1)$, and $(0,0)$ are represented by the subscript number 1, 2, 3, and 4, respectively.

The α's and β's are normalized spin eigenfunctions for the indicated particles with spin direction parallel and antiparallel, respectively, to the direction of the magnetic field. The magnetic field-dependent coefficients c and s are given by:

$$c = \frac{1}{\sqrt{2}} \left(1 - \frac{x}{\sqrt{1+x^2}} \right)^{1/2} \quad \text{and} \quad s = \frac{1}{\sqrt{2}} \left(1 + \frac{x}{\sqrt{1+x^2}} \right)^{1/2},$$

(B-8)

with $c^2 + s^2 = 1$.

Because the g factors have opposite sign for particle and anti-particle, the hfs energy levels in the muonium states with $m_F = 0$ ($|M_2\rangle$ and $|M_4\rangle$) have the same energies as their corresponding anti-muonium states ($|\bar{M}_2\rangle$ and $|\bar{M}_4\rangle$), whereas the corresponding $m_F = +1$ and $m_F = -1$ states are inverted (e.g., $E_1 = \bar{E}_3$, and $E_3 = \bar{E}_1$). It is therefore to be expected that the magnetic field dependence of M-$\bar{\text{M}}$ transition probability will be different for $m_F = \pm 1$ and $m_F = 0$ states. The explicit values of hfs energy levels are[70]

$$E_1 = \bar{E}_3 = \frac{A}{4} + \mu H$$

$$E_2 = \bar{E}_2 = \frac{A}{4} \left(-1 + 2\sqrt{1+x^2} \right)$$

$$E_3 = \bar{E}_1 = \frac{A}{4} - \mu H$$

$$E_4 = \bar{E}_4 = \frac{A}{4} \left(-1 - 2\sqrt{1+x^2} \right),$$

(B-9)

with $\mu = \frac{1}{2}(g_e\mu_B^e + g_\mu\mu_B^\mu)$. Thus, the muonium and antimuonium hfs energy states form a two fold degenerate system as plotted against magnetic field in Figure 2 (dashed lines).

Next, we introduce the weak interaction Hamiltonian H_w, which will break the M-$\bar{\text{M}}$ degeneracy. This treatment follows that given by Feinberg and Weinberg.[16] A possible interaction with this effect is

$$H_W = \frac{C_{M\bar{M}}}{\sqrt{2}} \, \bar{\psi}_\mu \gamma_\lambda \, (1+\gamma_5) \psi_e \, \bar{\psi}_\mu \gamma^\lambda (1+\gamma_5) \psi_e + h.c.$$

(B-10)

which is a four-fermion weak interaction of the universal V-A form. This Hamiltonian will couple a particular M eigenstate to the corresponding $\bar{\text{M}}$ eigenstate with the same spin angular momentum quantum numbers, since angular momentum must be conserved in the M-$\bar{\text{M}}$ conversion process. For such a pair of states the matrix element for conversion of M into $\bar{\text{M}}$ is

$$\langle \bar{M}_i | H_W | M_i \rangle = \langle M_i | H_W | \bar{M}_i \rangle = \begin{cases} \dfrac{\delta}{2} & \text{for } i = 1, 3 \\ \dfrac{\delta}{2}(1+\chi^2)^{-1/2} & \text{for } i = 2, 4 \end{cases}$$

(B-11)

where

$$\delta = \frac{C_{M\bar{M}}}{\sqrt{2}} \left(\frac{16}{\pi a_\circ^3}\right) = 2.1 \times 10^{-12} \left(\frac{C_{M\bar{M}}}{C_V}\right) eV,$$

(B-12)

and a_o is the Bohr radius $(m_e e^2)^{-1}$.

First we consider the case of muonium (antimuonium) in the $F=1$, $m_F = +1$ state, in the presence of static external fields which break the original M-$\bar{\text{M}}$ degeneracy by an amount $\Delta = 2\mu|\vec{H}|$. The actual eigenfunctions and energies of the M-$\bar{\text{M}}$ system in the presence of H_w can be obtained by using a perturbation method, in which the M-$\bar{\text{M}}$ mixed states are linear superpositions of the unperturbed eigenfunctions (B-7). In order to obtain the two energies we have to solve the secular equation,

$$\begin{vmatrix} \langle M_1 | H | M_1 \rangle - E & \langle M_1 | H | \bar{M}_1 \rangle \\ \\ \langle \bar{M}_1 | H | M_1 \rangle & \langle \bar{M}_1 | H | \bar{M}_1 \rangle - E \end{vmatrix} = 0$$

(B-13)

But

$$\langle M_i | H_w | M_i \rangle = \langle \bar{M}_i | H_w | \bar{M}_i \rangle = 0 \quad , \quad \text{and}$$

$$\langle M_i | H_{em} | \bar{M}_i \rangle = \langle \bar{M}_i | H_{em} | M_i \rangle = 0 \quad .$$

(B-14)

From eqs. (B-9), (B-11) and (B-14), eg. (13) can be written

$$\begin{vmatrix} \dfrac{A}{4} + \mu|\vec{H}| - E & \dfrac{\delta}{2} \\ \\ \dfrac{\delta}{2} & \dfrac{A}{4} - \mu|\vec{H}| - E \end{vmatrix} = 0$$

(B-15)

Solving eq. (B-15) for E we get

$$E_{1\pm} = \frac{A}{4} \pm \sqrt{(\mu|\overline{H}|)^2 + (\tfrac{\delta}{2})^2} = \frac{A}{4} \pm \frac{1}{2}(\Delta^2 + \delta^2) = \frac{A}{4} \pm \frac{W}{2}$$

(B-16)

with

$$W = E_{1+} - E_{1-} = (\Delta^2 + \delta^2)^{1/2}$$

The two corresponding energy eigenstates are

$$|M_{1+}\rangle = [2W(W-\Delta)]^{-1/2}(\delta|M_1\rangle + (W-\Delta)|\overline{M}_1\rangle)$$

$$|M_{1-}\rangle = [2W(W+\Delta)]^{-1/2}(-\delta|M_1\rangle + (W+\Delta)|\overline{M}_1\rangle)$$

(B-17)

where the + notation and − notation refer to state that for $\Delta = 0$
resolve into symmetric and antisymmetric combinations of $|M_i\rangle$ and
$|\overline{M}_i\rangle$, respectively.

Because the unperturbed energy levels of the states $m_F = +1$ and
$m_F = -1$ states in muonium and antimuonium are inverted, the two new
energies $(E_3\pm)$ for the $m_F = -1$ states are equal to two new energies
$(E_1\pm)$ of the $m_F = +1$ states, i.e.,

$$E_{3\pm} = E_{1\pm} = \frac{A}{4} \pm \frac{W}{2}$$

.

(B-18)

The two eigenstates corresponding to E_{3-} and E_{3+} must have a structure similar to the new eigenstates of $m_F = +1$ in eq. (B-17):

$$|M_{3+}\rangle = \left[2W(W-\Delta)\right]^{-1/2} \left(\delta |M_3\rangle + (W-\Delta)|\overline{M}_3\rangle \right)$$

$$|M_{3-}\rangle = \left[2W(W+\Delta)\right]^{-1/2} \left(-\delta |M_3\rangle + (W+\Delta)|\overline{M}_3\rangle \right).$$

(B-19)

The secular equation for the F=1, $m_F = 0$ degenerate states is

$$\begin{vmatrix} E_2 - E & \frac{\delta}{2}(1+X^2)^{-1/2} \\ \frac{\delta}{2}(1+X^2)^{-1/2} & E_2 - E \end{vmatrix} = 0 \quad ,$$

(B-20)

since $\overline{E}_2 = E_2$. The two solutions for eq. (B-20) are

$$E_{2\pm} = E_2 \pm \frac{\delta}{2}(1+X^2)^{-1/2}$$

(B-21)

The corresponding energy eigenstates are

$$|M_{2\pm}\rangle = \frac{1}{\sqrt{2}} \left(|M_2\rangle \pm |\overline{M}_2\rangle \right).$$

(B-22)

Similarly we can obtain the actual energies and eigenstates for the F=0, $m_F = 0$ degenerate state. They are

$$E_{4\pm} = E_4 \pm \frac{\delta}{2}(1+X^2)^{-1/2},$$

(B-23)

and

$$|M_{4\pm}\rangle = \frac{1}{\sqrt{2}} \left(|M_4\rangle \pm |\bar{M}_4\rangle \right)$$

(B-24)

These modified hfs energy levels are plotted as solid lines in Figure 2.

C. Non-Linear Least-Squares Fit:

A measure of goodness of fit χ^2 for n observations y_i is defines by

$$\chi^2 \equiv \sum_{i=1}^{n} \left\{ \frac{1}{\sigma_i^2} [y_i - f(x_i, a_j)]^2 \right\} \qquad n > j$$

where

(C-1)

y_i are the data points,

σ_i are the statistical errors in the data points. We chose $\sigma_i^2 = y_i$ based upon the assumption in which the observations are known to be distributed according to the Poisson distribution,

a_j are the parameters to be determined, and

$f(x_i, a_j)$ is the fitting form used to give the functional behavior at the observation point x_i. Thus eq.(41) is written as

$$f(x_i, a_j) = a_1 e^{-x_i/\hbar} [1 + \alpha a_2 e^{-x_i/a_3} \cos(a_4 x_i + a_5)$$
$$+ a_6 \cos(b a_4 x_i + a_5)] + a_7$$

(C-2)

The values of parameters a_j are obtained by minimizing χ^2 with respect to each parameter simultaneously, i.e. we have to solve j simultaneous equations

$$\frac{\partial}{\partial a_j} \chi^2 = \frac{\partial}{\partial a_j} \sum_{i=1}^{n} \left\{ \frac{1}{\sigma_i^2} [y_i - f(x_i, a_j)]^2 \right\} = 0$$

(C-3)

In order to solve these non-linear equations, the method we used is to expand the fitting function $f(x_i, a_j)$ to first order in a Taylor's series expansion as a function of the parameters a_j about the point which is given by initial estimates.

$$f(x_i, a_j) = f_o(x_i, a_{jo}) + \sum_j \left[\frac{\partial f_o(x_i, a_{jo})}{\partial a_j} \delta a_j \right]$$

(C-4)

The result is a function which is linear in the parameter increments δa_j, to which we apply the method of linear least-squares.

To this approximation, the explicit form of χ^2 is

$$\chi^2 = \sum_i \left\{ \frac{1}{\sigma_i^2} \left[y_i - f_o(x_i, a_{jo}) - \sum_j \left(\frac{\partial f_o}{\partial a_j} \delta a_j \right) \right]^2 \right\}$$

(C-5)

We now minimize χ^2 with respect to each of the parameter increments δa_j, by setting the derivatives equal to 0.

$$\frac{\partial \chi^2}{\partial \delta a_K} = -2 \sum_i \left\{ \frac{1}{\sigma_i^2} \left[y_i - f_o(x_i, a_{jo}) - \sum_j \left(\frac{\partial f_o}{\partial a_j} \delta a_j \right) \right] \frac{\partial f_o}{\partial a_K} \right\} = 0$$

(C-6)

Transposing and setting $\Delta y_i = y_i - f_o(x_i, a_{jo})$, we have

$$\sum_i \left\{ \frac{1}{\sigma_i^2} \sum_j \left(\frac{\partial f_o}{\partial a_j} \delta a_j \right) \right\} \frac{\partial f_o}{\partial a_K} = \sum_i \frac{1}{\sigma_i^2} \Delta y_i \frac{\partial f_o}{\partial a_K}$$

(C-7a)

In the matrix form

$$\underline{A} \, \underline{\alpha} = \underline{\beta}$$

(C-7b)

where

$$\beta_k = \sum_i \frac{1}{\sigma_i^2} \Delta y_i \frac{\partial f_o}{\partial q_k}$$

$$\alpha_{jk} = \alpha_{kj} = \sum_i \frac{1}{\sigma_i^2} \left(\frac{\partial f_o}{\partial q_j} \right) \left(\frac{\partial f_o}{\partial q_k} \right)$$

$$A_j = \delta a_j \tag{C-8}$$

The solution is

$$\underline{A} = \underline{\beta} \, \underline{\alpha}^{-1} \tag{C-9}$$

The solution to the equation (C-7) is a set of values δa_j, with which to modify each of the a_{jo}. We do this by applying

$$a_j = a_{jo} + \delta a_j \tag{C-10}$$

The improved estimates of the a_j are then placed into eqs. (C-7) and (C-10), and the process is repeated until the δa_j are all deemed "sufficiently small". When this occurs, we say that the process has converged and we take these a_j as the desired values of the least squares calculation.

The error matrix is

$$\underline{\epsilon} = \underline{\alpha}^{-1} \tag{C-11}$$

The uncertainty in each parameter is

$$\sigma_{a_j}^2 = \epsilon_{jj}$$

<div align="right">(C-12)</div>

where ϵ_{jj} are the diagonal matrix element in the error matrix $\underline{\epsilon}$.

The uncertainty calculated in this experiment was followed by the equation

$$\sigma_{a_j}^2 = \frac{\chi^2}{N-P} \epsilon_{jj}$$

<div align="right">(C-13)</div>

Where N is the number of data points, and

P is the number of free parameters.

This will increase the uncertainty in each parameter if $\frac{\chi^2}{N-p} > 1$.

Since the predicted value of χ^2 is the number of data points N minus

1 for each parameter determined from the data we should find that

$$\frac{\chi^2}{N-P} \simeq 1$$

<div align="right">(C-14)</div>

VIII. LIST OF REFERENCES

1. Martin L. Perl, "The search for muon-electron differences". SLAC-
    Pub-982, November 1971.

2. G. Danby, J. M. Gaillard, K. Goulianos, L. M. Lederman, N. Mistry,
    M. Schwartz, and J. Steinberger, Phys. Rev. Lett. $\underline{9}$, 36, (1962).

3. Number taken from T. A. Lasinski et al., Rev. Mod. Phys., $\underline{45}$, S15
    (1973).

4. D. A. Bryman, M. Blecher, K. Gotow and R. J. Powers, Phys. Rev.
    Lett., $\underline{28}$, 1469 (1972).

5. R. E. Marshak, Riazuddin, and C. P. Ryan, Theory of Weak Interaction
    in Particle Physics, Wiley, 1969.

6. T. D. Lee and C. S. Wu, Ann. Rev. of Nuclear Science, $\underline{15}$, 381 (1965).

7. Pontecorvo, Zh. Eksp. Teor. Fiz. $\underline{53}$, 1717 (1967), [Sov. Phys. JETP
    $\underline{26}$, 984 (1968)].

8. G. Feinberg and S. Weinberg, Phys. Rev. Lett. $\underline{6}$, 381 (1961).

9. B. Pontecorvo, Zh. Eksp. Teor. Fiz. $\underline{33}$, 549 (1957), [Sov. Phys. JETP
    $\underline{6}$, 429 (1958)].

10. J. J. Amato, P. Crane, V. W. Hughes, J. E. Rothberg, P. A. Thompson,
    Phys. Rev. Lett. $\underline{21}$, 1709 (1968).

11. W. C. Barber, D. C. Cheng, B. Gittelman, G. K. O'Neill, Phys. Rev.
    Lett. $\underline{22}$, 902 (1969).

12. C. Y. Chang, Phys. Rev. Lett. $\underline{24}$, 79 (1970).

13. K. Borer, et al., Phys. Lett. $\underline{29B}$, 614 (1969).

14. CERN Gargamelle group, T. Eichten et al., Phys. Lett. $\underline{46B}$, 281 (1973).

15. K. Lande et al., LA-4842-MS, LAMPF Neutrino Facility Proposal.

16. G. Feinberg and S. Weinberg, Phys. Rev. 123, 1439 (1961).

17. V. W. Hughes, Ann. Rev. of Nuclear Science, 16, 445 (1966).

18. G. G. Myasishcheva, Yu. V. Obukhov, V. S. Roganov, and V. G. Firsov, Zh. Eksp. Teor. Fiz. 53, 451 (1967), [Sov. Phys. JETP 26, 298 (1968)].

19. G. Feher, R. Prepost and A. M. Sachs, Phys. Rev. Lett. 5, 515 (1960).

20. V. G. Nosov and I. Y. Yakovlev, Zh. Eksp. Teor. Fiz. 43, 1750 (1962), [Sov. Phys. JETP 16, 1236 (1963)].

21. V. G. Firsov and V. M. Byakov, Zh. Eksp. Teor. Fiz. 47, 1074 (1964), [Sov. Phys. JETP 20, 719 (1965)].
    V. G. Firsov, Zh. Eksp. Teor. Fiz. 48, 1179 (1965), [Sov. Phys. JETP 21, 786 (1965)].

22. V. W. Hughes, D. W. McColm, K. Ziock, and R. Prepost, Phys. Rev. Lett. 5, 63 (1960).

23. C. Y. Chang, G. B. Yodh, J. B. Carroll, M. Eckhause, C. S. Hsieh, J. R. Kane, R. T. Siegel and C. B. Spence, Bull. Am. Phys. Soc. 16, 617 (1971).

24. C. S. Hsieh, J. B. Carroll, M. Eckhause, J. R. Kane, C. B. Spence, R. T. Siegel, C. Y. Chang and G. B. Yodh, Bull. Am. Phys. Soc. 17, 453 (1972).

25. J. A. Phillips, Phys. Rev. 97, 404 (1955).

26. S. K. Allison, Rev. of Modern Phys. 30, 1137 (1958).

27. D. L. Wessel, Charge Transfer Ratios for Hydrogen ions in Gold Foil. Internal Reports, College of William and Mary, 1972.

28. D. W. Koopman, Phys. Rev. 154, 79 (1967).

29. M. Lepeles, R. Novick and N. Tolk, Phys. Rev. Lett. $\underline{15}$, 815 (1965).

30. M. Kaminsky, <u>Atomic and Ionic Impact Phenomena on Metal Surfaces</u>, Chap. 12, Academic Press, 1965.

31. D. G. Costello, D. E. Groce, D. F. Herring and J. Wm. McGowan, Phys. Rev. $\underline{B5}$, 1433 (1972).

32. B. Y. Tong, Phys. Rev. $\underline{B5}$, 1436 (1972).

33. C. H. Hodges and M. J. Stott, Phys. Rev. $\underline{B7}$, 73 (1973).

34. D. J. Judd, Y. K. Lee, L. Madansky, E. R. Carlson, V. W. Hughes and B. Zundell, Phys. Rev. Lett., $\underline{30}$, 202 (1973).

35. C. H. Hodges, Private communication.

36. W. M. Mueller, James P. Blackledge, and George G. Libowitz, <u>Metal Hydrides</u>, Chap. 12, Academic Press, New York, 1968.

37. E. W. R. Stercie and F. M. G. Johnson, Proc. Roy. Soc. (London), Ser. A, $\underline{117}$, 662 (1928).

38. H. G. E. Kobrak, R. A. Swanson, D. Favart, W. Kells, A. Magnon, P. M. McIntyre, J. Roehrig, D. Y. Stowell, V. L. Telegdi, and M. Eckhause, Phys. Lett. $\underline{43B}$, 526 (1973).

39. J. M. Bailey, W. E. Cleland, V. W. Hughes, R. Prepost, and K. Ziock, Phys. Rev. $\underline{A3}$, 871 (1971).

40. S. L. Glashow, Phys. Rev. Lett., $\underline{6}$, 196 (1961).

41. T. D. Lee and C. N. Yang, Phys. Rev. $\underline{104}$, 254 (1956), ibid. $\underline{105}$, 1671 (1957).

42. R. L. Garwin, L. M. Lederman, and M. Weinrich, Phys. Rev. $\underline{105}$, 1415 (1957).

43. J. I. Friedman, and V. L. Telegdi, Phys. Rev. $\underline{105}$, 1681 (1957).

44. V. W. Hughes, D. W. McColm, K. Ziock and R. Prepost, Phys. Rev. A1, 595 (1970).

45. I. I. Gurevich, I. G. Ivanter, E. A. Meleshko, B. A. Nikolsky, V. S. Roganov, V. I. Selivanov, V. P. Smilga, B. V. Sokolev, and V. D. Shestakov, Phys. Letters, 29B, 387 (1969); also Zh. Eksp. Teor. Fiz. 60, 471 (1971) [Sov. Phys. JETP 33, 253 (1971)].

46. H. O. Funsten, Nucl. Instr. and Meth. 94, 443 (1971).

47. New England Nuclear Corporation, Pilot Chemicals Division, Watertown, Mass. 02172.

48. The precision magnetic shield 32P100x55N was obtained from Perfection Mica Company, Bensenville, Ill. 60106.

49. R. A. Swanson, Phys. Rev. 112, 580 (1958), also, A. Buhler, T. Massam, Th. Muller, M. Schneegans, and A. Zichichi, Nuovo Cimento 36, 824 (1965).

50. We used the ultra high purity (99.998%) Argon gas obtained from Air Products and Chemical Inc., 773 W. Broad St., Emmaus, Pa. 18049.

51. The gold foils used were commercially available gold leaf from Hastings and Co., Inc., Philadelphia 1, Pa.

52. We used the Bell 240 increamental gaussmeter and Hall probe from F. W. Bell, Inc., Columbus, Ohio 43229.

53. ORTEC 437A time to amplitude converter.

54. M. Eckhause, R. T. Siegel, and R. E. Welsh, Nucl. Instr. and Meth. 43, 365 (1966).

55. Nuclear Data 3300, Multi-parameter Pulse Height Analysis System.

56. E. G. & G. Nanonotes, Vol. 1, No. 2, Jan. 1964.

57. Fairchild crystal controlled time mark generator, type 781A.

58. R. H. Moore and R. K. Zeigler, Los Alamos Scientific Laboratory Report La-2367, 1959.

59. P. R. Bevinton, "Data Reduction and Error Analysis for the Physical Sciences". McGraw-Hill (1969).

60. G. G. Myasishcheva, Yu. V. Obukhov, V. S. Roganov, and V. G. Firsov, Sov. Phys. JETP Lett. $\underline{5}$, 182 (1967).

61. Manufactured by Science Accessories Corporation, 65 Station St. Southport, Connecticut.

62. Manufactured by Gow Mac Instrument Company, Madison, New Jersey.

63. C-Magnet from Space Radiation Effects Lab., Newport News, Virginia.

64. D. Favart, P. M. McIntyre, D. Y. Stowell, V. L. Telegdi, R. Devoe, and R. A. Swanson, Phys. Rev. $\underline{A8}$, 1195 (1973); also see W. G. Wadey, Rev. Sci. Instrum., $\underline{27}$, 910 (1956).

65. John D. Rayner, M. S. Thesis, An On-Line Measurement System for Bubble Chamber Photographs, University of Maryland, 1969.

66. H. W. Koch and J. W. Motz, Rev. Mod. Phys. $\underline{31}$, 920 (1959).

67. Bruno Rossi, High-Energy Particles, Prentice-Hall Inc., 1956.

68. E. S. Konopinski and H. M. Mahmoud, Phys. Rev. $\underline{92}$, 1045 (1953). K. Nishijima, Phys. Rev. $\underline{108}$, 907 (1957).

69. J. Schwinger, Ann. Phys. $\underline{2}$, 407 (1957).

70. Feynman, Leighton, and Sands, The Feynman Lectures on Physics, Vol. III, Chap. 12, Addison-Wesley Publishing Company, New York, 1965.

IX. ACKNOWLEDGMENTS

The author also wishes to express appreciation for financial support to the College of William and Mary, the National Science Foundation and the National Aeronautics and Space Adminstration.

The work reported here was partly supported by the National Science Foundation and the National Aeronautics and Space Administration.

X. LIST OF FIGURES

with H = -3.0 G, (c) argon at 1290 Torr with H = -3.0 G, (d) 200 gold foil in argon at 1290 Torr with H = -3.0 G. The value of R is plotted against the muonium frequency ($\omega/2\pi H$). The dots are best-fit results. Solid curves are Fourier spectra of muonium oscillation at the measured magnetic fields.

Figure 26 Two typical spark tracks for an electron event. The bent

track is a top view from the reflection of the mirror while

the straight track is a front view of event.

Figure 27 Histogram of observed e^- events (solid line) and the normal-

ized results of a Monte Carlo calculation of the bremsstrahlung-

pair process for decay positrons (hatched).

Figure 28 Histogram of observed e^+ events (solid line) and the normal-

ized results of a Monte Carlo calculation of the bremsstrahlung-

pair process for decay positrons (hatched).

Figure 1

Figure 2

$$P(M,t) = \int_0^t dt' \lambda e^{-\lambda t'} |\langle \overline{M}|\psi(t')\rangle|^2$$

$$|\langle \overline{M}|\psi(t')\rangle|^2 e^{-\lambda t'}$$

Figure 3

Bending magnet

Experimental area

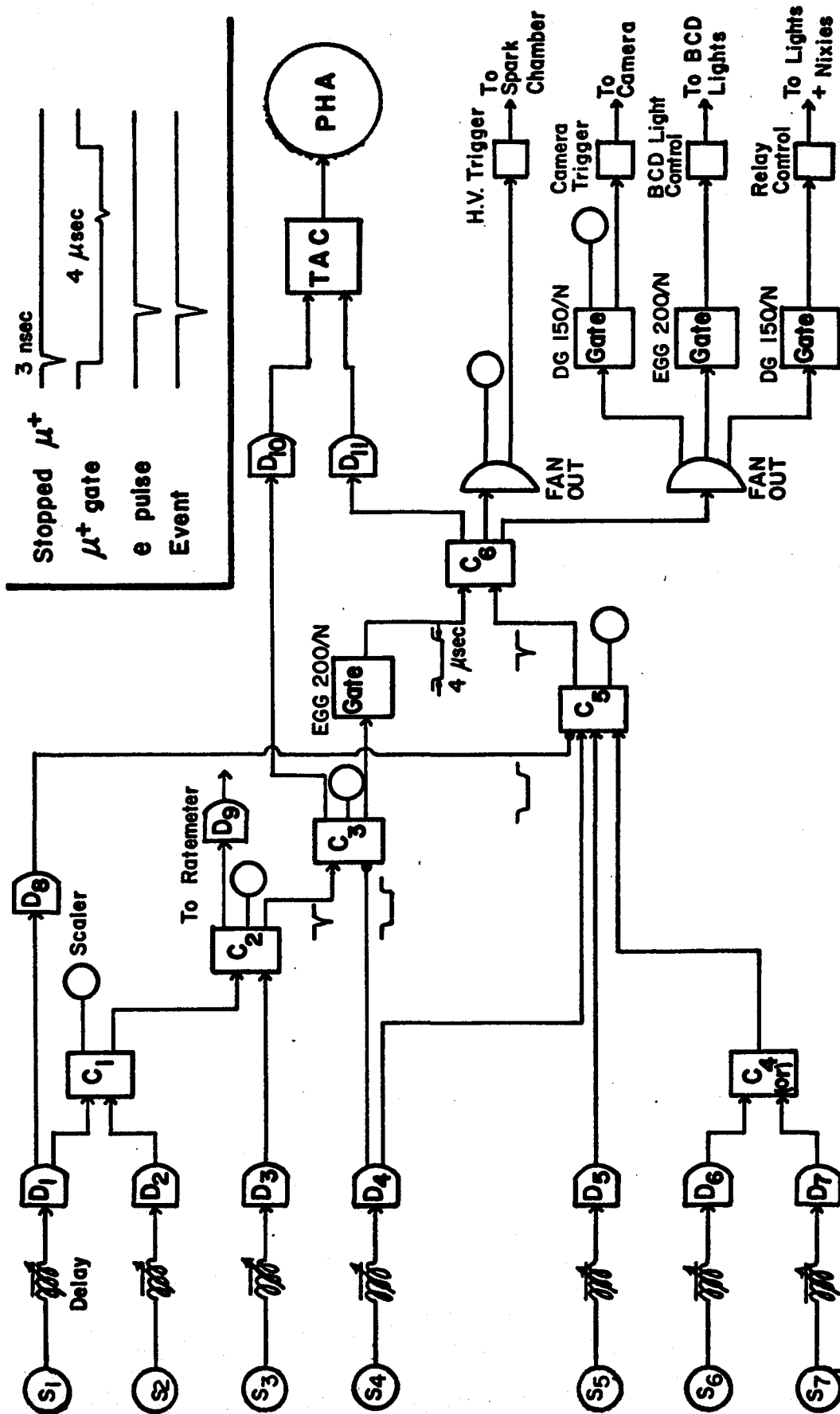Bending magnet

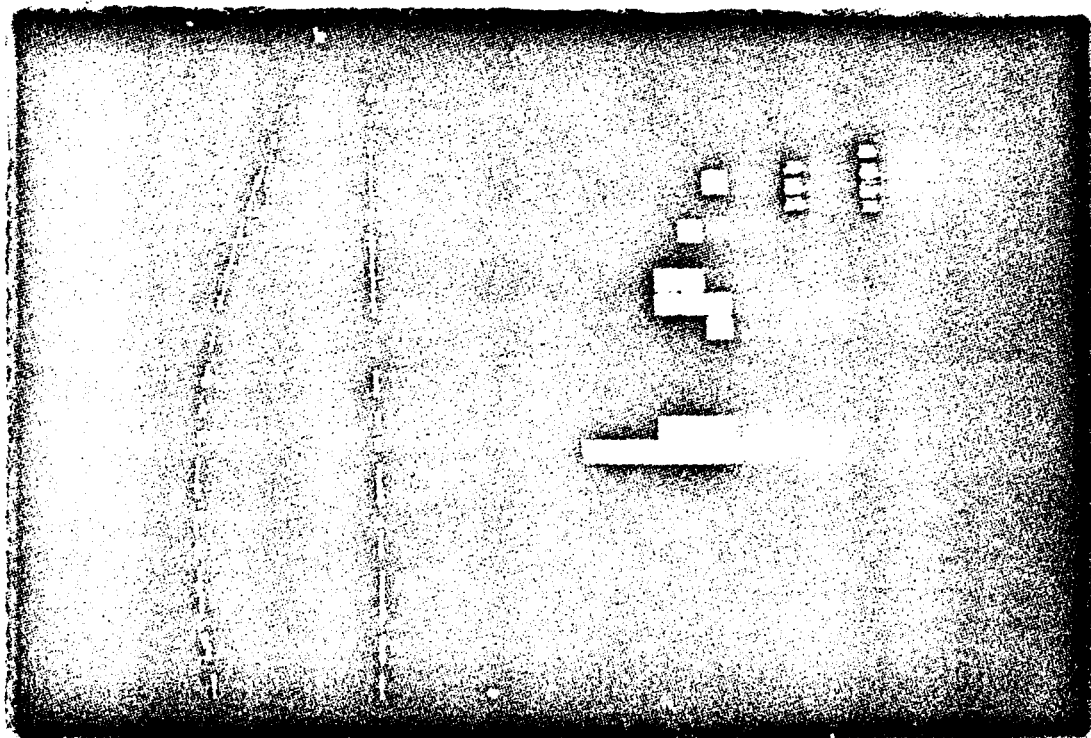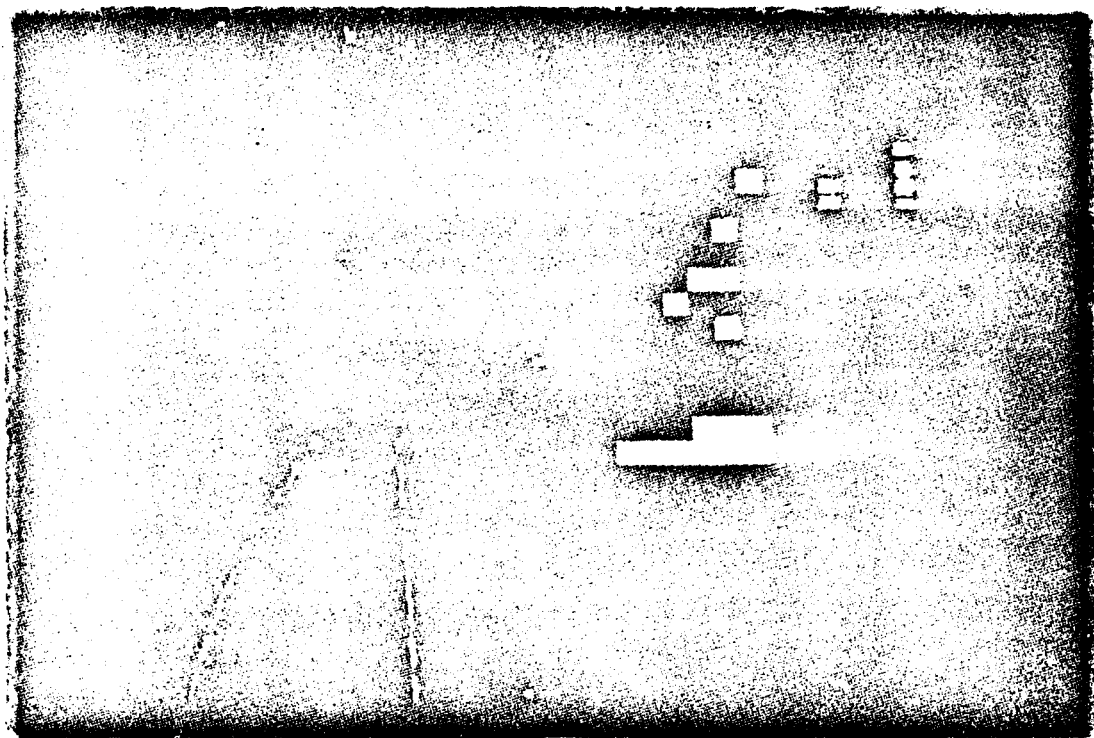Muon channel

Quad doublet

Meson window

Cyclotron yoke

Pole tip

Cyclotron

Scale 6 ft.
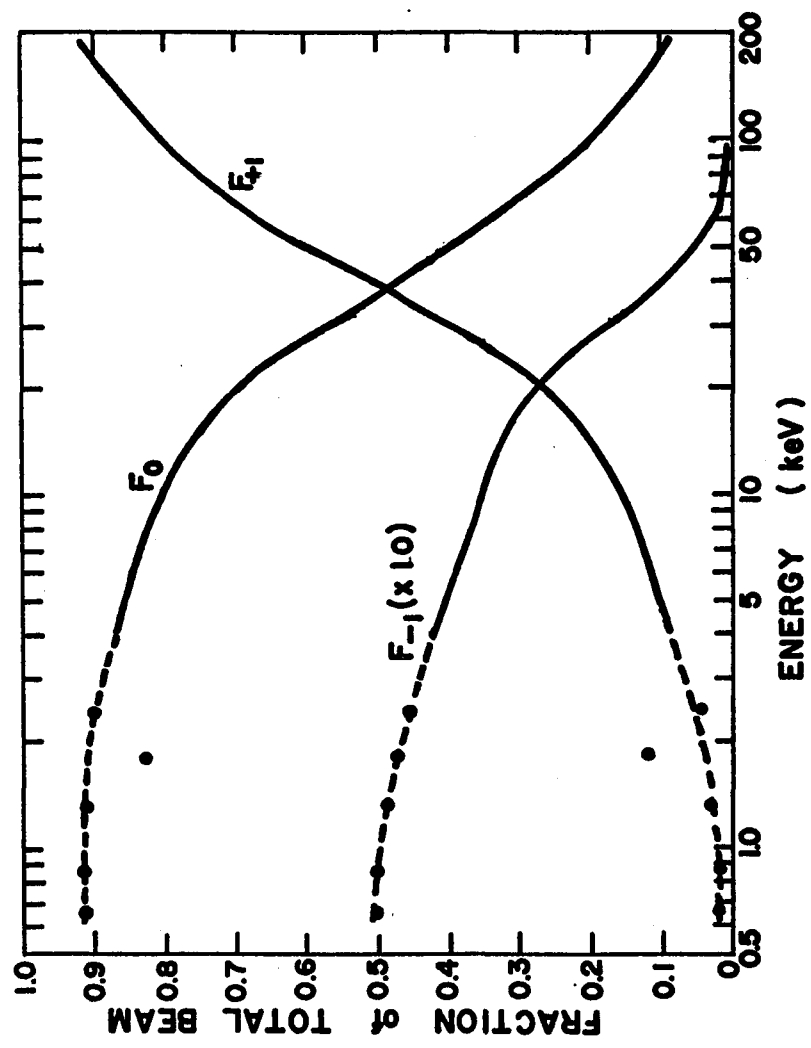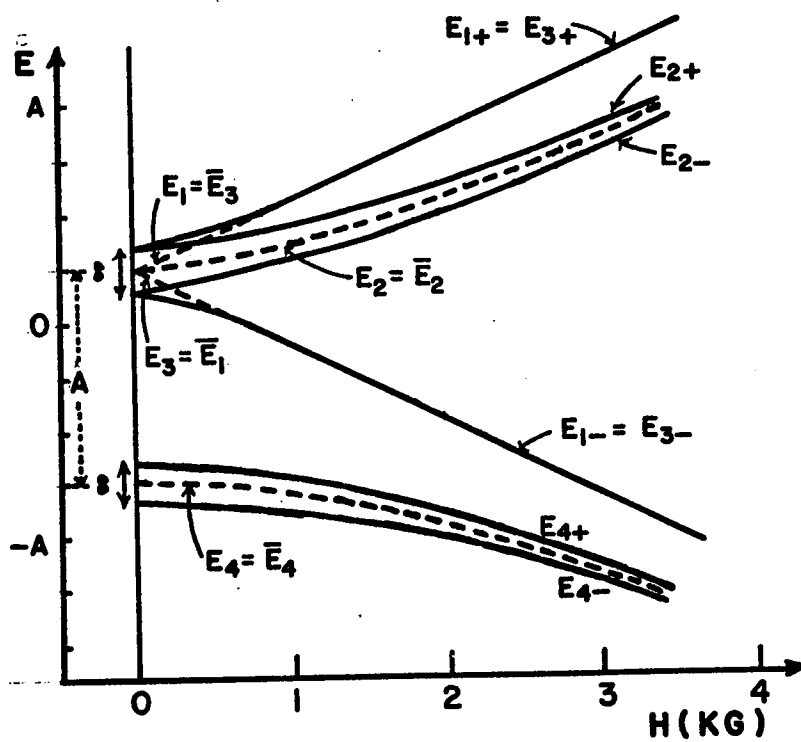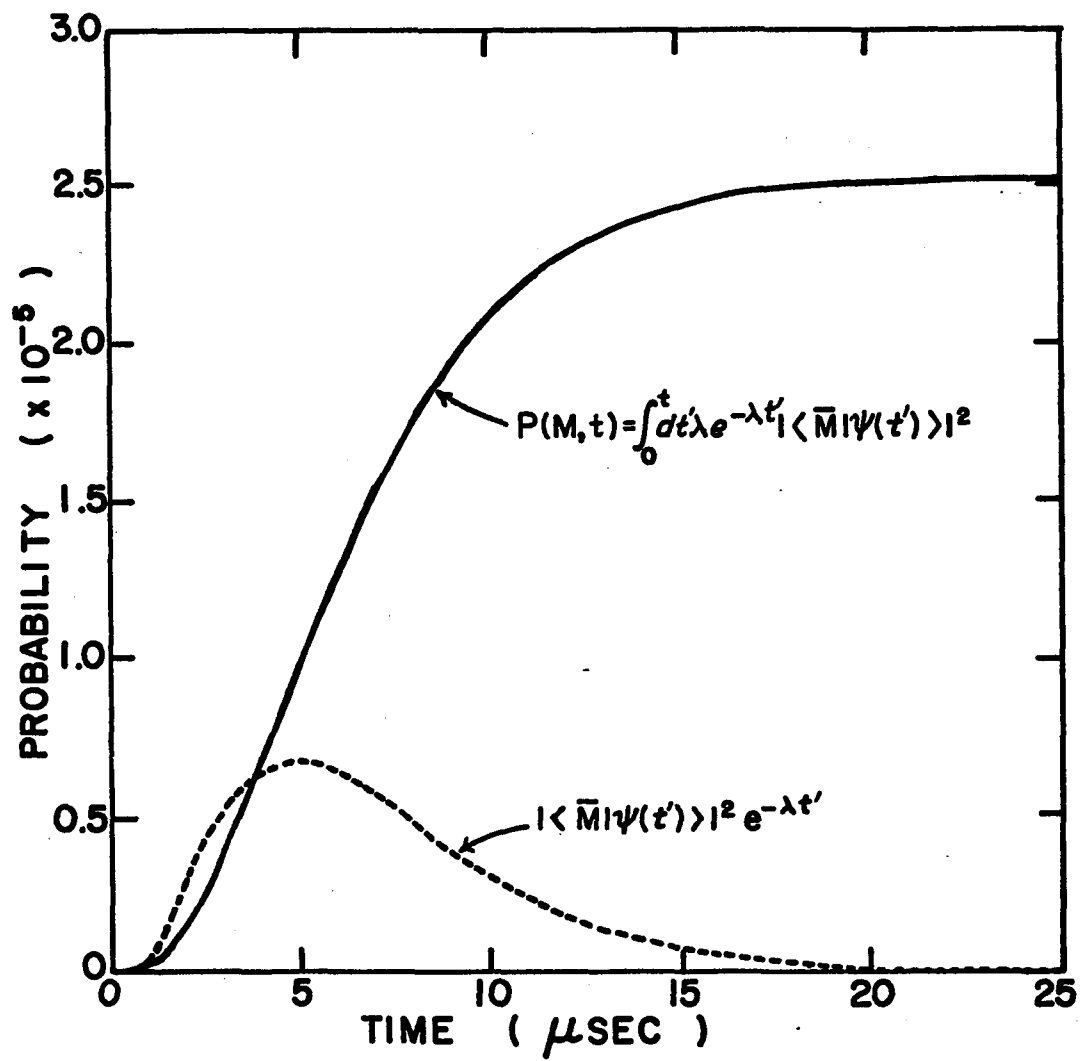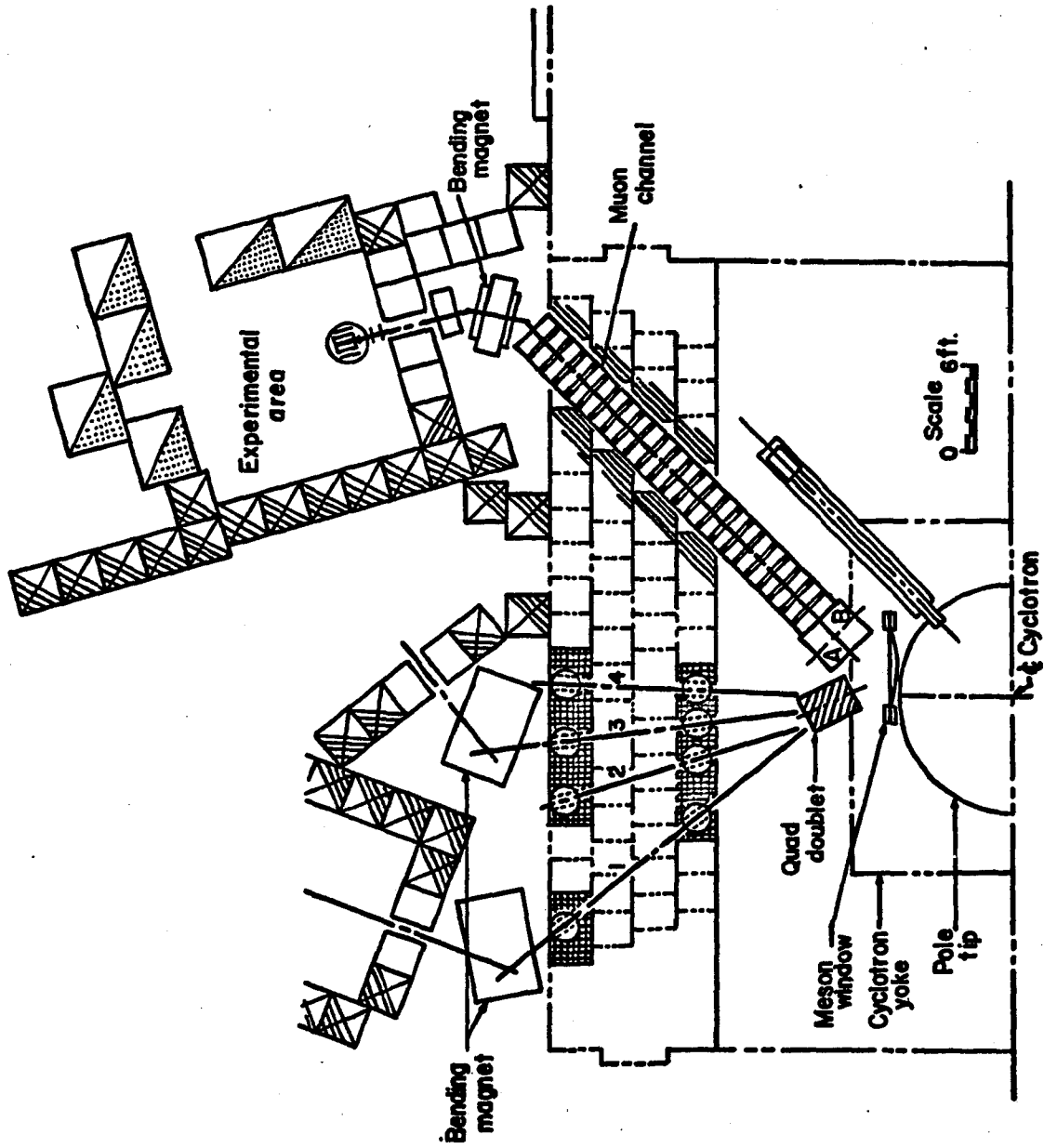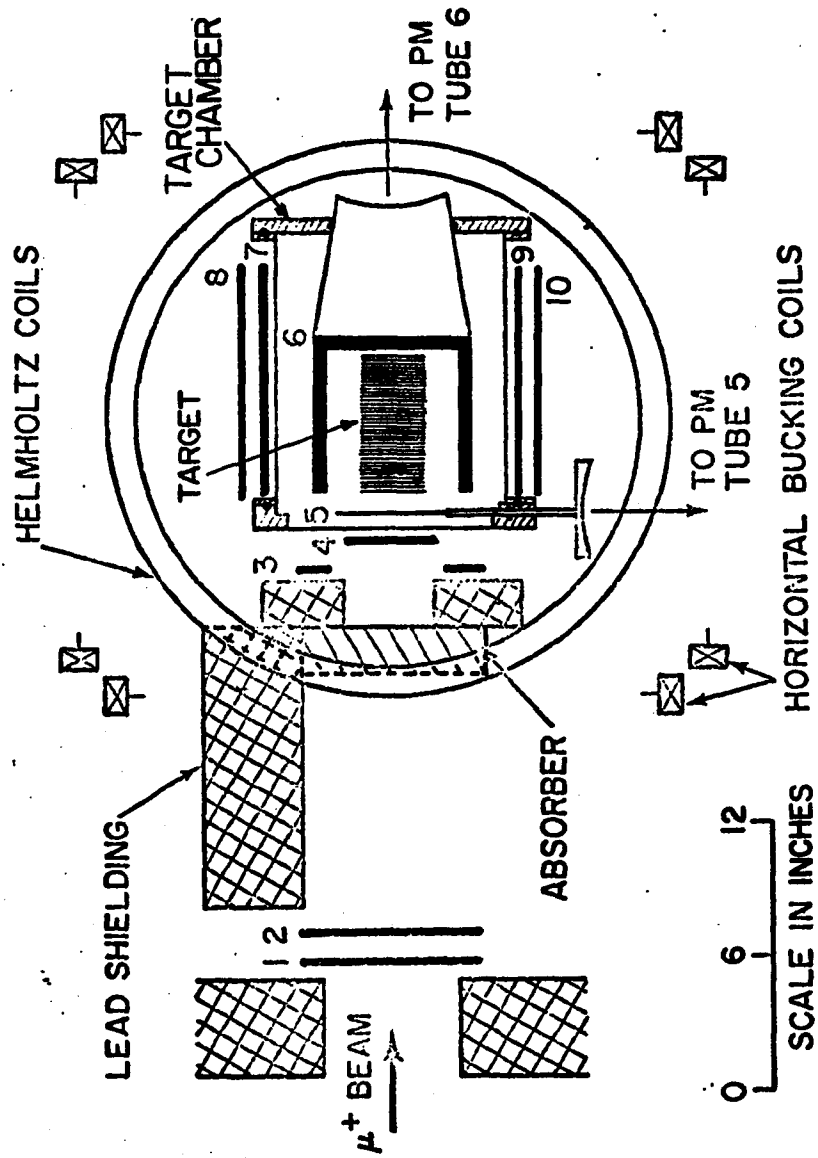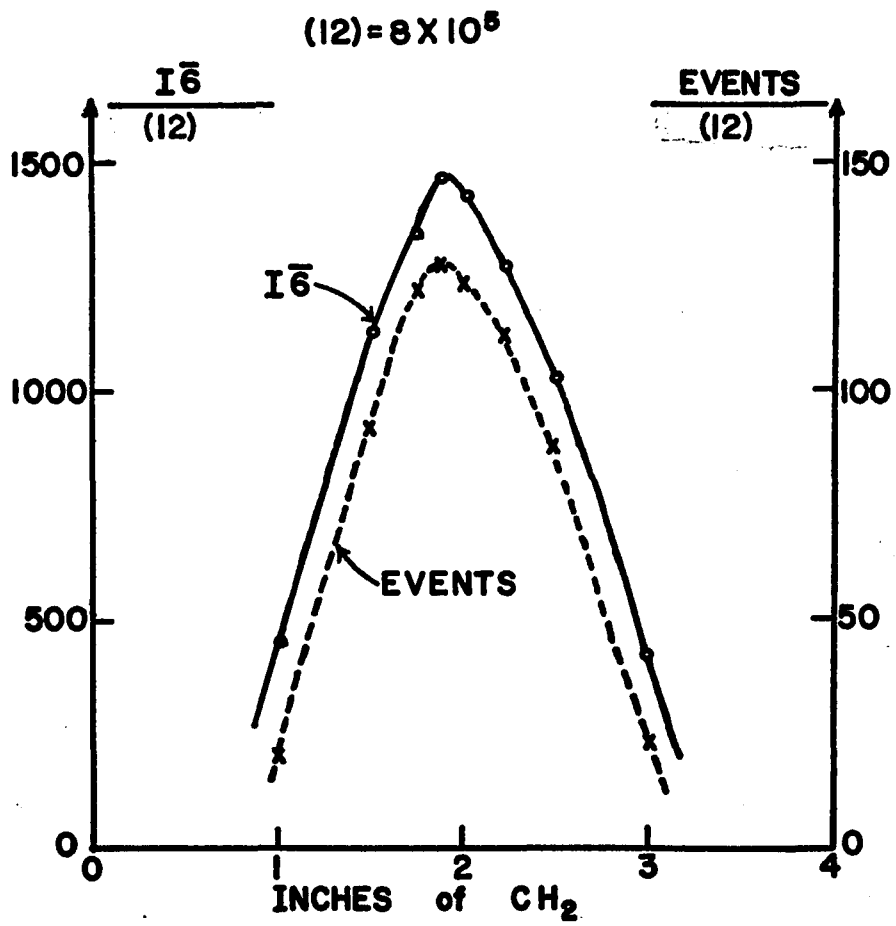
Figure 4

Figure 5

Figure 6
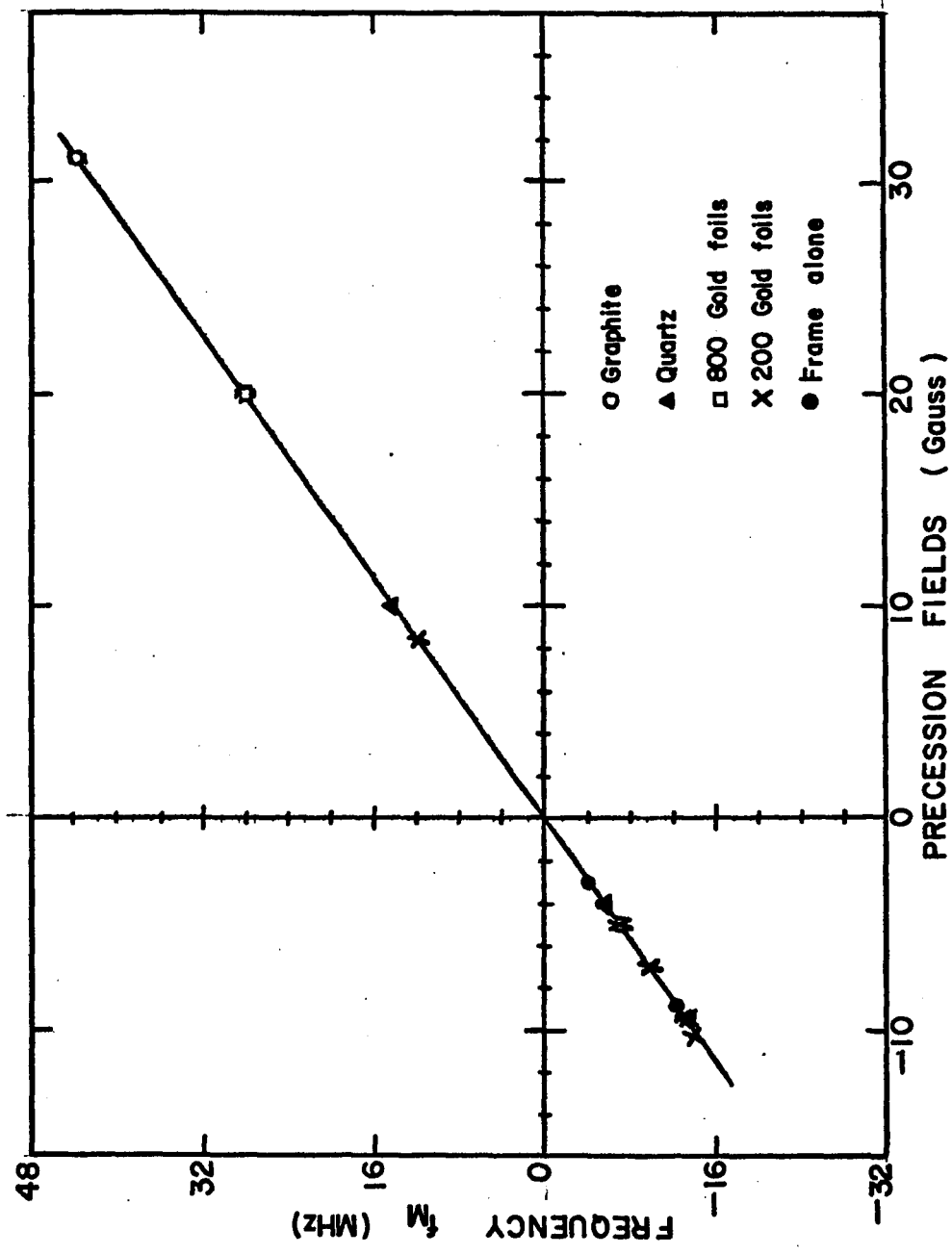
Figure 7
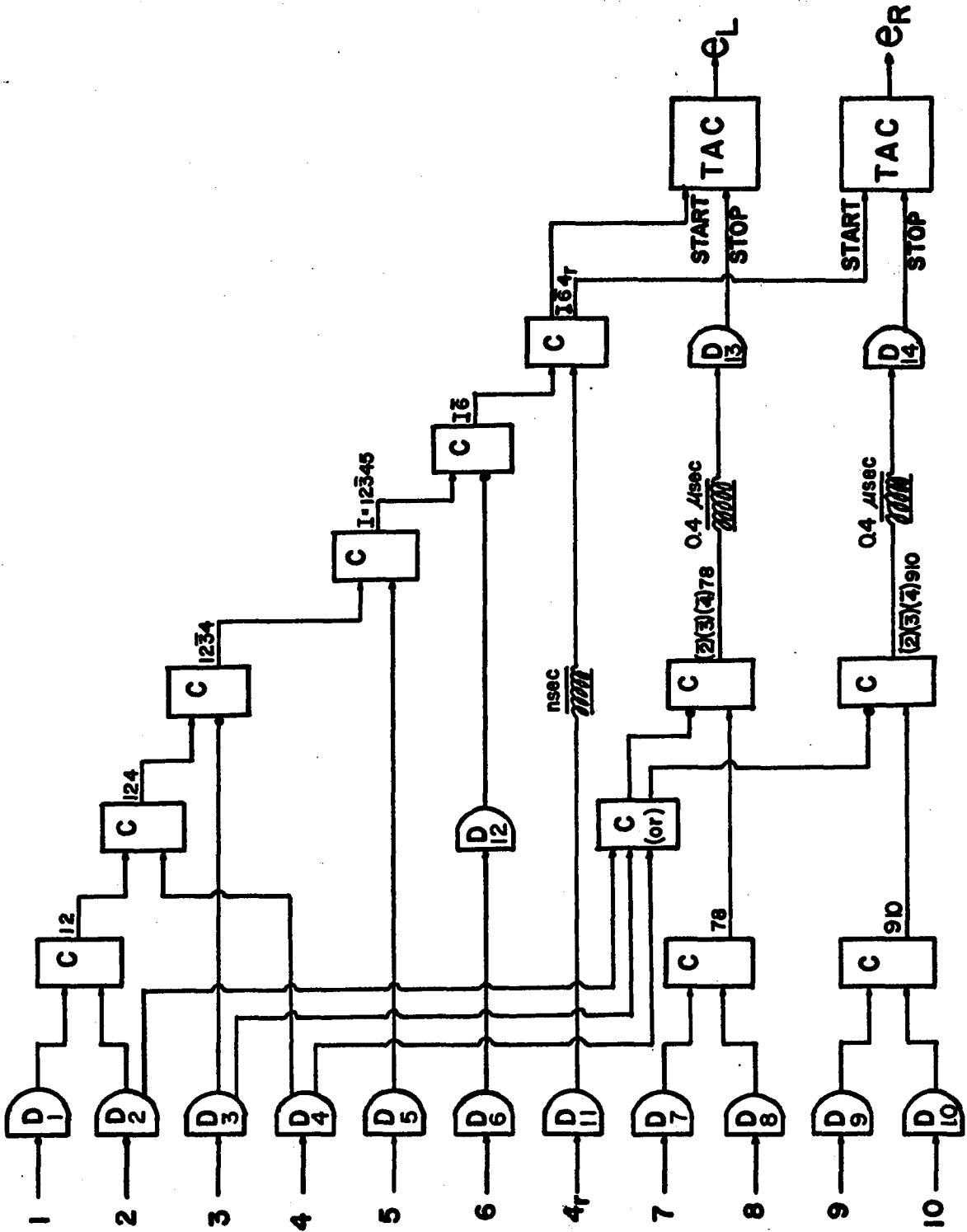
Figure 8

Figure 9

Figure 10

ARGON

CHANNEL NUMBER

AMPLITUDE
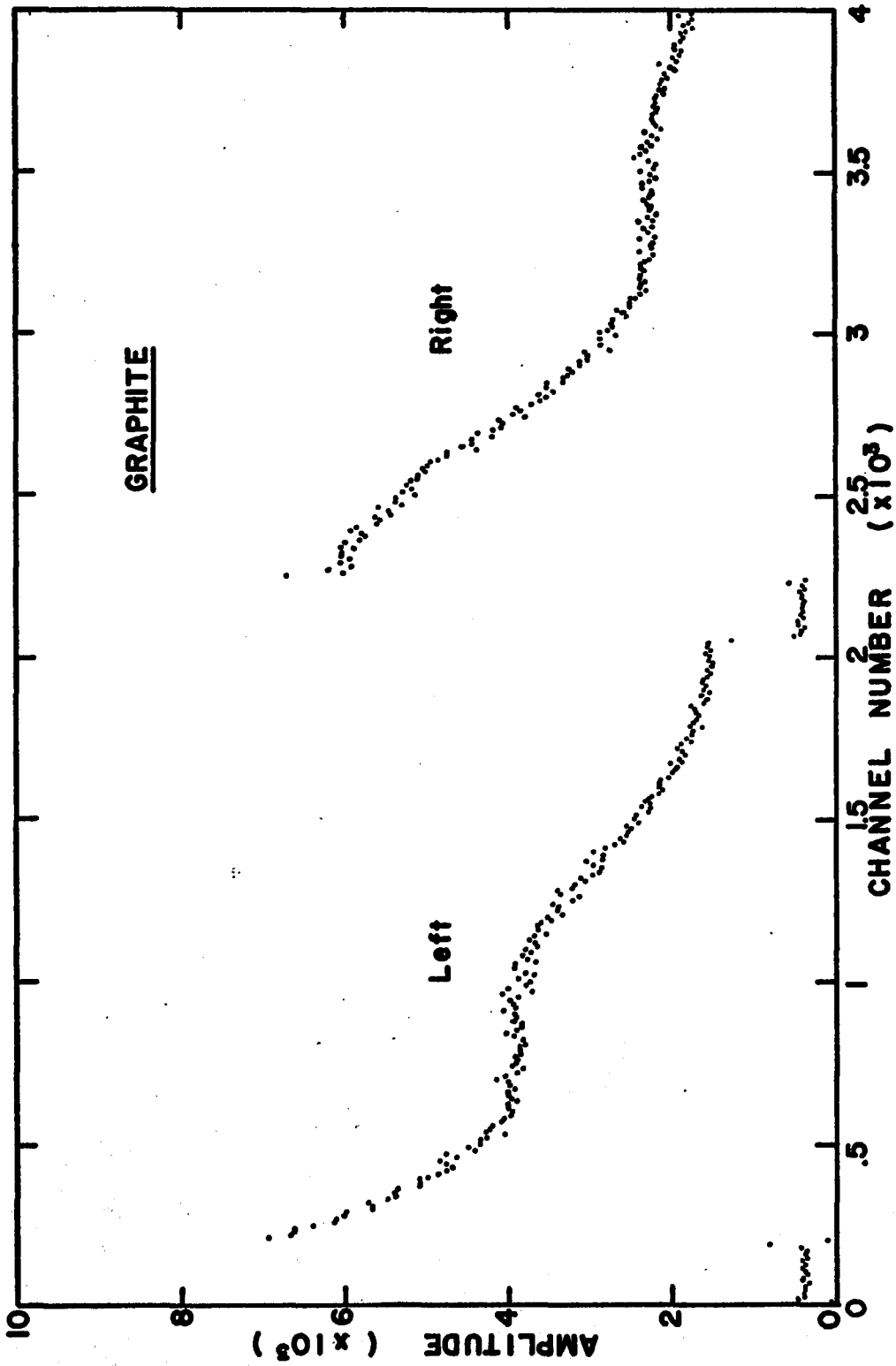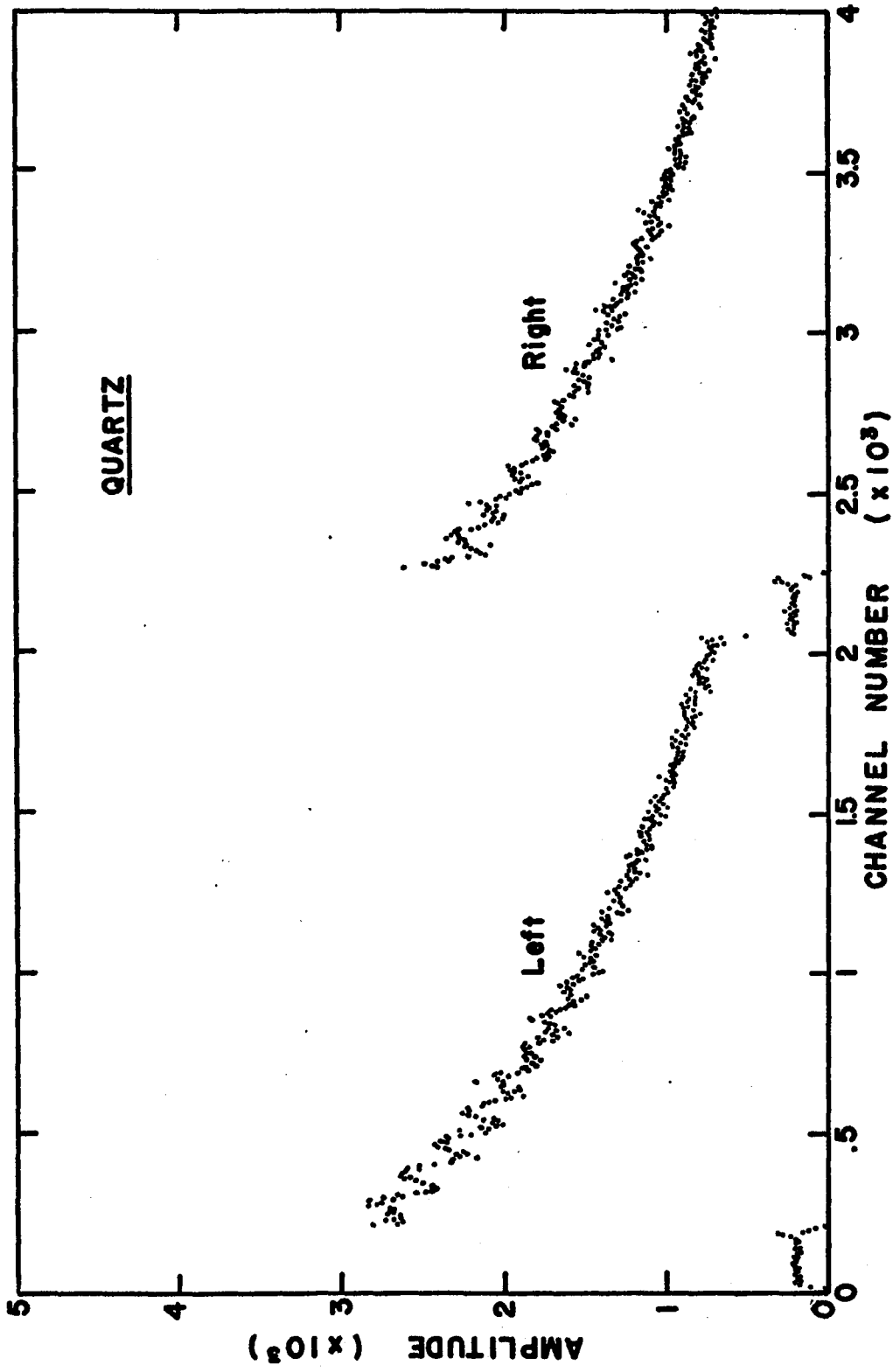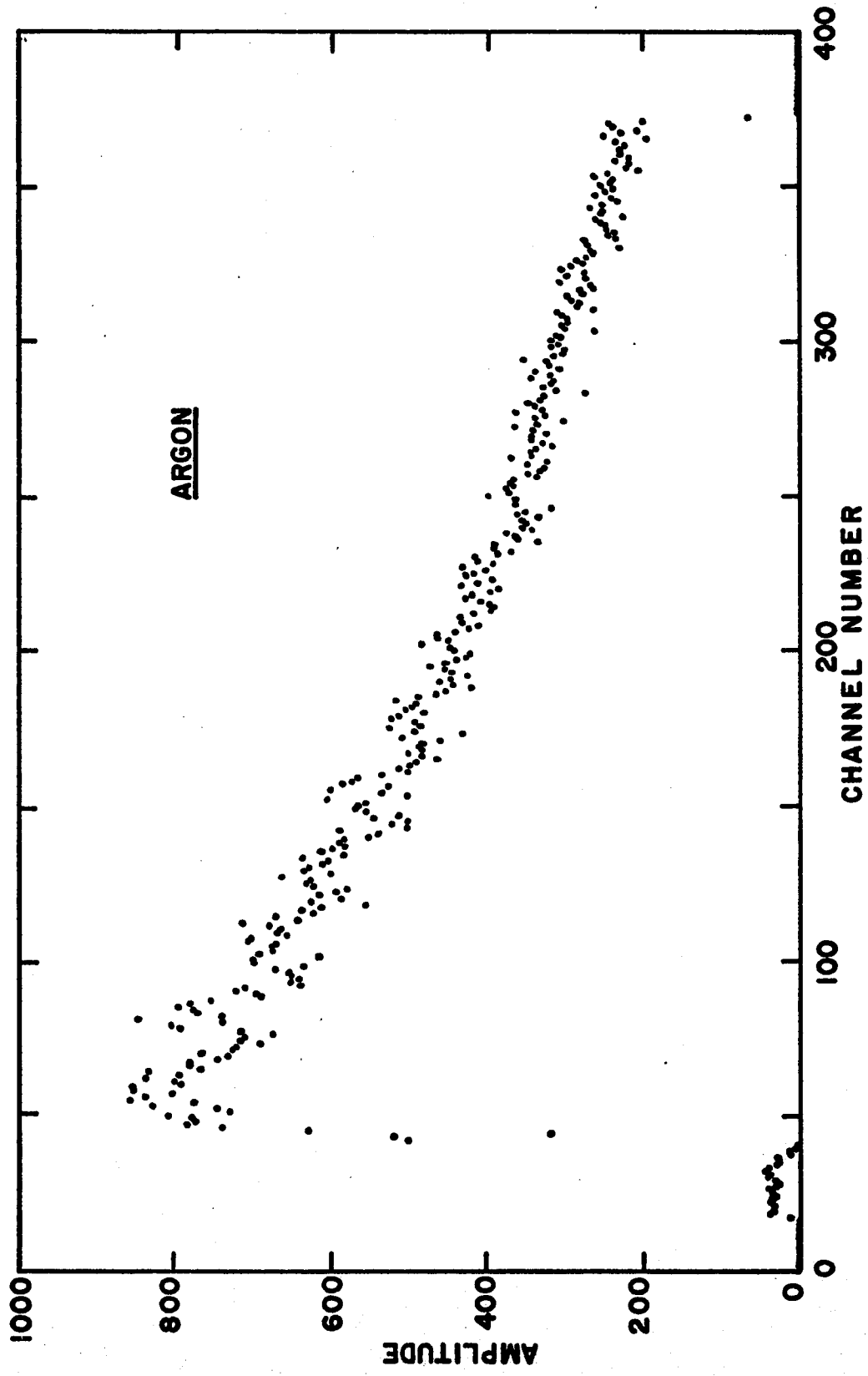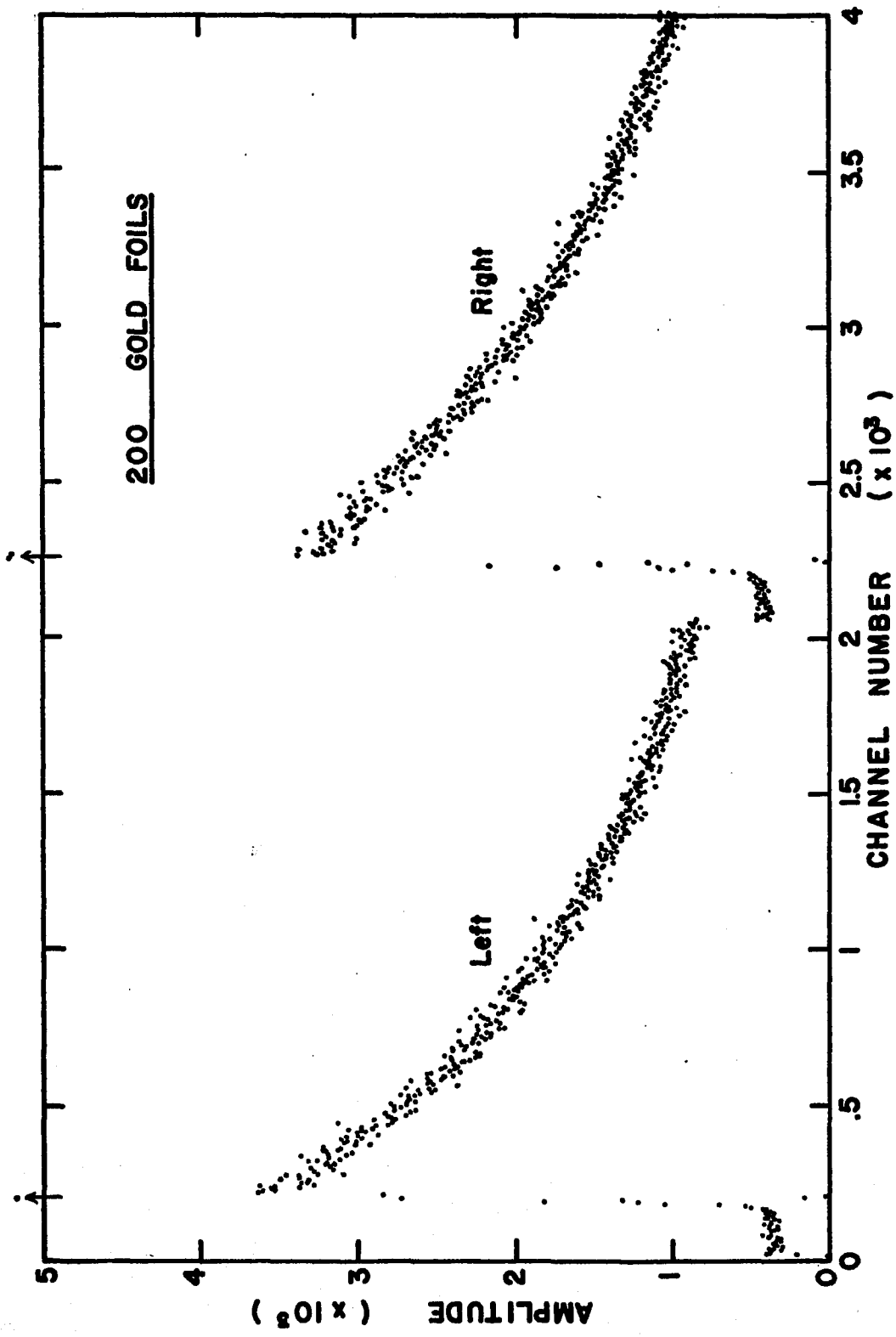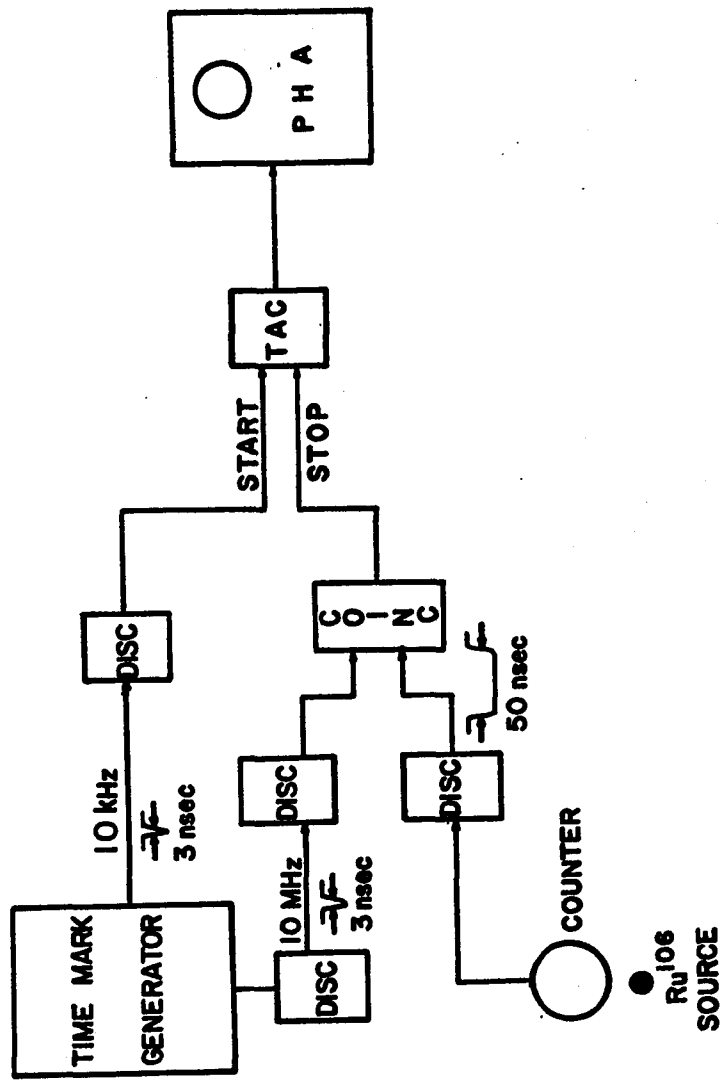
Figure 11

Figure 12

Figure 13
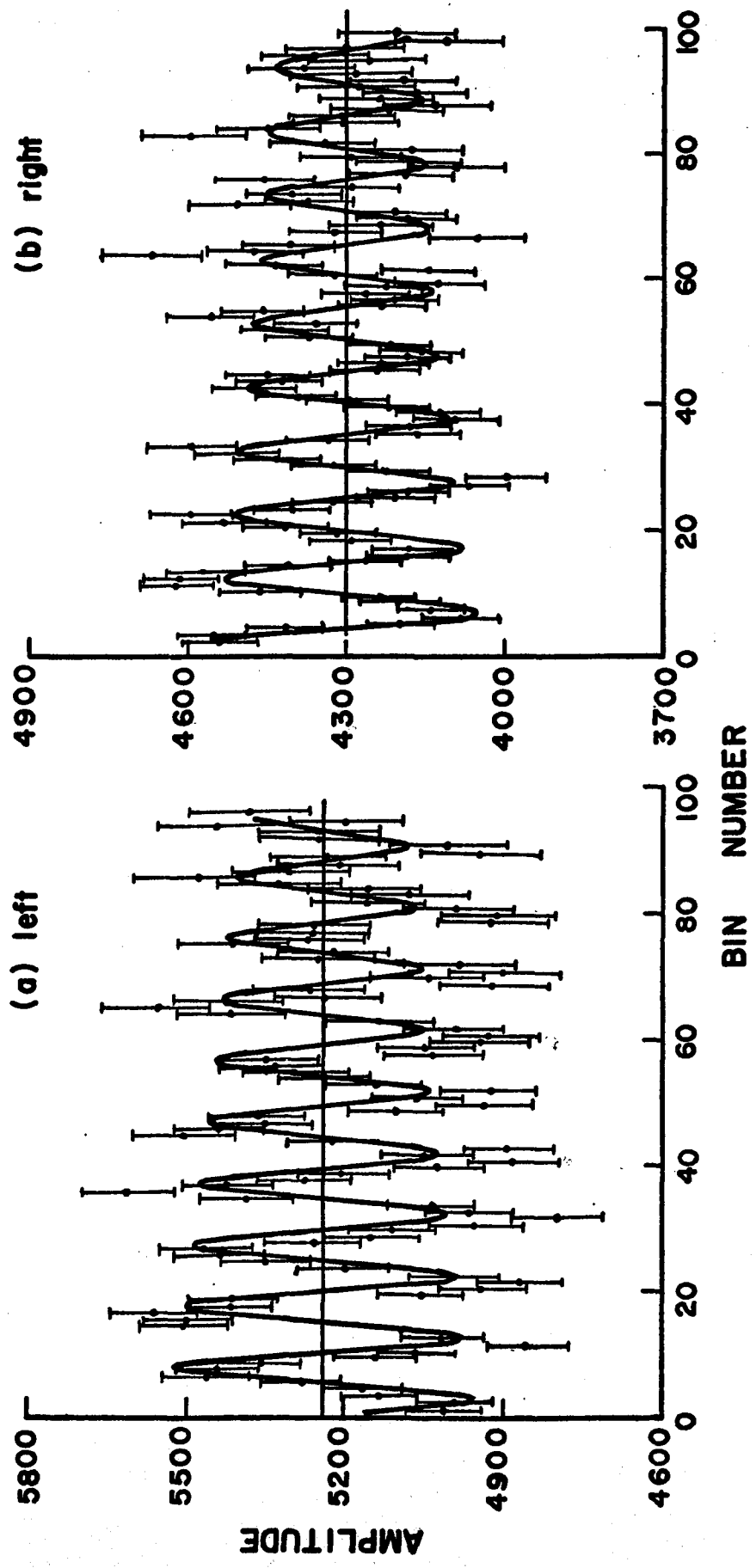
Figure 14
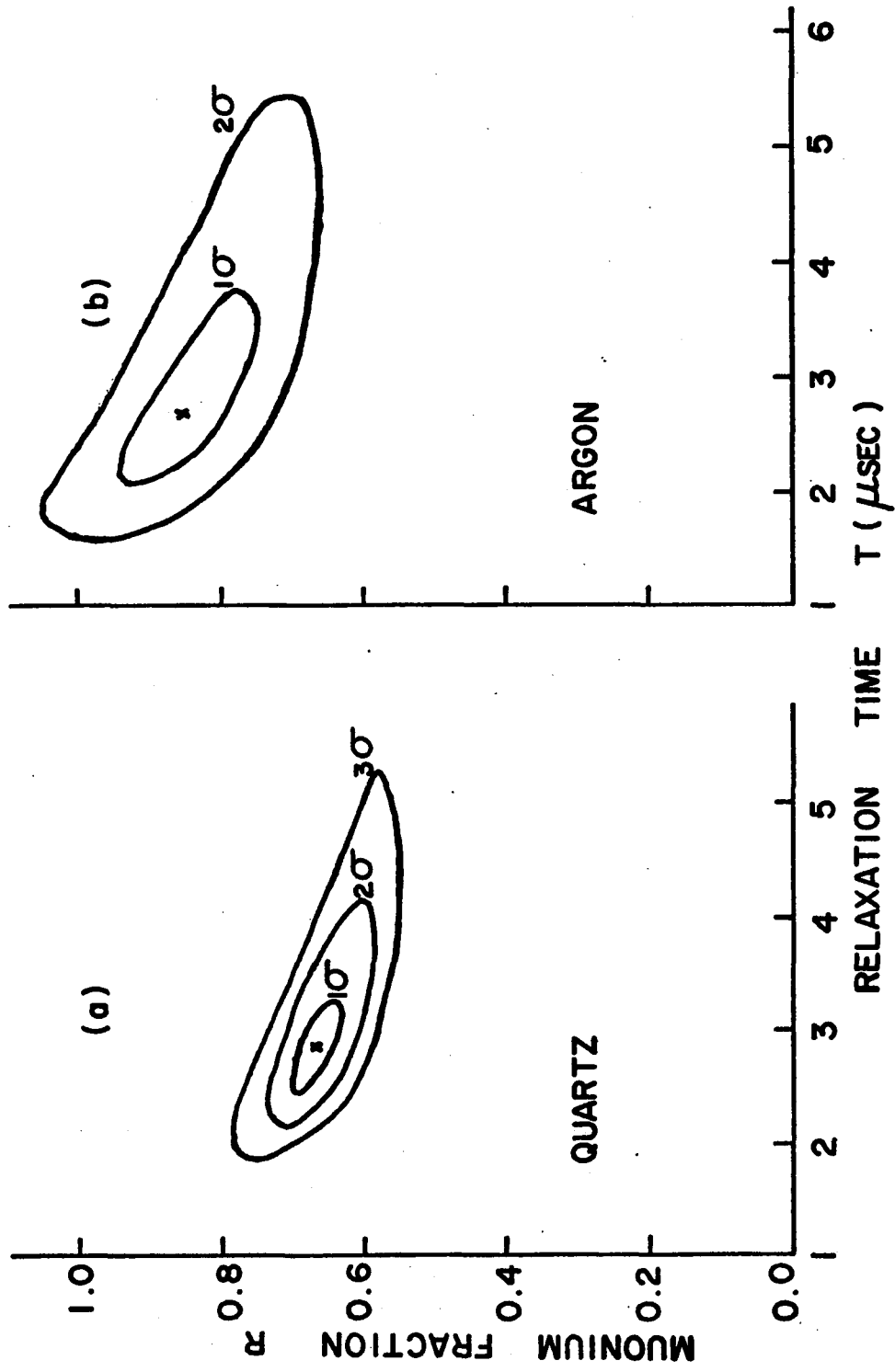
Figure 15
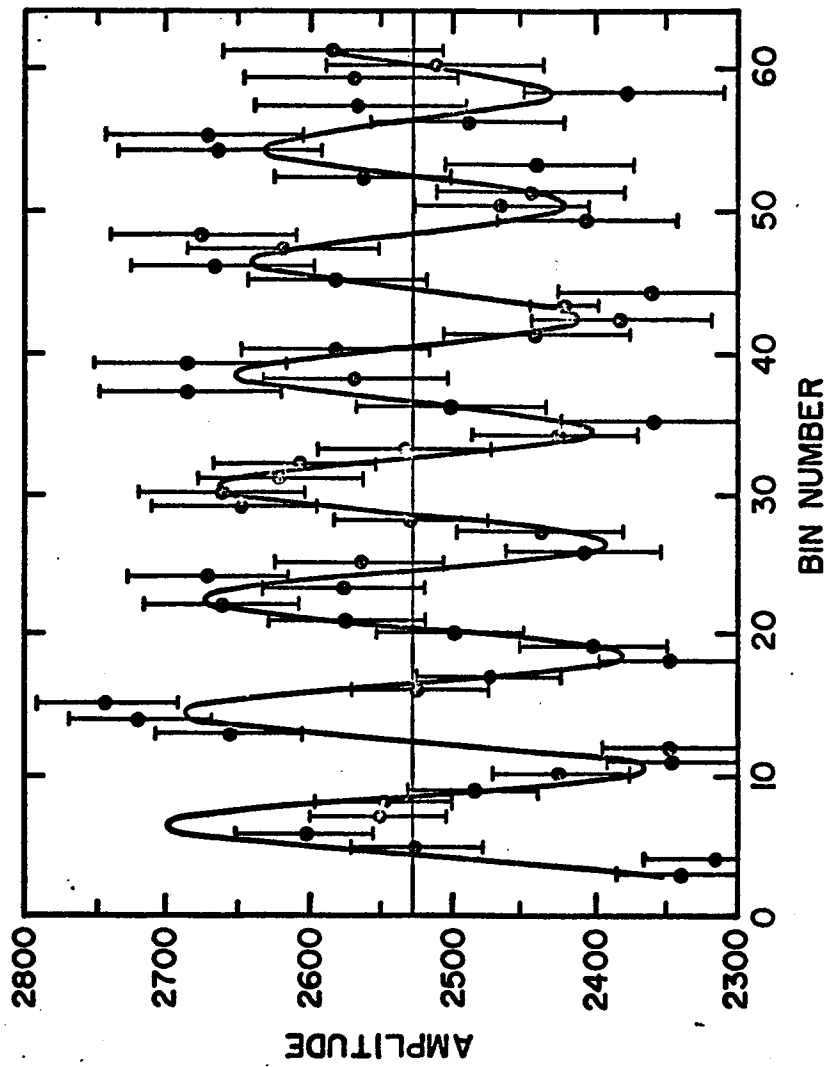
Figure 16
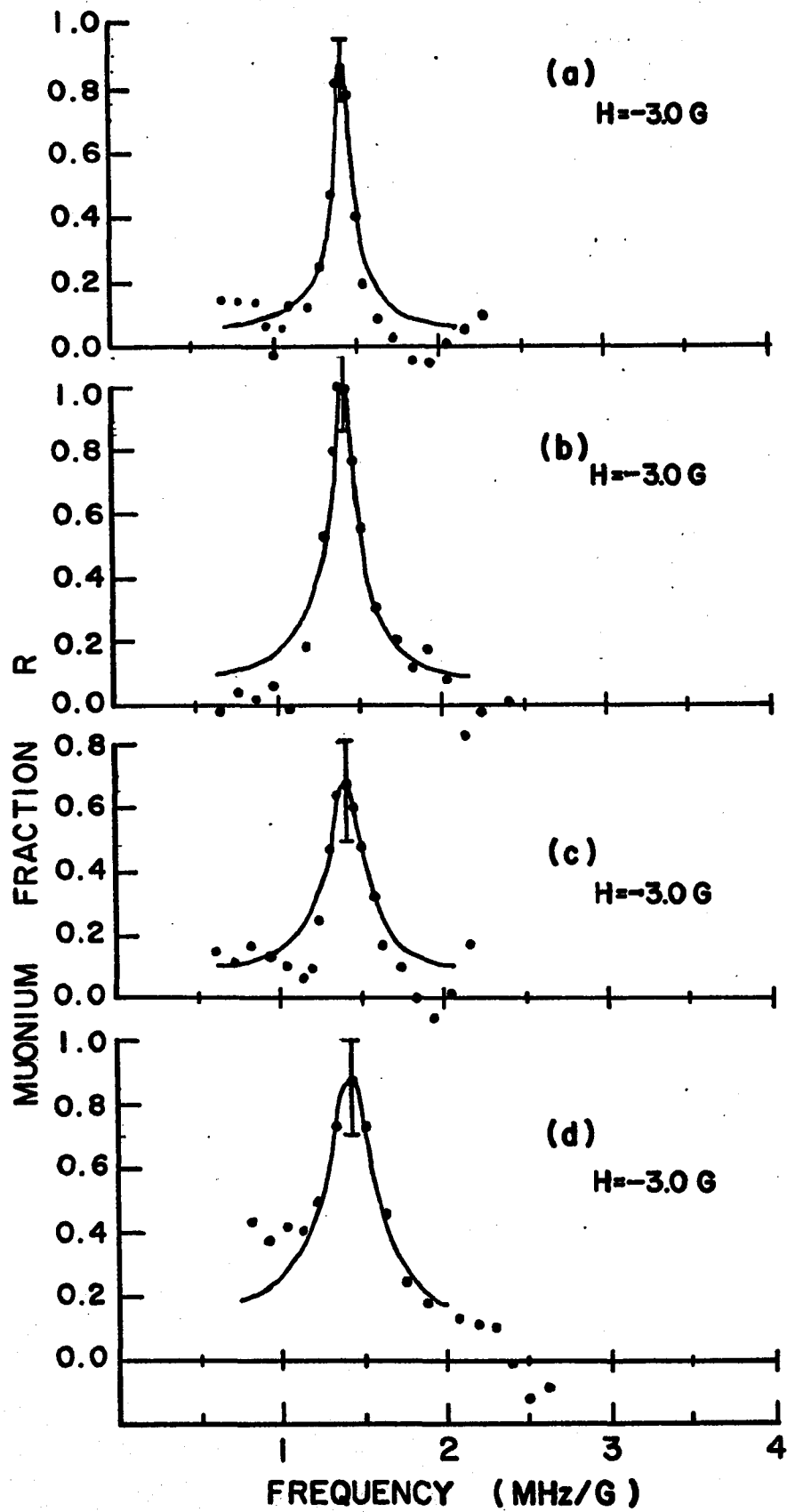
Figure 17
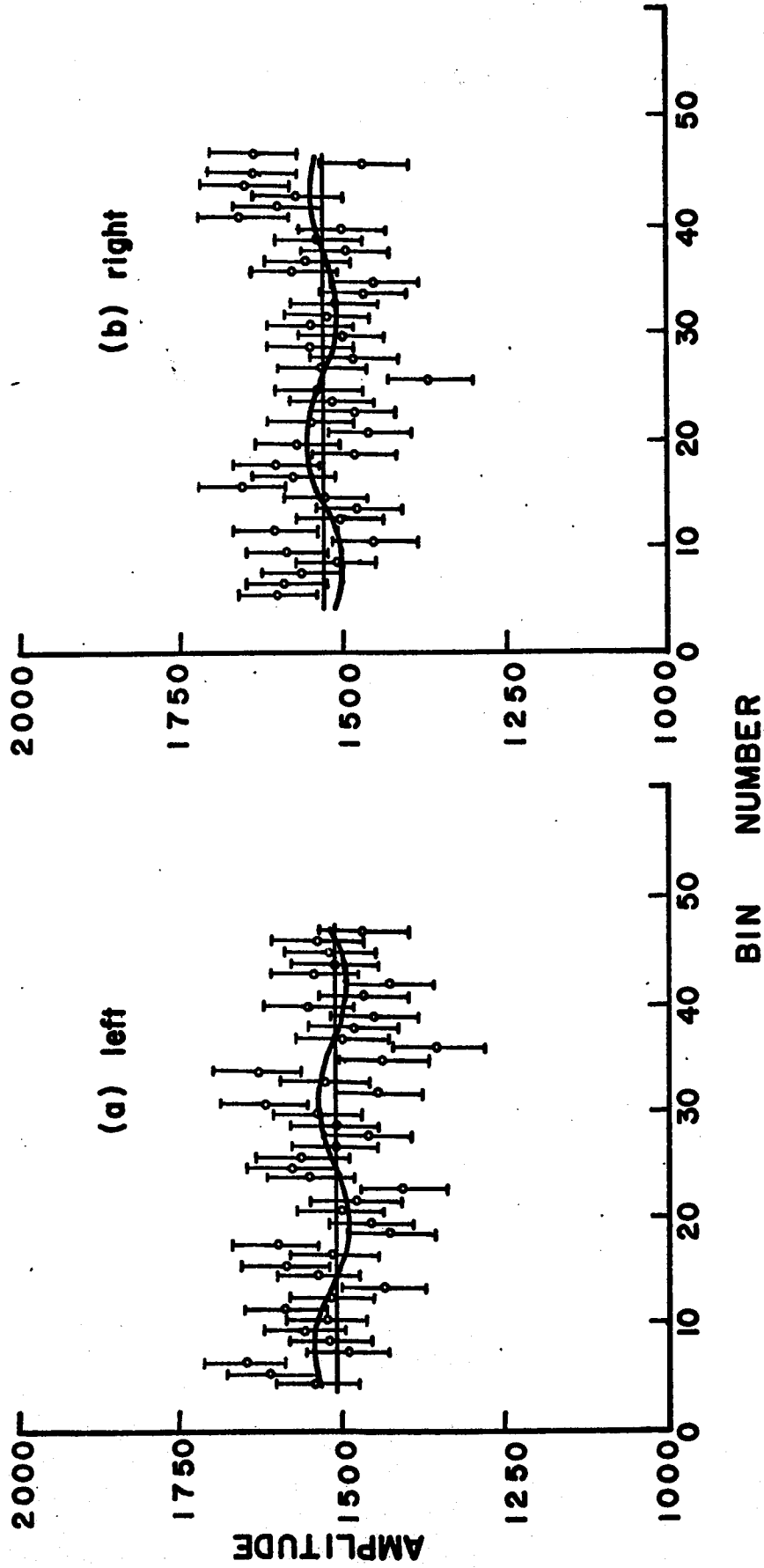
Figure 18
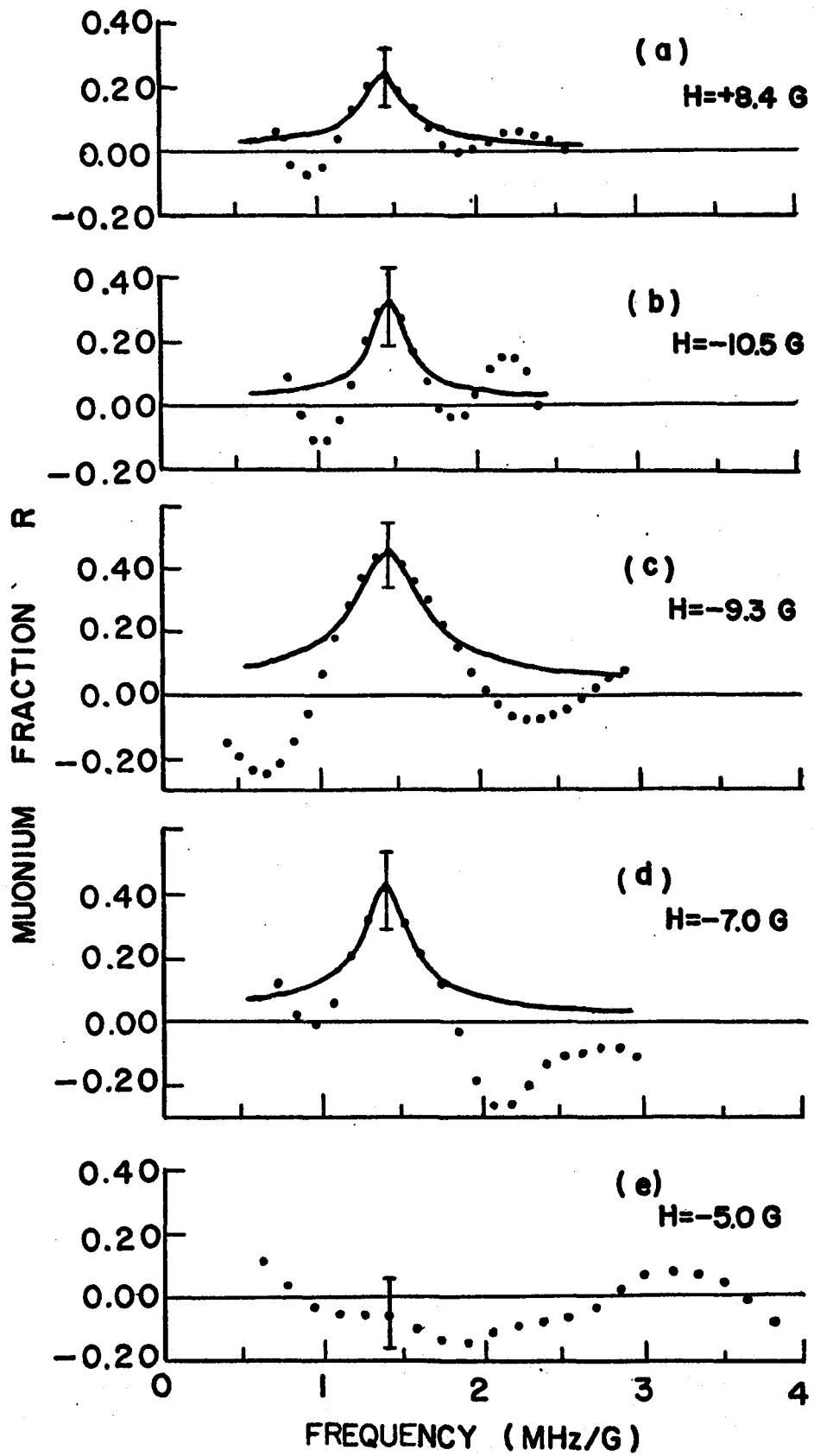
Figure 19
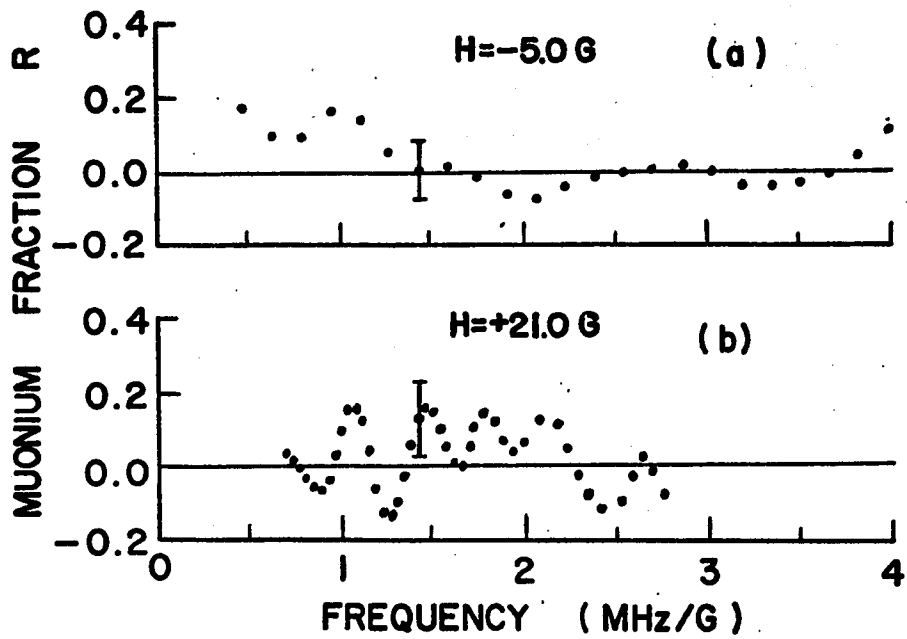
Figure 20
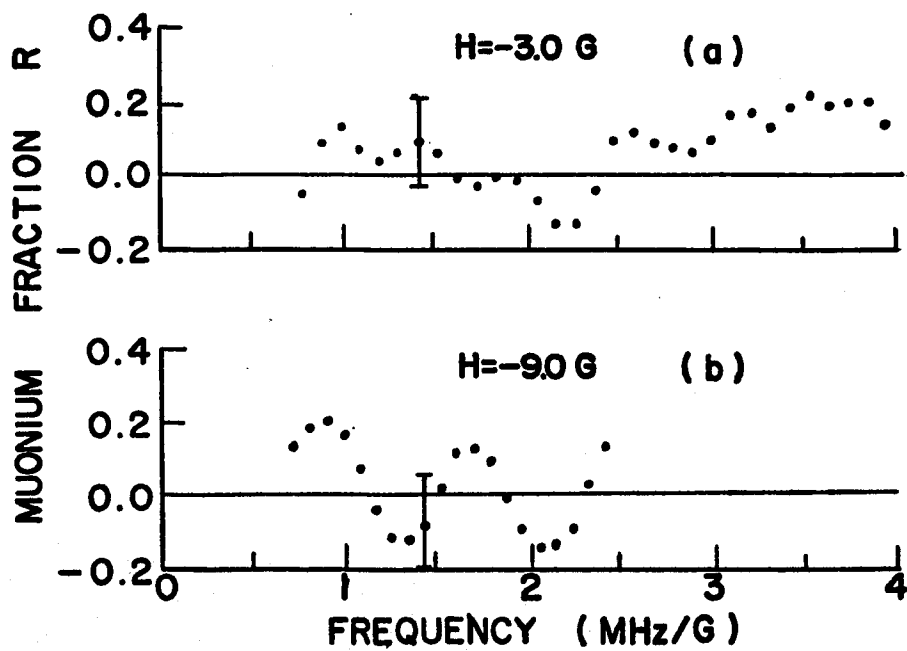
Figure 21
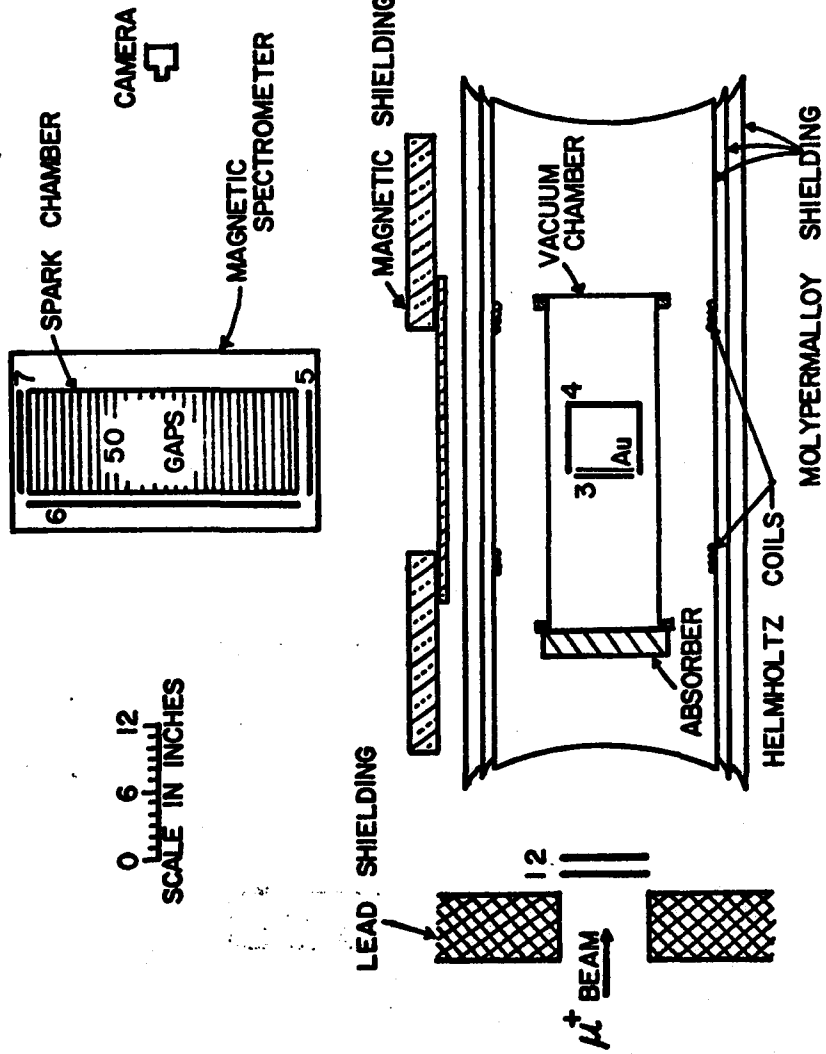
Figure 22

NOTE: A-A

ALTERNATE SHEETS
ARE ROTATED 180°
AROUND AXIS A-A
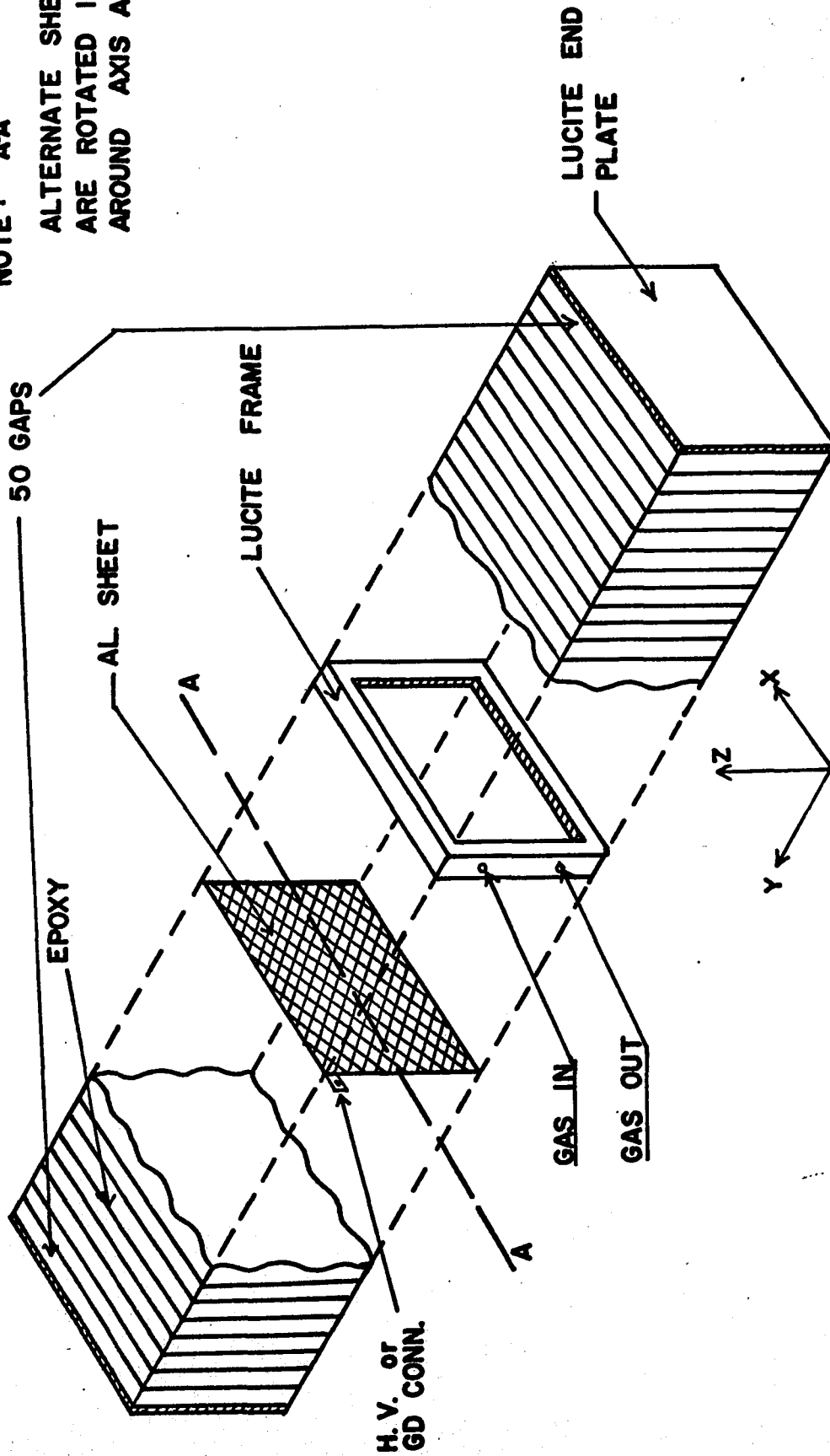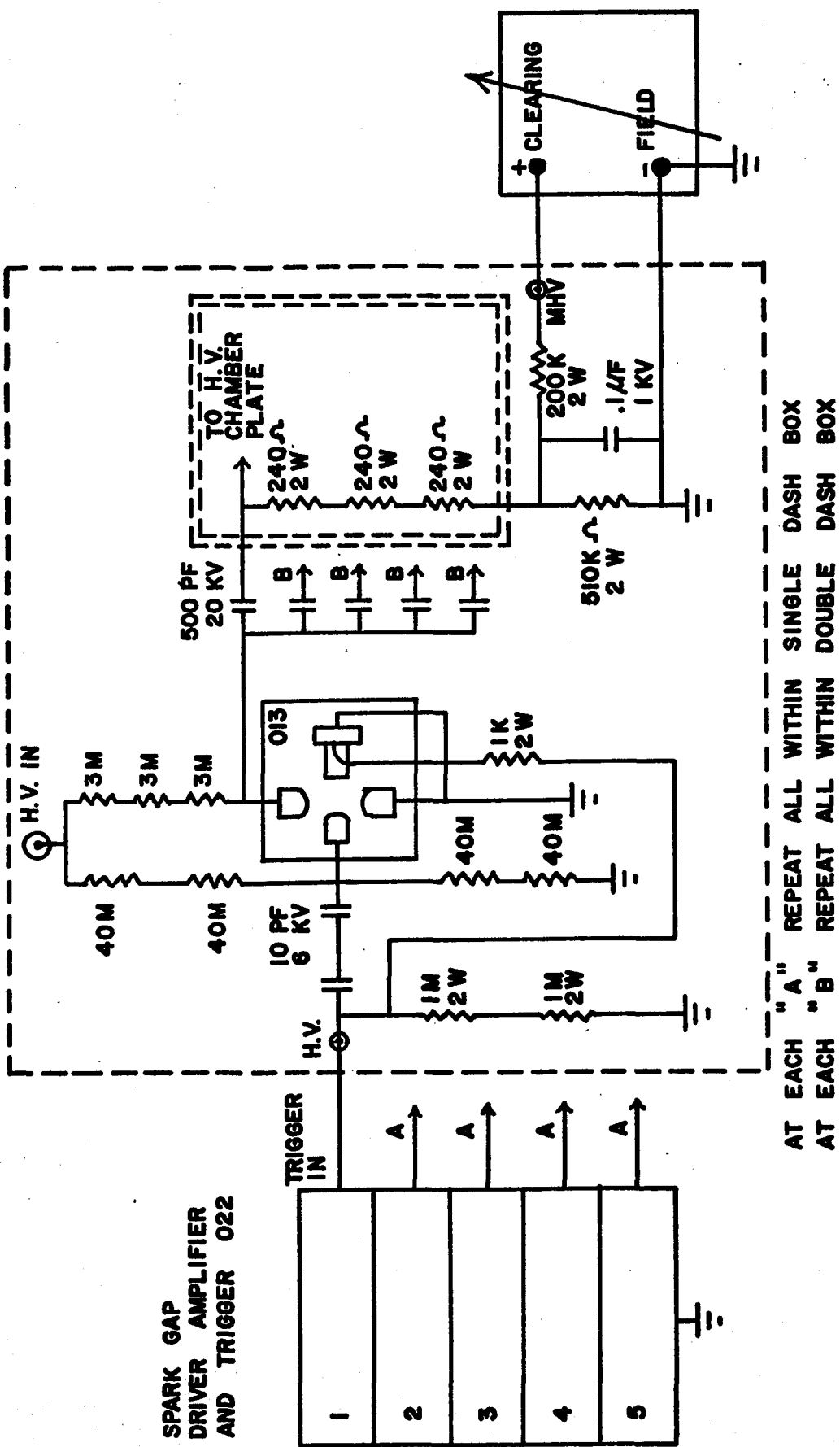
LUCITE END
PLATE

50 GAPS

LUCITE FRAME

AL SHEET

A

EPOXY

H.V. or
GD CONN.

GAS IN

GAS OUT

A

X

Z

Y

Figure 23

Figure 24

Figure 25

Figure 26

Figure 27

Figure 28